Neutron Scattering Studies of Modulated Magnetic Structures

Sørensen, Steen Aagaard

Publication date:
1999

Document Version
Publisher's PDF, also known as Version of record

Risø–R–1125(EN)

Neutron Scattering Studies of Modulated Magnetic Structures

Steen Aagaard Sørensen

Risø National Laboratory, Roskilde, Denmark
August 1999

Abstract This report describes investigations of the magnetic systems $DyFe_4Al_8$ and MnSi by neutron scattering and in the former case also by X-ray magnetic resonant scattering.
The report is divided into three parts: An introduction to the technique of neutron scattering with special emphasis on the relation between the scattering cross section and the correlations between the scattering entities of the sample. The theoretical framework of neutron scattering experiments using polarized beam technique is outlined. The second part describes neutron and X-ray scattering investigation of the magnetic structures of $DyFe_4Al_8$. The Fe sublattice of the compound orders at 180 K in a cycloidal structure in the basal plane of the *bct* crystal structure. At 25 K the ordering of the Dy sublattice shows up. By the element specific technique of X-ray resonant magnetic scattering, the basal plane cycloidal structure was also found for the Dy sublattice. The work also includes neutron scattering studies of $DyFe_4Al_8$ in magnetic fields up to 5 T applied along a $< 110 >$ direction. The modulated structure at the Dy sublattice is quenched by a field lower than 1 T, whereas modulation is present at the Fe sublattice even when the 5 T field is applied. In the third part of the report, results from three small angle neutron experiments on MnSi are presented. At ambient pressure, a MnSi is known to form a helical spin density wave at temperature below 29 K. The application of 4.5 kbar pressure intended as hydrostatic decreased the Néel temperature to 25 K and changed the orientation of the modulation vector. To understand this reorientation within the current theoretical framework, anisotropic deformation of the sample crystal must be present. The development of magnetic critical scattering with an isotropic distribution of intensity has been studied at a level of detail higher than that of work found in the literature. Finally the potential of a novel polarization device for small angle neutron scattering is demonstrated by measurements of the magnetic critical scattering from MnSi.

The present report is a revised version of the thesis, *"Neutron Scattering Studies of Modulated Magnetic Structures"* submitted August 1998 in partial fulfillment of the requirements for obtaining the Ph.D. degree in physics at the University of Copenhagen. Supervisors have been Bente Lebech, Risø National Laboratory, Allan R. Mackintosh, University of Copenhagen and Stig Steenstrup, University of Copenhagen. Involvements during the Ph.D.-work not reported in this thesis, has resulted in the following publications which are not regarded a part of the thesis:

- A. Pavese, M. Prencipe, M. Tribaudino and **S. Aa. Sørensen**, X-ray and Neutron Single Crystal Study of P4/n Vesuviate. Submitted to Canadian Mineralogist.
- A. Vigliante, M. J. Christensen, J. P. Hill, G. Helgesen, **S. Aa. Sørensen**, D. F. McMorrow, D. Gibbs, R. C. C. Ward and M. R. Wells, Interplay between structure and magnetism in Ho_xPr_{1-x} alloys. Phys. Rev. B. **57**, 5941.
- D. F. McMorrow, J-G. Lussier, B. Lebech, **S. Aa. Sørensen**, M. Christensen and O. Voigt, X-ray scattering study of the interplay between magnetism and structure in CeSb. J. Phys. Cond. Matt. Phys., **9**, 1133.
- S. Kawano, **S. Aa. Sørensen**, B. Lebech, and N. Achiwa, High pressure neutron diffraction studies of the magnetic structures of erbium. J. Magn. Magn. Mater., **140 - 144**, 763.
- K. Clausen, **S. Aa Sørensen**, K. A. McEwen, J. Jensen and A. R. Mackintosh, Crystal fields and conduction electrons in praseodymium. J. Magn. Magn. Mater., **140 - 144**, 735.

ISBN 87–550–2570–6
ISBN 87–550–2571–4 (Internet)
ISSN 0106–2840 Typeset by LaTeX

Grafisk Service · Risø · 1999

Contents

Part I
Introduction

Facilitated by the operation of research reactors, scattering of thermal neutrons has become an elegant and powerful probe of both static and dynamical properties of chemical and magnetic structure of solids. The power of the neutron relies on a number of fortunate intrinsic properties:

- Since the neutron is uncharged, it penetrates easily into a bulky sample.
- By means of the strong nuclear forces, the neutron interacts with the atomic nuclei of the sample.
- As the neutron possesses a magnetic moment, it interacts through magnetic dipole forces with the unpaired electrons of the sample.
- Due to the actual value of the neutron mass, neutrons with energies of the order of meV have de Broglie wavelengths of the order of Å. In a scattering experiment, the detectable momentum transfer is thus of the order of inverse atomic distance and at the same time, the detectable energy transfer is comparable to the characteristic energies of structural and magnetic excitations in solids.

The theoretical foundation of neutron scattering has been treated in great detail in several text books [47], [37]. The reader is referred to these texts and we shall only outline some principles of the derivation of fundamental results. In this introductory part, a number of corner stone results are stated and the focus has been put on a discussion of physical and experimental implications.

1 Scattering as a probe of correlations

In order to characterize a scattering process, the concepts of *scattering cross-sections* are introduced. As indicated in Fig. 1, we consider a scattering target being illuminated by a parallel beam of particles. By the *total scattering cross-section* of the target, we mean the total rate of scattering events divided by the incident flux:

$$\sigma = \frac{\text{Number of scattered particles}}{\text{Flux} \times \text{Time}} \tag{1}$$

It is clear from equation (1) that the dimension of σ is indeed area. To further characterize the angular dependence of the scattering process, the *differential scattering cross-section* is defined as the rate of particles scattered into the solid angle $d\Omega$ normalized with respect to incoming flux and $d\Omega$:

$$\frac{d\sigma}{d\Omega} = \frac{\text{Number of particles scattered into } d\Omega}{\text{Flux} \times \text{Time} \times d\Omega} \tag{2}$$

Finally, to account for the energy dependence of the scattering process, the *partial differential scattering cross-section* is defined as the differential scattering cross section with the restriction added that the energy transfer in the scattering process is in the interval dE around E and with the corresponding normalization with respect to dE:

$$\frac{d^2\sigma}{d\Omega dE} = \frac{\text{Number of particles scattered into } d\Omega \text{ with energy transfer within } dE \text{ around} E}{\text{Flux} \times \text{Time} \times d\Omega \times dE} \tag{3}$$

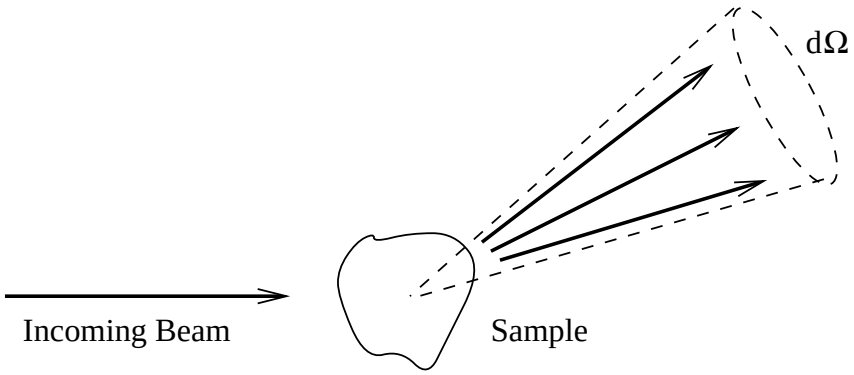

Figure 1. The geometry of a generic scattering experiment.

The three scattering cross-sections are related to each other through the integral relations:

$$\sigma = \int_{4\pi} \frac{d\sigma}{d\Omega} d\Omega = \int \int_{4\pi} \frac{d^2\sigma}{d\Omega dE} d\Omega dE \tag{4}$$

The theoretical treatment of the scattering of neutrons from an assembly of atomic nuclei is facilitated by either the Born approximation or by time dependent perturbation theory. In both cases, we must have a potential describing the interaction between the neutron and the nuclei. Since the linear extent of the atomic nucleus ($\approx 10^{-13}$ cm) is so much smaller than the (thermal) neutron de Broglie wavelength ($\approx 10^{-8}$ cm), one takes a delta function-like model potential known as the Fermi pseudo potential for the interaction between a neutron and a single nucleus. The potential contains a scaling parameter, b known as the *scattering length* of the nucleus in question. The scattering length of common isotopes have been experimentally determined and their values have been tabulated in various reference works [19]. From the simple model potential for each of the nuclei of the assembly, one forms the total scattering potential. Assuming no correlation between scattering length and position, the application of time dependent perturbation theory gives the following result for the partial differential scattering cross-section [47]:

$$\begin{aligned}
\frac{d^2\sigma}{d\Omega dE} &= \frac{\sigma_{coh}}{4\pi}\frac{k'}{k}\frac{1}{2\pi\hbar} \times \\
&\sum_{j,j'} \int_{-\infty}^{\infty} \left\langle \exp\{-\imath\vec{\kappa}\cdot\vec{R}_{j'}(0)\} \exp\{\imath\vec{\kappa}\cdot\vec{R}_j(t)\} \right\rangle \exp(-\imath\omega t) dt + \\
&\frac{\sigma_{incoh}}{4\pi}\frac{k'}{k}\frac{1}{2\pi\hbar} \times \\
&\sum_{j} \int_{-\infty}^{\infty} \left\langle \exp\{-\imath\vec{\kappa}\cdot\vec{R}_j(0)\} \exp\{\imath\vec{\kappa}\cdot\vec{R}_j(t)\} \right\rangle \exp(-\imath\omega t) dt
\end{aligned} \tag{5}$$

In the equation, k and k' denotes the wave numbers of the incoming and scattered neutron, respectively. $\vec{\kappa}$ is the scattering vector (the vector difference between the wave vectors of the incoming and the scattered neutron), $\vec{R}_j(t)$ is the position of the j'th nucleus at the time t. Further, $\hbar\omega$ is the energy transfered in the scattering process, $\sigma_{coh} = 4\pi(\overline{b})^2$ is proportional to the squared mean value of the scattering lengths and $\sigma_{incoh} = 4\pi\{\overline{b^2} - (\overline{b})^2\}$ is proportional to the variance of the nuclear scattering length. Finally, $<>$ denotes thermal averaging of matrix elements between initial and final states of neutron and scattering system. The

first term of (5) is known as the *coherent* part of the scattering cross-section. It is proportional to the square of the scattering lengths averaged over the nuclei of the sample and to the space-time Fourier transform of the thermal average of the so-called pair correlation function. It measures the degree of correlation between the position $\vec{R}_{j'}(0)$ of nucleus j' at one time (time zero) and the position $\vec{R}_j(t)$ of nucleus j at time t. The second term of (5) being proportional to the variance of the nuclear scattering lengths of the assembly is known as the *incoherent* scattering cross-section of the assembly. This term contains the space-time Fourier transform of the thermal average of the *auto correlation function*. This function measures the degree of correlation between the position of the *same* nucleus at different times. That is, the coherent part of the scattering cross-section holds information on both the collective structure and dynamics of the assembly and on the motion of the individual nuclei, whereas the incoherent part of the cross-section contains information on the individual motion only. By varying the momentum transfer $\hbar\vec{\kappa}$ and the energy transfer $\hbar\omega$ in a scattering experiment, we may probe the Fourier transformed) correlation functions at different points in the four-dimensional $(\vec{\kappa}, \omega)$-space. Throughout this work, we shall mainly consider the coherent part of the scattering focusing on the long-range ordered properties of samples. In other branches of neutron scattering research, the attention is devoted to the incoherent part of the scattering. This is the case when studying diffusive motion in solids and liquids. In the acquisition and analysis of scattering data, two key problems arise. Firstly, a real experimental device never samples the scattering cross-section in a single point in the $(\vec{\kappa}, \omega)$-space. Due to various instrumental imperfections (like finite collimations and imperfect crystals), we always observe the convolution of the cross-section and some instrumental response function, the *resolution function* centered in the nominal point $(\vec{\kappa}_0, \omega_0)$ defined by the setting of the instrument. It is important to understand that in any scattering experiment, there is a trade-off between resolution and intensity. Therefore, a very narrow instrumental resolution or a perfect instrument is rarely desirable. When planning an experiment, one should always determine the resolution needed to obtain the desired data and then chose instrument and configuration to match this need. When analyzing the data, it is standard procedure to account for the finite resolution by fitting the results to a combined sample-instrument model generated as a convolution of a pure sample cross-section and the instrumental resolution function. The other fundamental problem comes up when the "true" sample cross-section has been deconvoluted from the experimental data and we should interpret the various correlation functions in terms of the physical properties of the systems under investigation. In Fig.2, we show a few examples of corresponding structures and scattering patterns.

The equation (5) represents a fundamental and general expression for the scattering cross-section. It emphasizes the intimate relation between the scattering pattern and correlations between the atoms in the system under consideration. However, it is also useful to discuss simplified cross-sections valid under special conditions. The elastic scattering from a perfect crystal with no thermal motion of the atoms is an example of such special conditions. In this case, the position of any atom is expressed in terms of the Bravais lattice of the crystal structure. A plane wave incident on the crystal is scattered into a spherical wave by every single nucleus. The amplitude of each spherical wave is given by the respective scattering lengths and the resulting scattered wave is calculated by summing the spherical waves including the phase differences due to differences in the position of the

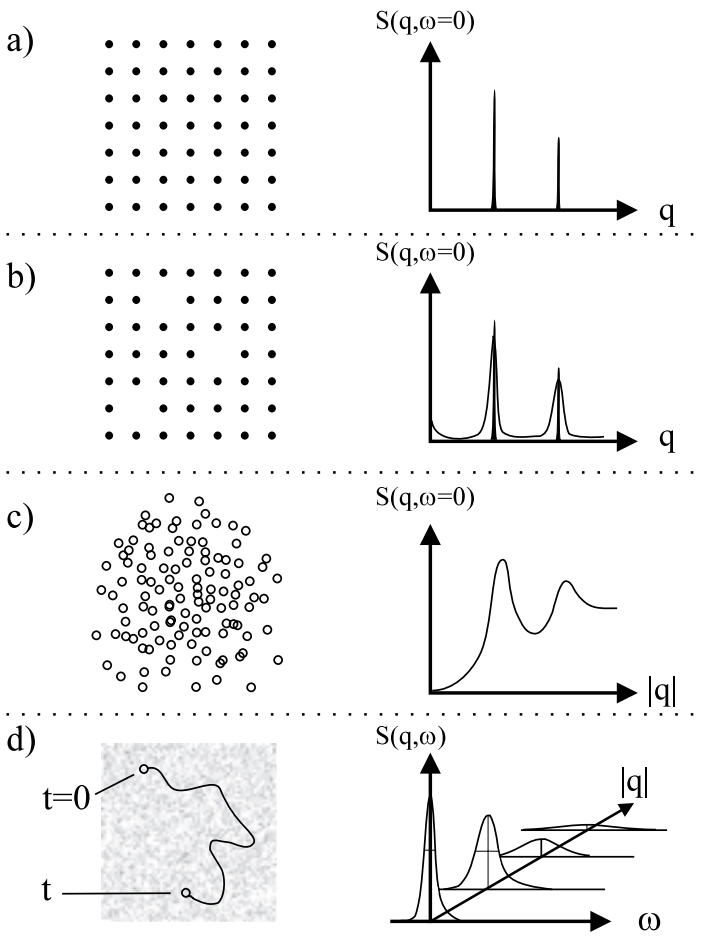

Figure 2. Some examples of real-space structures and corresponding scattering patterns. a) The elastic scattering from a perfectly periodic array of scatterers forms sharp peaks in the momentum transfer space. b) Imperfections in the perfectly ordered system cause the diffraction peaks to smear out. c) The scattering becomes more and more diffuse as the system disorders, d) The incoherent part of the scattering resulting from the second (auto correlation) term of equation (5) holds information about the diffusion of scatterers.

scattering nuclei. Straight forward geometrical considerations yield the result [43]:

$$\frac{d\sigma}{d\Omega}^{el} = \left| F(\vec{\kappa}) \sum_{\vec{R}} e^{\imath\vec{\kappa}\cdot\vec{R}} \right|^2 \tag{6}$$

with the sum including all Bravais lattices points $\vec{R}$. The *structure factor* $F(\vec{\kappa})$ is defined as the sum of scattering length times phase factor within the crystal unit cell:

$$F(\vec{\kappa}) = \sum_j b_j e^{\imath\vec{\kappa}\cdot\vec{d}_j} \tag{7}$$

where $\vec{d}_j$ and b_j denotes position and scattering length of the j'th atom within the unit cell. For an infinite (or macroscopic) number of atomic scatterers in the perfect crystal, the sum (6) cancels for all scattering vectors $\vec{\kappa}$ except those belonging

to the reciprocal lattice of the crystal. The intensity of each of these reflections is governed by the structure factor.

To briefly compare the X-ray charge scattering and the neutron nuclear scattering, we note that typical nuclear scattering lengths are of the order 10^{-12} cm resulting in scattering cross-sections of the order 10^{-24} cm^2. For X-rays, the high energy scattering length is given by Zr_0 with Z being the atomic number (the number of electrons) and $r_0 = 2.8 \times 10^{-13}$ cm. Hence, the order of magnitude of the neutron and the X-ray scattering lengths are comparable. Note however, that whereas the X-ray scattering length varies linearly with the number of electrons, the nuclear neutron scattering length varies among the isotopes in an apparently non-systematic way. Although the nuclear neutron and X-ray charge scattering lengths are of comparable magnitude, the intensity at available neutron sources is many orders of magnitudes lower than the intensity of even small laboratory X-ray sources. The neutron flux at the sample position of the TAS1 instrument at Risø National Laboratory is 8.7×10^6 n/s/cm^2 at 14 meV incident energy measured with approximately 1 degree beam divergence and an energy bandwidth of about 5%. Fluxes approximately 10 times higher are available under similar conditions at leading high flux reactors. Compare this to the brilliance of the order 10^{10} photons/s/cm^2/mrad^2 in 0.1% bandwidth from a rotating anode laboratory X-ray source. Brilliances more than 10 orders of magnitude higher than this are available at third generation synchrotron radiation sources. Thus, neutron scattering is a highly intensity limited technique and the correct choice of instrumentation and configuration is often crucial. As a final point in the comparison of the X-ray and neutron scattering techniques, we turn to absorption. In table 1, the $1/e$-penetration lengths are quoted for the two cases of Be and Ho with 25 meV neutrons and 1.54 Å X-rays (Cu K-α).

Radiation	Be	Ho
Neutrons @ 25meV (1.8Å)	2×10^{3} cm	6×10^{-1} cm
X-rays @ 1.54 Å (8.0 keV)	4×10^{-1} cm	9×10^{-4} cm

Table 1. Some typical $1/e$-absorption lengths for neutrons and X-rays. The figures are based on table 6, [1] p. 72.

2 The magnetic scattering length

The neutron scattering caused by the magnetic dipole coupling between the neutron magnetic moment and unpaired electrons in the sample is included in the formalism demonstrated above by the introduction of a magnetic scattering length. It takes the form of a scalar product between the normalized neutron spin operator $\vec{\sigma}$[1] and a quantity $\vec{b}_m$ known as the *magnetic scattering length vector*. It is derived directly from the magnetic dipole interaction potential, and has the vector character to account for the anisotropy of the magnetic dipole coupling. The magnetic scattering amplitude depends on the mutual orientation of the neutron and sample magnetic moments and the momentum transfer of the scattering event. As demonstrated in [3], the application of fundamental electrodynamics and the

[1]The components of the spin vector operator $\vec{\sigma}$ are the Pauli matrices σ_x, σ_y and σ_z.

Born approximation yields the result:

$$\vec{b}_m = \frac{\gamma e^2}{2m_e c_0^2} f(\vec{\kappa}) \frac{|\vec{\mu}|}{\mu_B} (\hat{\mu} - \hat{\kappa}(\hat{\kappa} \cdot \hat{\mu})) \tag{8}$$

In this expression, $\gamma = 1.91$ denotes the neutron gyromagnetic ratio, $\vec{\mu}$ is the atomic magnetic moment and $\hbar\vec{\kappa}$ is the momentum transfer. The hat symbol indicates unit vectors ($\hat{\kappa} = \vec{\kappa}/|\vec{\kappa}|$; $\hat{\mu} = \vec{\mu}/|\vec{\mu}|$). The function $f(\vec{\kappa})$ known as the *magnetic form factor* accounts for the effect of the electronic wave functions having linear extensions comparable to the neutron de Broglie wavelength. The concept of a form factor is familiar from the electronic charge scattering of X-rays. In analogy to the X-ray case, the magnetic form factor represents the Fourier transform of the density of magnetic moment in the target atom. The remaining symbols in equation (8) follow standard notation. Instead of quoting the derivation of (8) from [3], we shall give some physical reasoning for the components of the relation. We have already explained the meaning of the form factor, $f(\vec{\kappa})$. The term $|\vec{\mu}|/\mu_B$ simply gives the size of the sample magnetic moment in units of Bohr magnetons. In the same way, γ gives the neutron magnetic moment in units of nuclear magnetons. Thus, the scattering length quite reasonably depends on the product of the two interacting magnetic moments. We recognize the remaining physical constants, $e^2/m_e c_0^2$ as the classical electron radius, r_0. Since the nature of the interaction responsible for the scattering is electromagnetic, it is not surprising that r_0 turns up as the characteristic scale of the scattering length. Finally, the geometric term $(\hat{\mu} - \hat{\kappa}(\hat{\kappa} \cdot \hat{\mu}))$ implies that only the component of the sample magnetic moment perpendicular to the momentum transfer, $\hbar\vec{\kappa}$ may contribute to the scattering length. In scattering experiments using unpolarized incoming neutrons, the effect of this geometrical factor is the only source of information to the orientation of the sample magnetic moments. To illustrate the application of the magnetic scattering length vector, we consider the simple antiferromagnetic crystal depicted in Fig 3. The crystal is mono-atomic cubic with the atomic spins along the c-axis. Within planes perpendicular to this direction, the spins are parallel and these planes are antiferromagnetically coupled. Hence, we may write the magnetic moment at the crystal site $\vec{R}$ in the form:

$$\vec{\mu}(\vec{R}) = \mu \begin{pmatrix} 0 \\ 0 \\ e^{\imath \vec{R} \cdot \frac{\vec{c}^*}{2}} \end{pmatrix} \tag{9}$$

In this expression, magnetic structure is described in a simple way by the vector $\frac{\vec{c}^*}{2}$. This quantity, often denoted by the symbol $\vec{q}$, is known as the *modulation vector* of the magnetic structure. Inserting (9) into (8), the magnetic scattering length vector becomes:

$$\vec{b}_m(\vec{R}) = \frac{\gamma e^2}{2m_e c_0^2} \frac{\mu}{\mu_B} f(\vec{\kappa}) \begin{pmatrix} -e_1 e_3 \\ -e_2 e_3 \\ 1 - {e_3}^2 \end{pmatrix} e^{\imath \vec{R} \cdot \frac{\vec{c}^*}{2}} \tag{10}$$

Where $\hat{\kappa} = (e_1, e_2, e_3)$. The co-ordinates refer to a Cartesian system with the axes parallel to the a, b and c directions of the crystal.

To calculate the scattering cross-section from (6), we must insert the sum of the nuclear scattering length and the magnetic scalar product, $\vec{\sigma} \cdot \vec{b}_m(\vec{R})$:

$$\frac{d\sigma}{d\Omega}^{el} = \left| \sum_{\vec{R}} \left\{ b_{\vec{R}} + \vec{\sigma} \cdot \vec{b}_m(\vec{R}) \right\} e^{\imath \vec{\kappa} \cdot \vec{R}} \right|^2 \tag{11}$$

We readily see that the squared sum splits into three terms: One containing purely nuclear scattering, another containing only magnetic scattering, and finally an interference term containing the product $b_{\vec{R}} \vec{\sigma} \cdot \vec{b}_m(\vec{R})$. In an unpolarized beam of

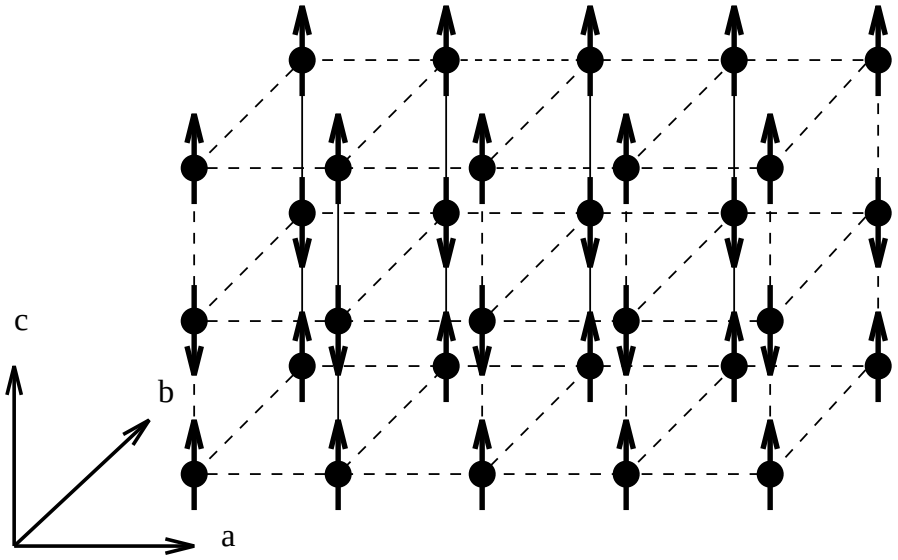

Figure 3. A simple cubic antiferromagnetic crystal.

neutrons, the last term will average out leaving no possibility of interference between the nuclear and the magnetic part of the scattering. For the purely magnetic term, we get:

$$\frac{d\sigma}{d\Omega}^{el}_{magn} = \left(f(\vec{\kappa}) \frac{\gamma e^2}{2 m_e c_0^2} \frac{\mu}{\mu_B} \right)^2 2(1 - {e_3}^2) \left| \sum_{\vec{R}} e^{\imath(\vec{\kappa} + \frac{\vec{c}^*}{2}) \cdot \vec{R}} \right|^2 \tag{12}$$

The structure of the squared sum factor in this expression is quite analogous to the corresponding term in the case of nuclear scattering. However, in the magnetic case, the $\vec{\kappa}$ has been substituted by $\vec{\kappa} + \vec{c}^*/2$. From this observation, it immediately follows that the positions of peaks in the cross-section *vs.* momentum transfer have been shifted away from the reciprocal lattice points by the modulation vector $\vec{c}^*/2$. The same is true for other modulated magnetic structures: The reasoning given above works analogously for a sinusoidal modulation (such a modulation is viewed as a combination of two complex exponentials giving rise to a magnetic satellite on either side of each nuclear peak), and we may regard any magnetic structure as a Fourier sum of such plain sinusoidal modulations. We briefly mentioned above the importance of the geometric factor in the magnetic scattering length vector. For the simple magnetic structure of Fig. 3, the geometric factor shows up in the scattering cross-section as $2(1 - {e_z}^2)$. This factor clearly reflects the symmetry of the magnetic structure itself. Hence, from a measurement of the cross-section we might have deduced the orientation of the spins in the crystal. When dealing with more complicated structures, such a determination of the spin configuration may be considerably less straight forward.

3 Polarized neutron beams

In the previous section, we assumed an unpolarized incident beam of neutrons in our application of the magnetic scattering length vector. When controlling the polarization of the incident neutron beam and measuring the polarization state of the scattered neutrons, additional information may become available. Firstly, the application of beam polarization and polarization analysis may help to solve the spin structure. Secondly, by the polarization technique it is possible to separate different contributions to the scattering cross-section. I the present work, polarized neutron beams are used in combination with small angle neutron scattering (SANS) to determine the chirality of a long period magnetic structure in MnSi.

The theory needed for the interpretation of full three-dimensional beam polarization and polarization analysis was presented by Halpern and Johnson [20] in 1939. An experimental apparatus for routine neutron scattering measurements with one-dimensional beam polarization and polarization analysis was developed and implemented at the High-Flux Isotope Reactor of Oak Ridge National Laboratory by Moon, Riste and Koehler [40]. In this paper, the authors work out a very convenient one-dimensional version of the original Halpern-Johnson theory. The first step in formulating the theoretical framework for scattering experiments using polarized neutrons is a revision of the neutron-atom interaction potential. For the scattering of a neutron from a single nucleus with a non-zero spin, there will be two different scattering lengths according to whether the spins of the nucleus and the neutron align parallel or anti-parallel. If we denote the nuclear scattering lengths for the parallel and anti-parallel alignment by b^+ and b^-, respectively, we may write the actual nuclear scattering length as:

$$\frac{b^+(I+1)+b^-I}{2I+1}+\frac{b^+-b^-}{2I+1}\vec{I}\cdot\vec{\sigma}=b+B\vec{I}\cdot\vec{\sigma} \tag{13}$$

where $\vec{I}$ is the nuclear spin operator and $\vec{\sigma}$ is the normalized neutron spin operator introduced in the previous section. The magnetic scattering length has already been presented in a form involving neutron spin. To simplify notation and follow [40], we shall write the magnetic scattering length as

$$-p\vec{S}_\perp\cdot\vec{\sigma} \tag{14}$$

where the factor p contains all the prefactors of the expression (8) including the magnitude of the atomic magnetic moment and $\vec{S}_\perp$ is a short-hand notation for the vector projection $(\hat{\mu}-\hat{\kappa}(\hat{\kappa}\cdot\hat{\mu}))$ Calculating a scattering cross-section in the Born-approximation involves (as indicated in equation (5)) the calculation of matrix elements of the scattering potential between initial and final states of both neutron and scattering system:

$$\left(\frac{d^2\sigma}{d\Omega dE}\right)^{s,s'}\propto\sum_\lambda P_\lambda\sum_{\lambda'}\frac{k'}{k}\delta(\Delta E_N-\Delta E)$$
$$\times\left|<\lambda',s'|\sum_{\vec{r}}e^{\imath\vec{\kappa}\cdot\vec{r}}(b_{\vec{r}}+(B_{\vec{r}}\vec{I}_{\vec{r}}-p_{\vec{r}}\vec{S}_{\perp,\vec{r}})\cdot\vec{\sigma})|\lambda,s>\right|^2 \tag{15}$$

where the quantum numbers λ and λ' refer to the initial and final states of the scattering system. Similarly, the quantum numbers s and s' refer to the initial and final spin states of the neutron. P_λ is the probability of finding the scattering system in the initial state λ. In the energy conserving δ-function, ΔE_N and ΔE denotes the energy change of the neutron and the scattering system, respectively. An index $\vec{r}$ has been added on the scattering length to denote atomic site.

Throughout this section, the site index is omitted when not explicitly needed for summation etc. By inserting the Pauli matrices, we may readily calculate the spin part of the matrix elements:

$$U^{s,s'} =< s'|b + (B\vec{I} - p\vec{S}_\perp)\cdot\vec{\sigma}|s > \tag{16}$$

Since we only consider incident polarization and polarization analysis with respect to one direction (say z), we have four combinations of incident and scattered neutron spin state:

$$\begin{aligned} U^{+,+} &= b + BI_z - pS_{\perp,z} \\ U^{-,-} &= b - BI_z + pS_{\perp,z} \\ U^{+,-} &= B(I_x + \imath I_y) - p(S_{\perp,x} + \imath S_{\perp,y}) \\ U^{-,+} &= B(I_x - \imath I_y) - p(S_{\perp,x} - \imath S_{\perp,y}) \end{aligned} \tag{17}$$

To include the states of the scattering system, we introduce (still following [40]) the notation:

$$\begin{aligned} \tilde{A}_{\vec{r}} &= < \lambda'|B\vec{I}_{\vec{r}} - p_{\vec{r}}\vec{S}_{\perp,\vec{r}}|\lambda > \\ \tilde{b}_{\vec{r}} &= < \lambda'|b_{\vec{r}}|\lambda > \end{aligned} \tag{18}$$

The polarization of the incident beam is characterized by $P_0 = n_+ - n_-$ with n_+ and n_- denoting the fraction of incident neutrons having spin up and spin down along z. When this notation is inserted into the expression (15), we obtain:

$$\begin{aligned} \frac{d^2\sigma}{d\Omega dE} &= \sum_{\lambda,\lambda'} P_\lambda \frac{k'}{k} \sum_{\vec{r},\vec{r}'} \Big[e^{\imath\vec{\kappa}\cdot(\vec{r}-\vec{r}')} \Big\{ \tilde{b}_{\vec{r}}\tilde{b}^*_{\vec{r}'} + \tilde{A}_{\vec{r}}\cdot\tilde{A}^*_{\vec{r}'} \\ &\quad + P_0\hat{z}\cdot\Big(\tilde{b}_{\vec{r}}\tilde{A}^*_{\vec{r}'} + \tilde{A}_{\vec{r}}\tilde{b}^*_{\vec{r}'} - \imath(\tilde{A}_{\vec{r}}\times\tilde{A}^*_{\vec{r}'})\Big)\Big\}\Big] \\ &\quad \times\delta(\Delta E_N - \Delta E) \end{aligned} \tag{19}$$

In the above expression, the four terms in the scattering cross-section representing each of the possible combinations of initial and final neutron spin state have been weighted with the appropriate fractions of spin up and spin down and summed. Alternatively, we may add the non spin-flip terms and subtract the spin-flip terms to get the polarization P_f of the scattered beam:

$$\begin{aligned} P_f\frac{d^2\sigma}{d\Omega dE} &= \sum_{\lambda,\lambda'} P_\lambda \frac{k'}{k} \sum_{\vec{r},\vec{r}'} \Big[e^{\imath\vec{\kappa}\cdot(\vec{r}-\vec{r}')} \Big\{ \hat{z}\cdot\Big(\tilde{b}_{\vec{r}}\tilde{A}^*_{\vec{r}'} + \tilde{A}_{\vec{r}}\tilde{b}^*_{\vec{r}'} + \imath(\tilde{A}_{\vec{r}}\times\tilde{A}^*_{\vec{r}'})\Big) \\ &\quad + P_0\Big(\tilde{b}_{\vec{r}}\tilde{b}^*_{\vec{r}'} + \tilde{A}_{\vec{r},z}\cdot\tilde{A}^*_{\vec{r}',z} - \tilde{A}_{\vec{r},x}\cdot\tilde{A}^*_{\vec{r}',x} - \tilde{A}_{\vec{r},y}\cdot\tilde{A}^*_{\vec{r}',y}\Big)\Big\}\Big] \\ &\quad \times\delta(\Delta E_N - \Delta E) \end{aligned} \tag{20}$$

From the equations (19) and (20) a number of important results are immediately derived. Firstly, we note that the polarization of an unpolarized beam ($P_0 = 0$; $P_f \neq 0$) may occur if some axial vector is built into the scattering system. If the system is ferromagnetically ordered, the terms containing the product of $\tilde{b}$ and $\tilde{A}$ are able to polarize the scattered beam. In a helical magnetic structure, beam polarization is represented by the cross product term $\tilde{A}_{\vec{r}}\times\tilde{A}^*_{\vec{r}'}$. Secondly, an incident polarized neutron beam is useful even without polarization analysis. The scattering cross-section is seen to depend on the incident polarization. As an example, we may deduce the helicity of a helical magnetic structure from the difference in cross-section for up and down incident polarization. Thirdly, it is noted that both the scalar part of the nuclear scattering represented by $\tilde{b}$ and the sample nuclear

and electronic spin parallel to the direction of polarization preserve the incident polarization (both components appear with a positive sign in the expression for polarization of the scattered beam). Conversely, nuclear and electronic spin components perpendicular to the direction of incident polarization rotate the neutron polarization.

Part II
$DyFe_4Al_8$

The compounds of the family MFe$_4$Al$_8$, where M is either a rare earth or an actinide element have attracted significant interest over the last couple of decades as candidates for new high T_c magnetic materials. A number of different techniques have been chosen for the studies, but a very confusing and contradicting picture of the magnetic properties has emerged. In this chapter, we describe a series of single crystal diffraction experiments on $DyFe_4Al_8$ using neurons and X-rays. The Fe-sublattice orders at a temperature of 180 K with the spins forming a cycloidal structure in the basal plane of the *bct* chemical unit cell. The Fe-magnetic structure is such that the resulting molecular field at the Dy-sites is rather small resulting in an ordering temperature of only 25 K for the Dy-sublattice. At temperatures below $\approx$ 15 K, higher order harmonics develop along with a significant diffuse magnetic scattering. With an external magnetic field of less then 1 T, one may quench the modulation of the Dy-moments while little effect is observed in the scattering from the Fe-sublattice.

4 Previous studies

In this section, we briefly summarize some of the most important previous work on the compounds MFe$_4$Al$_8$. Note, that powder samples were used in most of the referred experimental studies. The literature in the field is quite substantial, and no attempt has been made do justice to all the contributors.

The crystal structures of MFe$_4$Al$_8$, M = Y, La, Ce, Pr, Nd, Sm, Gd, Tb, Dy, Ho, Er, Tm, Yb, Lu and Th were solved by Buschow and coworkers [9] using powder X-ray diffraction. In all the cases, the structure is body centered tetragonal with the space group $I4/mmm$. More details on this structure are given in section 5.

In a paper by Buschow and van der Kraan [8], the magnetic properties of the series MFe$_4$Al$_8$, M = La, Ce, Pr, Nd, Sm, Gd, Tb, Dy, Ho, Er, Tm, Yb, Lu, Y and Th) have been investigated by measurements of bulk magnetization (all the compounds) and ^{57}Fe Mössbauer spectroscopy (all the compounds except M = Pr, Sm, Dy, Ho and Yb). In the curves of inverse susceptibility *vs.* temperature a maximum is observed for all compounds in the temperature range between 100 K and 200 K. This is interpreted as the onset of an antiferromagnetic ordering of the Fe sublattice. For the Y, La, Ce, Lu and Th compounds no further maxima are observed when lowering the temperature, and the authors conclude that in those cases no ordered moment exists at the rare earth/actinide site. In the cases of M = Gd, Tb, Dy, Ho and Er, estimates of the rare earth moment slightly below the free-ion values are extracted from the slope of the inverse susceptibility at temperatures below the Fe ordering. In the remaining compounds, the low temperature susceptibilities were strongly dependent on field and on the annealing treatment in the sample preparation. These effects were attributed to partial disorder in the Fe occupation, i.e. some of the Fe atoms are occupying Al sites and *vice versa*. From the Mössbauer measurements, the ordering temperatures of the Fe sublattice are found in the region 135 K $< T_N <$ 200 K for all compounds investigated by this technique. A simple molecular field (MF) model is developed, where the system is described as 3 interacting sublattices: Two antiferromagnetically coupled Fe sublattices and a third M sublattice. Approximate expressions for

the inverse susceptibility are derived for the temperature regions above and below the ordering of the Fe. From the data of selected samples, values of the molecular field constants are derived concluding that the absolute value of the MF parameter of the M and Fe sublattices is up to half the value of the Fe-Fe parameter. It is claimed that a general trend exists in the sign of the M-Fe coupling. When M is one of the light rare earth elements, the coupling between M and Fe should be ferromagnetic whereas it is antiferromagnetic in the heavy end of the rare earth series. However, this rule is only supported by quoted values of the M-Fe molecular field parameter for M = Gd and Nd. The M-M coupling is assumed to be negligible. This assumption is justified by an analogy with the system $GdMn_4Al_8$, where the susceptibility *vs.* temperature is found to be linear, and measurements on YMn_4Al_8 have shown that Mn carries no moment.

Many of the results of [9] and [8] were confirmed in a paper by Felner and Norwik [14], where compounds of the type $M Fe_4Al_8$ were investigated by X-rays, magnetization measurements and Mössbauer spectroscopy. In contrast to the authors of [8], Felner and Norwik claim that in those compounds where both the Fe and the M sublattices form ordered magnetic structures, the ordering of the M sublattice is *antiferromagnetic*. Their conclusion is based on relatively small magnetic moments induced by a field of 4 mT at 4.1 K. Furthermore, based on the ^{57}Fe Mössbauer spectra of $GdFe_4Al_8$, the authors point out the possibility that the ordering of the Fe sublattice may not be a simple antiferromagnetic structure. However, it is also noted that the observations leading to this point could arise from partial occupation of the Al sites by Fe.

The Mössbauer measurements of Buschow *et al.* [8] were continued by Gubbens, van der Kraan and Buschow [18] by the application of ^{169}Tm and ^{161}Dy Mössbauer spectroscopy to the compounds $TmFe_4Al_8$ and $DyFe_4Al_8$, respectively. By a rather involved analysis of the data, the authors [18] reach the conclusion that in $DyFe_4Al_8$, the Dy sublattice orders at (43 ± 8) K with the moments along the crystallographic c-axis. In the case of $TmFe_4Al_8$, no sharp transition to an ordered state occurs. Again, this effect is ascribed to the partial disorder of the Fe/Al occupancies. The Tm ordering temperature is estimated as (2 ± 2) K with the moments in the basal plane.

Using powder neutron diffraction in combination with the previously used techniques, Gal *et al.* [15] claim that $HoFe_4Al_8$ exhibits some of the irreversible and time dependent properties characteristic of a spin glass. Due to the values of the scattering lengths involved in the neutron scattering cross-section of the Ho-system, nuclear scattering is virtually absent at the (1 1 0)-position. This means that the (1 1 0)-reflection is a very sensitive probe to ferromagnetic ordering of the Ho moments (see section 5). In the experiment, the authors observe a non-reproducible ferromagnetic alignment of the Ho moments. Furthermore, in applied magnetic fields of 2 T - 6 T, they observe a formation of ferromagnetic ordering of the Ho-moments, which is preserved for many hours after the field has been turned off. When warming up after turning off the field, the (110)-peak signalizing the alignment of the Ho-moments fades away at a temperature between 40 and 70 K depending on the size of the originally applied field. Already in the paper [8] it was noted, that in those of the systems possessing magnetic moment at the M-site, the dependence of magnetization upon temperature changed when the sample was field cooled prior to the measurement. This effect is confirmed by Gal and coworkers [15] and together with apparently irreversible features in the ^{57}Fe Mössbauer spectra, this is taken as further support for the spin glass interpretation. Several places in this paper, the appearance of magnetic satellites in the neutron scatter-

ing powder pattern is mentioned. The discussion seems, however, not very clear at this point. In the beginning of the paper, it is stated that satellites are observed at temperatures below 180 K with some time and thermo-magnetical history dependence in the temperature range down to 20 K. Later in the paper, it is stated that no magnetic phase transitions are observed with neutrons in the vicinity of 180 K, and that the Fe sublattice is not magnetically ordered above approximately 20 K. In relation to the decay of the field induced intensity at the (1 1 0)-position, the authors talk about a transition from an aligned to a random state, and they note that the decay of the (1 1 0)-peak is associated with a reappearance of the magnetic satellites of the (2 2 0) and (2 0 0) observed at zero field. Thus, the authors propose a model of the magnetic properties of $HoFe_4Al_8$ strongly in opposition to the conclusions drawn in the preceding work referred: At approximately 180 K, the Fe sublattice freezes with a random spin orientation and at approximately 20 K the Fe orders in a modulated structure. The Ho never orders, but at low temperature and zero field, the Ho moments are in a frozen state. At the end of the paper, the authors mention that preliminary measurements on the Tb, Er and Dy systems show the same characteristics as those reported for $HoFe_4Al_8$.

The idea of a spin glass is further developed in a paper by Talik, Szade and Heimann [48]. In this case the measurements of electric conductivity and magnetic DC and AC susceptibility were performed on a *single crystal* of $DyFe_4Al_8$. In this work, the thermo-magnetical history effects in the DC susceptibility are reproduced, and a further indication of spin glass character, a cusp in the AC susceptibility, is reported. Furthermore, the measurements of DC susceptibility on the oriented sample reveals a strong magnetic anisotropy with the easy direction in the basal plane of the *bct* structure.

In the single crystal diffraction experiments reported in the remaining of this chapter, we try to clear some of the contradiction outlined above. Presently, not all the questions are resolved, but it appears clear that single crystal samples and microscopic techniques indeed are necessary when dealing with systems as complicated as the MFe_4Al_8 compounds.

5 Structure refinement

The first single crystal diffraction experiment on $DyFe_4Al_8$ was a structure refinement [42] using the Risø TAS2 4-circle diffractometer. Though the structure was known from [9] and other works, a careful characterization of the sample using neutrons was decided partly to check for disorder in the Fe and Al occupation and partly to obtain correction parameters needed for the further work. The sample used in all the neutron and X-ray experiments described in the remaining of this section was prepared by E. Talik of the University of Selesia, Katowice, Poland, and it is identical to the sample described in [48]. The TAS2 instrument is installed at a thermal neutron beam and for this refinement a Be (0 0 2) monochromator was used to produce a beam of 1 Å incident neutrons. The sample was mounted in a closed cycle cryostat allowing measurements at temperatures down to approximately 20 K. A total of 492 reflections were collected at room temperature. The unit cell is found to be body centered tetragonal with the space group $I4/mmm$. In the refinement of the structure, the effect of absorption was included as was extinction using a Becker-Coppens model with Lorentzian mosaic spread. The results of the refinement are summarized in Table 5. No disorder in the occupation

of sites was found. From Fig. 4, it is clear that each Dy atom in the Wyckoff $2a$-position is surrounded by a cage of Fe-atoms. This structural property common to all the members of the $M\mathrm{Fe_4Al_8}$-family turns out to play a key role for the magnetism of the compounds. Although the interaction between the M and Fe sublattices is comparable to the Fe-Fe sublattice interaction [8], a simple antiferromagnetic alignment of the Fe moments will lead to a vanishing molecular field at the M site. From the selection rules of the space group it follows, that the Fe sites can only contribute to the scattering at reflections with even values of all the indices.

Atom	Site	x	y	z
Dy	$2a$	0	0	0
Fe	$8f$	$\frac{1}{4}$	$\frac{1}{4}$	$\frac{1}{4}$
$\mathrm{Al_I}$	$8i$	0.3414(5)	0	0
$\mathrm{Al_{II}}$	$8j$	0.2794(5)	$\frac{1}{2}$	0

$R(F) = 2.7\%$; $\eta = 0.65'$

Cell parameters (RT): $a = b = 8.731$ Å, $c = 5.039$ Å.

Table 2. Structural parameters of $\mathrm{DyFe_4Al_8}$. *The site labels refer to the Wyckoff notation and* η *denotes the Lorentzian mosaic spread used for the extinction correction.*

In spite of the large neutron absorption cross-section of naturally abundant Dy (940 barns at 25 meV neutron energy), it was possible to fit the structure without absorption corrections leading to similar results and an R-factor of 4.5%.

In the 4-circle experiment, magnetic satellites around the (odd odd even) nuclear reflections were observed at temperatures below 170 K and satellites around other nuclear reflections were observed from about 30 K. However, due to the experimental conditions (the poor resolution of the instrument and the high base temperature of the cryostat), a more detailed study of the magnetism was not feasible.

6 A magnetic neutron scattering study

After the structure refinement, an experiment dedicated to the study of the magnetism of $\mathrm{DyFe_4Al_8}$ was conducted at the D10 diffractometer at the Institute Laue Langevin, Grenoble, France in collaboration with J. A. Paixão, University of Coimbra, Portugal, G. H. Lander, EITU, Karlsruhe, Germany and Bente Lebech, Risø, Denmark. The D10 is a very flexible instrument with several monochromators mounted in a carrousel, an Eulerian cradle, a wide range of sample environments and the choice between two different detectors to either have a double axis/4-circle scattering geometry or a triple axis setup with an analyzer crystal. The available sample environments include a ^{4}He flow cryostat with a base temperature of approximately 1.6 K and a dilution fridge going down to 130 mK. The general layout of the D10 instrument is illustrated in Fig. 5.

Since very little knowledge about the magnetic structures of $\mathrm{DyFe_4Al_8}$ was available prior to the experiment, it was planed as a combination of a survey in a large portion of reciprocal space with 1.26 Å incoming neutrons and a more detailed study at a somewhat higher $\vec{q}$-resolution with neutrons at 2.36 Å wavelength. During the entire experiment, the diffractometer was operated in double axis/4-circle mode with the flow-cryostat.

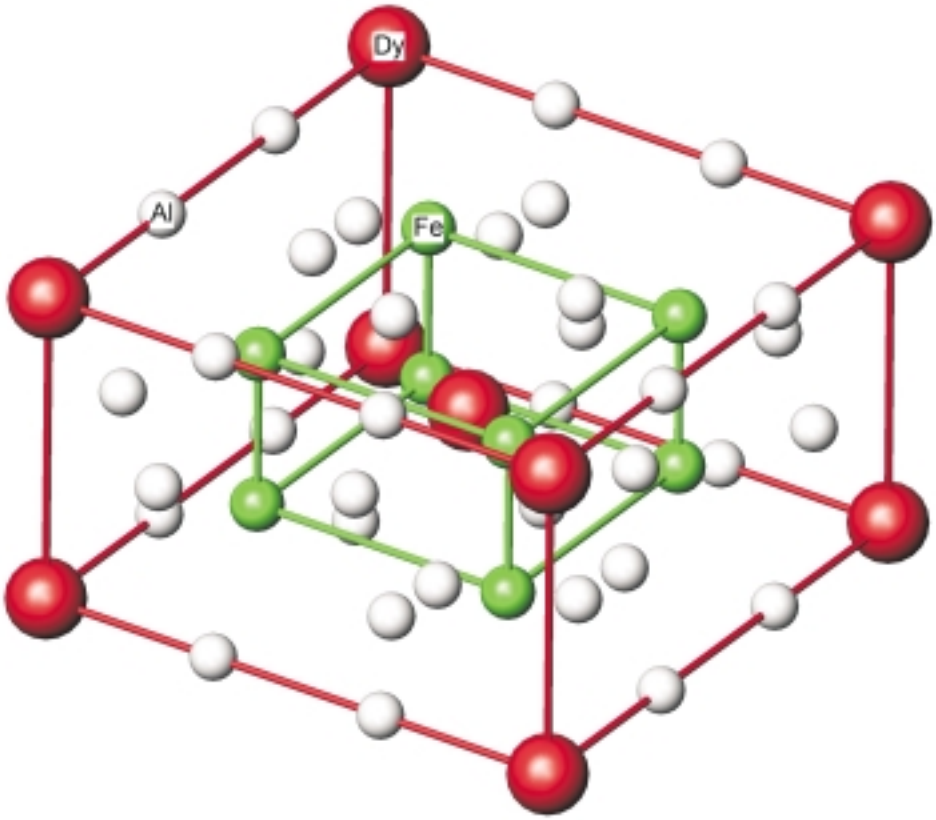

Figure 4. The unit cell of $DyFe_4Al_8$.

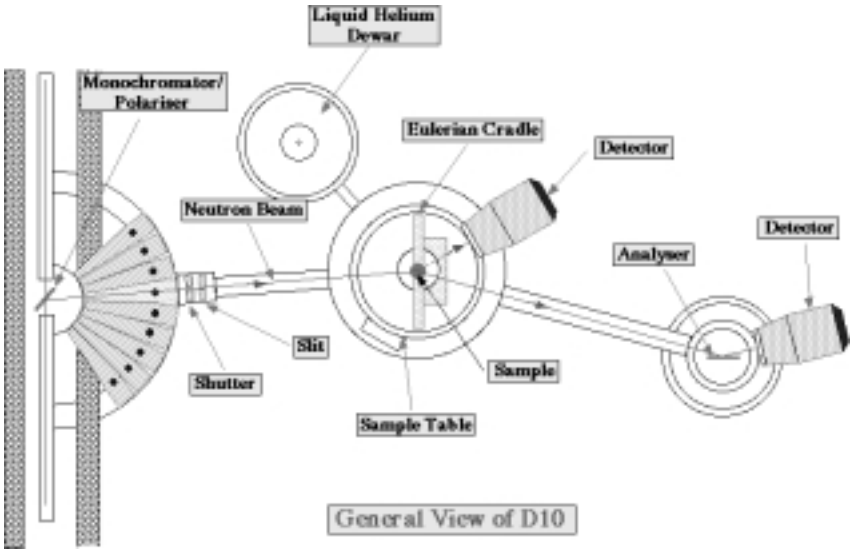

Figure 5. The general layout of the 4-circle diffractometer D10 at the Institute Laue Langevin. Note the special construction with a standard detector for diffraction and a separate section for detection with energy analysis of the scattered neutrons. The figure was reproduced from the ILL "Guide to Neutron Facilities" available at the ILL WWW-server, URL http://www.ill.fr.

6.1 The survey measurement

In the first part of the D10 experiment using 1.26 Å incident neutrons from the (0 0 2)-reflection of a Cu monochromator, scans in the (h k 0) plane of reciprocal space were performed in the region $-3.5 < h < 3.5$, $-3.5 < k < 3.5$ primarily at temperatures below 10 K. In the scans performed, magnetic satellites were observed along the <1 1 0>-directions, corresponding to a modulated magnetic structure with a fundamental modulation vector $\vec{q} = (\xi\ \xi\ 0)$, where $\xi \approx 0.13$. In addition to the fundamental satellites, peaks at positions corresponding to 3'rd and 5'th order satellites were observed. The satellites clearly divide into two distinct classes: A set of strong peaks around the nuclear reflections of type (odd odd even) and a set of considerably weaker peaks positioned around the remaining allowed Bragg peaks. When warming up to 50 K, the weak satellites disappeared and only the (odd odd even)-type was left. Since we know from the ^{57}Fe Mössbauer experiment, that the Fe sublattice is ordered at high temperature, and since the (even even even) reflections are the only ones allowing scattering from the Fe sites, the modulation of the Fe sublattice must be of the type $(1+\xi\ 1+\xi\ 0)$. By inspection of the unit cell it is clear, that this addition of the vector (1 1 0) to the modulation vector corresponds to an additional change of the phase by π when going from one Fe layer to the next along the [1 1 0]-direction. To test for a net moment on the Dy-sites, the count rate at the peak of the (1 $\overline{1}$ 0)-reflection was measured as a function of temperature in the interval 5 K to 14 K. No significant change in this count rate was observed. At the end of the run, a few scans along <1 1 0>-directions were performed with $l \neq 0$ and around the (7 7 0) nuclear peak. Due to the magnetic form factor, none of the known magnetic satellites were observed around (7 7 0), but satellites at the 2'nd order position had appeared. Due to their increasing intensity with momentum transfer, these satellites are believed to arise from a modulation in the atomic positions induced by the magnetic structure. In order to save time for work at higher resolution, it was decided to perform the survey scans in relatively coarse steps. This means, that estimates of the integrated intensities are likely to be unreliable, and a preliminary analysis of the intensities of nuclear reflections showed a lack of internal consistency.

6.2 The measurements at higher resolution

In the second part of the D10 experiment, we aimed for a more detailed determination of the modulation vector and satellite intensities *vs.* temperature. This time, a more restricted set of scans was performed with 2.36 Å incident neutrons from the (0 0 2)-reflection of a pyrolythic graphite monochromator. The switching to longer wavelength neutrons yields a higher resolution with the access to a smaller part of reciprocal space as the pay-off. At temperatures between 1.8 K and 30 K, data were collected in scans around the (1 $\overline{1}$ 0), (2 $\overline{2}$ 0), ($\overline{1}$ 0 $\overline{1}$) and (1 $\overline{2}$ 1) reciprocal lattice points. At higher temperatures, only the Fe-satellites around (1 $\overline{1}$ 0) was measured, but in this case the momentum transfer was scanned both parallel and perpendicular to the reciprocal lattice vector. A map of the scans is shown in Fig. 6. The predominantly transverse scan modes were chosen to have a good resolution, in particular, to separate the close 3'rd and 5'th harmonics.

The data analysis

Each of the peaks in the data set collected at 2.36 Å was analyzed in two ways: The peak position was extracted by fitting the data points to the sum of a Gaussian and a straight line, and the integrated intensity was obtained both by a Gaussian

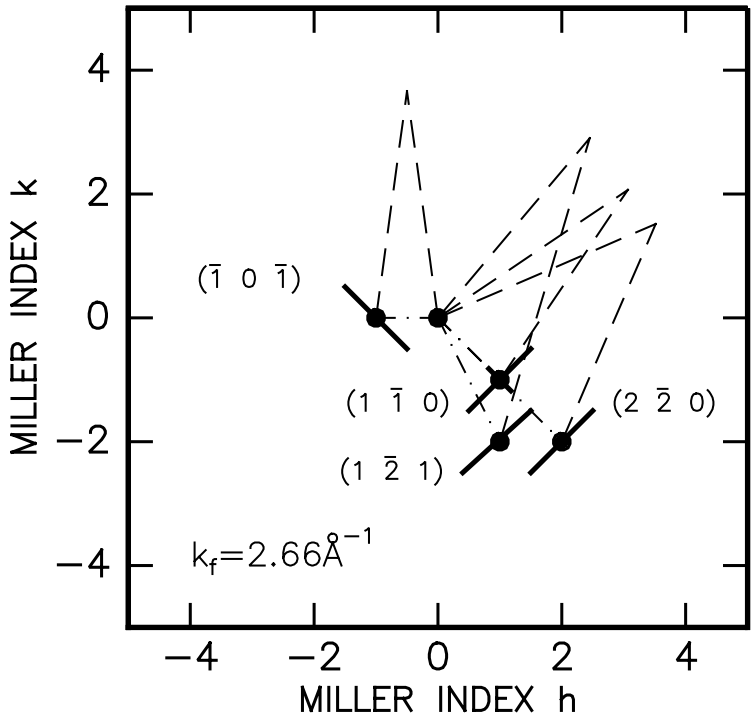

Figure 6. Vector diagram showing the scans in the part of the ILL-D10 experiment using 2.36 Å incident neutrons (graphite monochromator.) The solid lines indicate the scans whereas the dashed lines show the scattering triangle at the wavelength in question.

fit and by direct numerical integration.

In Fig. 7, the modulation vectors resulting from the peak fits are summarized. The error bars included are taken from the fitting algorithm. They only indicate the accuracy of the individual fits, and not systematic errors such as instrumental misalignment and offset in neutron wavelength. For the longitudinal scans along the [1 $\overline{1}$ 0] direction, the plotted values were extracted by taking the difference between the position of the $+\vec{q}$ and the $-\vec{q}$ satellites divided by the sum of the same positions. In this way, the values are compensated for the change in lattice parameter by temperature. This simple correction is possible only because the displacement of the satellites will be along the direction of scanning. In the remaining cases, where the scanning direction was not parallel to the reciprocal lattice vector midway between the two satellites, a displacement of the satellites will have components both parallel and perpendicular to the scanning direction. In fact, the relation between the true and the observed displacement of a satellite depends on the orientation of the resolution ellipsoid. Thus, for the satellites observed in the transverse scans, we simply plot half the difference between the fitted positions. This is the reason for the systematic offset between the ξ-values extracted from the two types of scans around (1 $\overline{1}$ 0). In the inset of Fig. 7, the ξ-values from all the non-longitudinal scans are shown in the low temperature regime. It is clear, that the overall scatter of the values is of the order 0.001 rlu. At temperatures above approximately 20 K, the length of the modulation vector seems to change with temperature in a continuous way. Although the steps in temperature are rather coarse, it is reasonable to assume that at high temperature, the period of the magnetic modulation is incommensurate with the chemical unit cell. At around

20 K, the period of the magnetic structure levels out in what is presumably a lock-in to a commensurate value. In the figure, the lock-in value appears to be close to 0.133, suggesting the simple rational number $\frac{2}{15} = 0.1333\ldots$ as the true low temperature value of the modulation vector elements. The value of $\xi = \frac{2}{15}$ corresponds to a phase shift of 48° when going from on Dy-layer to the next along a <1 1 0>-direction and repetition of the magnetic structure 4 times in 15 unit cells. From the considerations above, it is clear that when aiming at precise values of ξ, one should perform longitudinal scans, preferably including several Bragg peaks. To improve the resolution, one may apply an analyzer crystal.

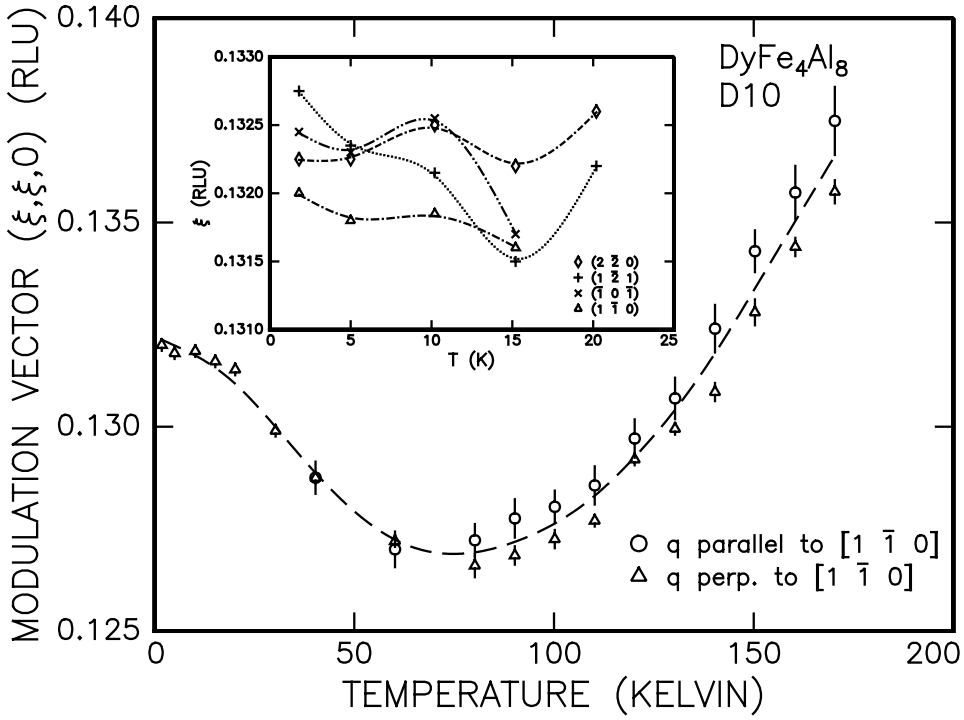

Figure 7. Magnetic modulation vector in reciprocal lattice units. The error bars of the data points in the main plot are calculated from fits. The dashed curves are guides to the eye. More details are given in the text.

When it comes to extracting and interpreting the intensities of the diffraction peaks, the details of the scan modes are once again of importance. The key issue of this part of the data analysis is to reduce the integrated intensities of the measured peaks to structure factors. In the general case, the instrumental effects on the measured intensities and line shapes are treated by introducing the resolution function of the instrument. If, however, one chooses the double axis geometry and works with a *relaxed* exit collimation, the treatment of the instrumental effects is strongly simplified [47]. In basic texts on scattering techniques or crystallography, it is shown that the differential cross-section for coherent, elastic scattering from a crystalline sample may be written as a sum of δ-functions:

$$\frac{d\sigma}{d\Omega} = \frac{(2\pi)^3 N}{v_0} \sum_{\vec{\tau}} \delta(\vec{\kappa} - \vec{\tau}) |F(\vec{\tau})|^2 \tag{21}$$

where the summation extends over all the reciprocal lattice vectors $\vec{\tau}$ of the crystal Bravais lattice, $\vec{\kappa}$ is the wave vector transfer, $F(\vec{\tau})$ is the structure factor, N is the number of unit cells in the sample crystal and v_0 is the volume of the unit cell. We now consider a scattering experiment as shown in Fig. 8. The incident beam is well collimated and monochromatic, but at the exit beam the collimation defined by the sample size and the aperture in front of the detector is sufficiently relaxed

to allow detection of all neutrons scattered by the sample when a single reciprocal lattice vector is brought in the position of reflection. Suppose, we put the detector at the nominal scattering angle, θ_1 of a particular reciprocal lattice vector, $\vec{\tau}_1$. We ask for the integrated intensity of a *rocking scan*, that is, a scan, where the crystal is rotated around an axis perpendicular to the scattering plane defined by the monochromator, the sample and the detector. Since only the selected reciprocal lattice vector, $\vec{\tau}_1$ will be brought in position for reflection, only one of the terms in the sum of δ-functions (21) may contribute to the signal. If the sample orientation is represented by ψ, the angle between the reciprocal lattice vector $\vec{\tau}_1$ and the direction of the incident beam, $\vec{k}$, the integral of the rocking scan is written as:

$$\begin{aligned} I &= \Phi \int_0^\pi d\psi \int d\Omega \frac{d\sigma}{d\Omega} \\ &= \Phi |F(\vec{\tau}_1)|^2 \frac{(2\pi)^3 N}{v_0} \int_0^\pi d\psi \int_{4\pi} d\Omega \delta(\vec{\kappa} - \vec{\tau}_1) \end{aligned} \tag{22}$$

where we have introduced the incident flux Φ. Note, that whereas the integration with respect to ψ corresponds to the physical rotation of the crystal, the integration with respect to the solid angle Ω represents the integration performed by the detector. That is, the integration with respect to Ω is equivalent to the assumption of relaxed exit collimation. To evaluate the integral of the 3-dimensional δ-function, we introduce the vector $\vec{\rho} = \vec{k} - \vec{\tau}_1$ allowing us to simplify the Ω-integration. Since the integral:

$$\int_{4\pi} d\Omega \delta(\vec{\kappa} - \vec{\tau}_1) = \int_{4\pi} d\Omega \delta(\vec{\rho} - \vec{k}') \tag{23}$$

must cancel unless $|\vec{\rho}| = |\vec{k}'|$ we may simply write:

$$\int_{4\pi} d\Omega \delta(\vec{\rho} - \vec{k}') = c\delta(\rho^2 - {k'}^2) \tag{24}$$

The value of the constant c is found be integrating over the length of $\vec{k}\,'$:

$$1 = \int dk' {k'}^2 \int_{4\pi} d\Omega \delta(\vec{\rho} - \vec{k}') = c \int d({k'}^2) \frac{k'}{2} \delta(\rho^2 - {k'}^2) = c\frac{\rho}{2} \tag{25}$$

giving $c = \frac{2}{\rho}$. Using this result for the integral of the intensity, I gives:

$$I = \Phi \frac{(2\pi)^3 N}{v_0} |F(\vec{\tau}_1)|^2 \int_0^\pi d\psi \frac{2}{\rho} \delta(\rho^2 - {k'}^2) \tag{26}$$

With the definition of $\vec{\rho}$ and ψ, we have:

$$\rho^2 - {k'}^2 = {\tau_1}^2 - 2k\tau_1 \cos\psi \tag{27}$$

and:

$$d(2k\tau_1 \cos\psi) = -2k\tau_1 \sin\psi d\psi \tag{28}$$

so:

$$I = \Phi \frac{(2\pi)^3 N}{v_0} \int_{-2k\tau_1}^{2k\tau_1} \frac{1}{k\rho\tau_1 \sin\psi} \delta({\tau_1}^2 - x) dx \tag{29}$$

There will be a contribution to the integral only when:

$$\tau_1 = 2k \cos\psi \tag{30}$$

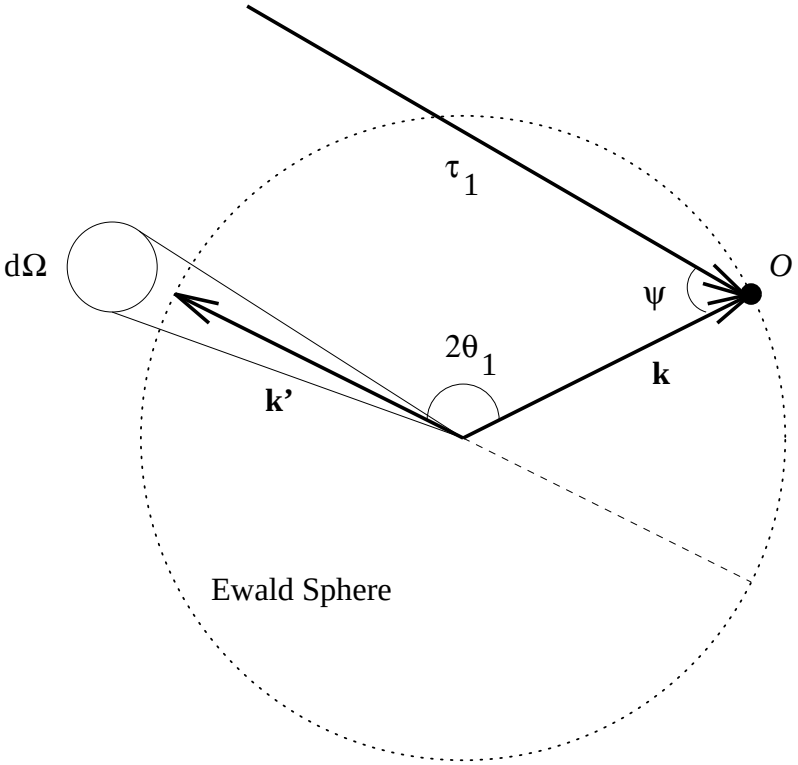

Figure 8. Vector diagram showing a rocking scan in the two axis geometry.

By inspecting Fig. 8 we note, that this condition is just equivalent to Bragg's law: $\psi = \frac{\pi}{2} - \theta_1$ with $2\theta_1$ being the scattering angle between $\vec{k}$ and $\vec{k}\,'$. We then reach the final result of the integration:

$$\begin{aligned} I &= \frac{(2\pi)^3 N}{v_0}\Phi|F(\tau_1)|^2\frac{1}{2k^3\sin\theta_1\cos\theta_1} \\ &= \frac{N}{v_0}\Phi|F(\tau_1)|^2\frac{\lambda^3}{\sin 2\theta_1} \end{aligned} \tag{31}$$

The factor $\frac{\lambda^3}{\sin 2\theta}$ is an example of what is generally known as the *Lorentz correction*. From the algebra above, it is clear, that the Lorentz factor represents the velocity by which we pass the scattering condition in a scan. When comparing intensities of Bragg peaks measured at different scattering angles or by different methods, it is crucial to take this effect into account. Because the correction turns out to be a simple factor in the case of a rocking scan, this is often the preferred mode of scanning in a crystallographic experiment. On a 4-circle machine (see Fig. 9 for the definition of the angles of the Eulerian cradle), one will often orient the crystal by the angles ϕ and χ with the χ-circle bisecting the incident and the scattered beam. During the scan, ϕ and χ are kept fixed while the circle is rotated to obtain the rocking curve. However, in some cases including studies of incommensurate magnetic structures, it is preferable to perform linear scans in reciprocal space. In this case, the scan may take a complicated path in the machine angles, and in the most general case, it is no longer possible to express the Lorentz correction as a simple factor. Instead one may transform the reciprocal lattice scan into a rocking scan by calculating the rotation of the crystal in the scattering plane from the values and the steps in all the instrument angles. An

expression for an instrumental geometry including tilting of the detector is given by [39]:

$$|F(\vec{\tau})|^2 \propto \sum_j I_j \frac{dz}{ds} \Delta s_j \tag{32}$$

where

$$\begin{aligned} \lambda \frac{dz}{ds} \Delta s_j &= -[\Delta\omega_j \sin\gamma \cos\nu + \Delta\chi_j \sin\omega \sin\nu \\ &\quad + \Delta\phi_j(\cos\chi \sin\gamma \cos\nu - \cos\omega \sin\chi \sin\nu)] \end{aligned} \tag{33}$$

The angles ω, χ and ϕ refer to the Eulerian cradle, ν is the detector tilt measured from the equatorial plane, i.e. the plane perpendicular to the ω-axis containing the sample and the monochromator, and γ is the angle between the incident beam and the project onto the equatorial plane of the direction to the detector. Note, that in the case of the simple rocking scan, the angular dependence of the expression (33) reduces to $\sin 2\theta$, and in the 4-circle case, where the detector tilt ν is missing, inserting $\nu = 0$ gives the relation

$$\lambda \frac{dz}{ds} \Delta s_j = -\sin 2\theta \, [\Delta\omega_j + \Delta\phi_j cos\chi] \tag{34}$$

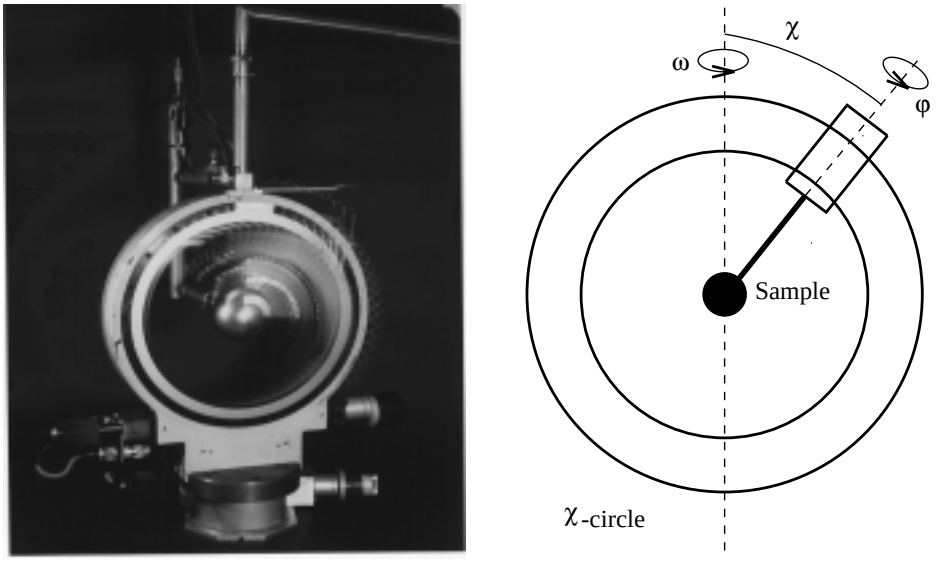

Figure 9. Principle of the Eulerian cradle. The left panel shows the Eulerian cradle of the D10 spectrometer with the dilution fridge mounted. In the right panel, the standard designation of the three orientation angles is shown.

From the considerations above, we may derive a most useful rule of thumb regarding the resolution in the double axis geometry with relaxed exit collimation: The long axis of the resolution ellipsoid must be along the direction in reciprocal space least sensitive to the scattering condition, i.e. along the tangent to the Ewald sphere. The angle between that direction and the reciprocal lattice vector in question is simply equal to the Bragg angle, θ. It then follows, that at small scattering angles, the direction of best resolution is close to perpendicular to the momentum transfer. Correspondingly, one will have the best resolution close to the longitudinal direction when working at high scattering angles.

In the present experiment on $DyFe_4Al_8$, the expressions (32) and (34) were used to reduce the intensities to squared structure factors. A special program was written to read the reciprocal lattice co-ordinates, the count rate and the 4 instrumental angles of each data point in the raw data files. By means of a pointing device

("mouse") the peak region was identified by the user on a plot of the raw data. A fixed number of points on each side of the peak region was used to estimate the background. By fitting the background points to a straight line, the background of each data point in the peak region was interpolated, and a background subtracted value of the integrated intensity was calculated directly from the data points using the trapez rule. From the standard deviation of the count numbers, the estimated error of the integral was calculated. For the background, the mean square deviation of the measured background from the interpolation line was used as an estimate of the background variance. It should be noted, that whenever possible, one should directly measure the background. In a magnetic diffraction experiment, that means performing identical scans above the ordering temperature. In the present case, however, it was realized, that a substantial component of diffuse scattering was developing below the nuclear peaks at low temperature. In order to get correct information about the long-range order structure of the system, this diffuse component must be subtracted as well as the true background.

To test the internal consistency of the measured intensities, we first compare the calculated integrals with the structure factor squared. Even with the 1 Å neutrons used in the structure refinement of section 5, severe extinction corrections were applied. The importance of the extinction effects increases with increasing wavelength. By application of the Becker-Coppens formalism implemented in the Cambridge Crystallography Subroutine Library (CCSL), the 1 Å extinction corrections obtained from the structure refinement were transformed to the neutron wavelength 2.36 Å. The comparison between extinction corrected intensities and the structure factors is shown in Table 3. As indicated in the table, the mean deviation of the measured intensities from the expected ones is 2%. It is, of course, dubious to deal with an R-factor based on only 4 reflections, and we shall merely take the result as an indication, that the nuclear intensities do not give reason for questioning the measured intensities in general.

$(h\ k\ l)$	$\lvert F(h\ k\ l)\rvert^2$	I_{calc}	$y \cdot I_{calc}$	I_{obs}	$\Delta(\%)$
$(1\ \overline{1}\ 0)$	5.96	1609	1321	1396	5.4
$(2\ \overline{2}\ 0)$	55.11	14868	7800	7710	1.2
$(\overline{1}\ 0\ \overline{1})$	5.80	1565	1308	1320	1.0
$(1\ \overline{2}\ 1)$	9.76	2632	2269	2253	0.7

$$R = \frac{1}{N}\sum_i \frac{|I^i_{obs} - I^i_{calc}|}{I^i_{obs}} = 2\%$$

Table 3. Comparison between the observed and calculated intensities of nuclear reflections. The extinction parameter y calculated by wavelength transformation of the TAS2 result is defined by $I_{obs} = y \cdot I_0$, where I_0 denotes the intensity of the reflection if no extinction was present. In the expression defining the R-factor, N denotes the number of observed reflections.

The ordering of Fe

Now turning to the the magnetic satellites, in Fig. 10 we plot the intensities of the 1'st order satellites observed around the $(1\ \overline{1}\ 0)$ nuclear reflection *vs.* temperature. We note, that since the modulation of the magnetic moment at the Fe sites has the additional π phase shift when going from one layer to the next along a <1 1 0>-direction, these satellites are sensitive to both the Dy and the Fe sites. The ordering of the Fe at approximately 180 K is clearly seen, and furthermore a steep increase in the intensity is observed around 20 K arising from the ordering of the Dy moments. We first concentrate on the high temperature regime. Here the two

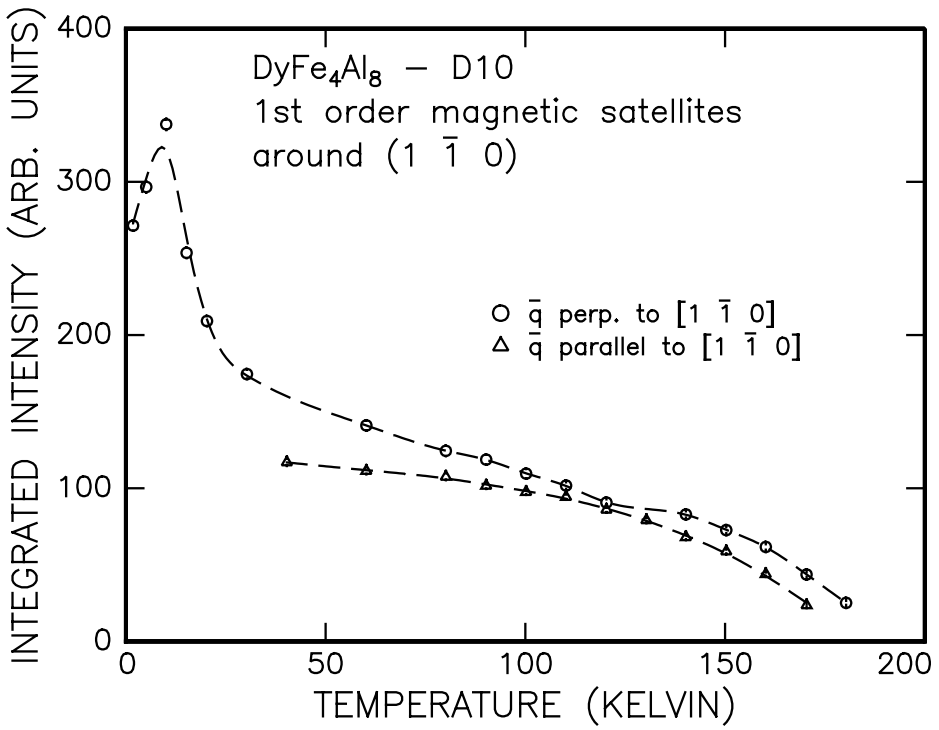

Figure 10. Integrated intensity of 1'st order magnetic satellites around the $(1\ \overline{1}\ 0)$*-peak. The dashed curves are guides to the eye.*

data sets represent the pair of satellites along and perpendicular to the $[1\ \overline{1}\ 0]$-direction. Assuming a single-$\vec{q}$ structure, the two sets of satellites originates from symmetry equivalent domains with the modulation along $[1\ \overline{1}\ 0]$ and [1 1 0]. We note, that the intensity of these two pairs of satellites is approximately identical. Since only the projection of the magnetic moment perpendicular to the momentum transfer contributes to the scattering length, this observation immediately rules out both the possibility of a longitudinal amplitude modulated structure and a transverse structure with the moments in the basal plane. The possibility of an amplitude modulated structure with the moments along the c-axis is unlikely. Partly because the magnetization measurements reported in [48] show that the easy directions are in the basal plane, and partly for reasons discussed in relation to the Dy structure. Assuming that the moments are (at least predominantly) in the basal plane, we are left with the possibility of moments rotating in the basal plane — a so-called *cycloidal* structure — and an amplitude modulated structure with the moments along the <1 0 0>-directions. To discuss the implication of these two structures, we must work out the detailed scattering cross-section for the two cases. Our starting point will be the expression for the magnetic scattering length vector discussed in the introduction of this thesis:

$$\vec{b}_m = \frac{\gamma e^2}{2m_e c_0^2}\frac{\mu}{\mu_B} f(\vec{\kappa})\,(\hat{\mu} - \hat{\kappa}(\hat{\kappa}\cdot\hat{\mu})) \tag{35}$$

and the equation for the differential scattering cross-section:

$$\frac{d\sigma}{d\Omega} = \left|\sum_{\vec{r}} \vec{b}_m(\vec{r}) e^{\imath\vec{\kappa}\cdot\vec{r}}\right|^2 \tag{36}$$

We introduce the elements e_1, e_2 and e_3 of the unit vector $\hat{\kappa}$ along the momentum transfer $\vec{\kappa}$:

$$\hat{\kappa} = \begin{pmatrix} e_1 \\ e_2 \\ e_3 \end{pmatrix} \tag{37}$$

referring to a Cartesian coordinate system with the x-, y- and z- axes along [1 0 0], [0 1 0] and [0 0 1], respectively. In the case of a basal plane cycloidal structure, we may write the magnetic moment at the position $\vec{r}$ as

$$\vec{\mu}(\vec{r}) = \mu\hat{\mu}(\vec{r}) = \mu \begin{pmatrix} \cos(\vec{q}\cdot\vec{r}+\phi_0) \\ \sin(\vec{q}\cdot\vec{r}+\phi_0) \\ 0 \end{pmatrix} \tag{38}$$

where $\vec{q}$ is the modulation vector and ϕ_0 is a phase constant. Rewriting the sine and cosine in terms of the complex exponential, the vector combination $\hat{\mu}-\hat{\kappa}(\hat{\mu}\cdot\hat{\kappa})$ takes the form:

$$\begin{aligned} \hat{\mu}-\hat{\kappa}(\hat{\kappa}\cdot\hat{\mu}) &= \frac{1}{2}e^{\imath(\vec{q}\cdot\vec{r}+\phi_0)} \begin{pmatrix} (1-e_1^2)+\imath e_1e_2 \\ -e_1e_2-\imath(1-e_2^2) \\ -e_3(e_1-\imath e_2) \end{pmatrix} \\ &\quad + \frac{1}{2}e^{-\imath(\vec{q}\cdot\vec{r}+\phi_0)} \begin{pmatrix} (1-e_1^2)-\imath e_1e_2 \\ -e_1e_2+\imath(1-e_2^2) \\ -e_3(e_1+\imath e_2) \end{pmatrix} \\ &= \frac{1}{2}e^{\imath(\vec{q}\cdot\vec{r}+\phi_0)}\vec{\alpha} + \frac{1}{2}e^{-\imath(\vec{q}\cdot\vec{r}+\phi_0)}\vec{\alpha}^* \end{aligned} \tag{39}$$

where the vector $\vec{\alpha}$ in the last expression is simply a short hand notation for the vector coefficient appearing in the first expression. Inserting the expression (39) into the basic equation of the cross-section (36) yields:

$$\begin{aligned} \frac{d\sigma}{d\Omega} &= \left(\frac{\gamma e^2}{4m_ec_0^2}\right)^2\left(\frac{\mu}{\mu_B}\right)^2|f(\vec{\kappa})|^2\cdot\left\{|\vec{\alpha}|^2\left|\sum_{\vec{r}}e^{\imath\vec{r}\cdot(\vec{\kappa}+\vec{q})}\right|^2 + |\vec{\alpha}|^2\left|\sum_{\vec{r}}e^{\imath\vec{r}\cdot(\vec{\kappa}-\vec{q})}\right|^2\right. \\ &\quad \left. + 2\cos(2\phi_0)\Re\left[\vec{\alpha}\cdot\vec{\alpha}\sum_{\vec{r}}e^{\imath\vec{r}\cdot(\vec{\kappa}+\vec{q})}\sum_{\vec{r}\,\prime}e^{\imath\vec{r}\,'\cdot(\vec{\kappa}-\vec{q})}\right]\right\} \end{aligned} \tag{40}$$

The last term containing the double sum may contribute only when the modulation vector, $\vec{q}$ equals half a reciprocal lattice vector of the Bravais lattice in question. That is, when the structure reduces to either a ferromagnetic or a simple antiferromagnetic (+-) configuration. Since this is not the case for the system considered, we proceed without the cross term. To further manipulate the remaining sum-terms, we write the atomic position $\vec{r}=\vec{R}+\vec{d}_j$ as a sum of a lattice vector $\vec{R}$ and a vector $\vec{d}_j$ of the crystal structure basis:

$$\begin{aligned} \left|\sum_{\vec{r}}e^{\imath\vec{r}(\vec{\kappa}\pm\vec{q})}\right|^2 &= \left|\sum_{\vec{R}}e^{\imath\vec{R}(\vec{\kappa}\pm\vec{q})}\right|^2\left|\sum_{j}e^{\imath\vec{d}_j(\vec{\kappa}\pm\vec{q})}\right|^2 \\ &= \frac{(2\pi)^3N}{v_0}\sum_{\vec{\tau}}|F(\vec{\tau})|^2\delta(\vec{\kappa}\pm\vec{q}-\vec{\tau}) \end{aligned} \tag{41}$$

In this manipulation we have just used the standard expression in δ-functions of the Bravais lattice sum. The structure factor $F(\vec{\tau})$ is simply the phase summation over those of the sites in the unit cell carrying magnetic moment. Thus, in the present case the summation in F only includes the Wyckoff $8f$ Fe sites. Finally, we work out the absolute square of the vector coefficient, $|\vec{\alpha}|^2 = (1+e_3^2)$. The resulting differential scattering cross-section writes:

$$\frac{d\sigma}{d\Omega} = \left(\frac{\gamma e^2}{4m_ec_0^2}\right)^2\left(\frac{\mu}{\mu_B}\right)^2(1+{e_3}^2)|f(\vec{\kappa})|^2\frac{(2\pi)^3N}{v_0}\sum_{\vec{\tau}}|F(\vec{\tau})|^2\delta(\vec{\kappa}\pm\vec{q}-\vec{\tau}) \tag{42}$$

The other structure considered, the amplitude modulated one with the moment along [1 0 0], is easily treated in the same way. We just write the moment as:

$$\vec{\mu}(\vec{r}) = \mu\hat{\mu}(\vec{r}) = \mu \begin{pmatrix} \cos(\vec{q}\cdot\vec{r}+\phi_0) \\ 0 \\ 0 \end{pmatrix} \Rightarrow \vec{\alpha} = \begin{pmatrix} 1-e_1^2 \\ -e_1e_2 \\ -e_1e_3 \end{pmatrix} \tag{43}$$

Since $|\vec{\alpha}|^2 = 1-e_1^2$, we reach the scattering cross-section of the amplitude modulated structure:

$$\frac{d\sigma}{d\Omega} = \left(\frac{\gamma e^2}{4m_e c_0^2}\right)^2 \left(\frac{\mu}{\mu_B}\right)^2 (1-e_1^2)|f(\vec{\kappa})|^2 \frac{(2\pi)^3 N}{v_0} \sum_{\vec{\tau}} |F(\vec{\tau})|^2 \delta(\vec{\kappa}\pm\vec{q}-\vec{\tau}) \tag{44}$$

When scanning along [1 $\overline{1}$ 0], the scattering cross-section (42) of the cycloidal structure is twice the cross-section (44) of the amplitude modulated structure. Furthermore, in the amplitude modulated case, the cross-section will depend on the angle in the basal plane between [1 0 0] and the momentum transfer. However, due to the symmetry related amplitude modulated domain with the moment along [0 1 0], this effect will not appear in a multi domain crystal. If we plug in the measured intensities of the satellites around (1 $\overline{1}$ 0) at 60 K and normalize with respect to the intensity of the nuclear reflection (1 $\overline{1}$ 0), we get the value 1.5 μ_B per Fe atom for the ordered moment in the cycloidal structure. In the amplitude modulated structure, we need a moment of 2.1 μ_B per Fe atom to get the observed intensities. In both cases we use the magnetic form factor of metallic Fe as tabulated in [19]. The moment 2.1 μ_B is very close indeed to the ordered moment of 2.2 μ_B in metallic Fe. In the magnetization measurements [8] it is concluded that the ordered Fe moment in $GdFe_4Al_8$ is reduced by a factor of 3 relative to metallic Fe. Therefore, the value of 1.5 μ_B from the cycloidal model appears more likely than the higher value from the longitudinal modulation. To distinguish more rigorously between the two structures, one must either apply polarization analysis to directly observe the rotation of spins or prepare a single magnetic domain to get a different geometrical factor in the cross sections. In Fig. 10, we note a pronounced difference in the intensity of the satellites with modulation vector parallel and perpendicular to the [1 $\overline{1}$ 0]-direction. There is no simple explanation to this effect in the models considered, but minor differences in the population of magnetic domains are often observed.

The ordering of Dy

At approximately 25 K, a steep increase in the satellite intensity in Fig. 10 indicates the ordering of the Dy-moments. The intensity has a maximum around 10 K. Since the (1 $\overline{1}$ 0) satellites are sensitive to the relative phase between the scattering from Fe and Dy, the maximum may indicate a reorientation of the moments. However, the maximum was not reproduced in *longitudinal* scans performed in later experiments at Risø. The ordering of Dy at low temperature is also observed by the appearance of satellites around reflections not sensitive to the Fe sites. In the Figs. 11, 12 and 13, we plot the intensity *vs.* temperature of the 1'st, 3'rd and 5'th order satellites appearing around (1 $\overline{2}$ 1), ($\overline{1}$ 0 $\overline{1}$) and (2 $\overline{2}$ 0), respectively. These Dy-only satellites are all very weak, and we should note that systematic errors especially related to the estimation of the background may be substantially larger than the errors estimated from the counting statistics. To analyze the intensities of the Dy-only satellites, we have calculated the product of the basal plane geometrical factor $(1+{e_3}^2)$ and the square of the Dy^{3+} form factor at all the relevant positions in reciprocal space. The results of these calculations are shown in Table 4.

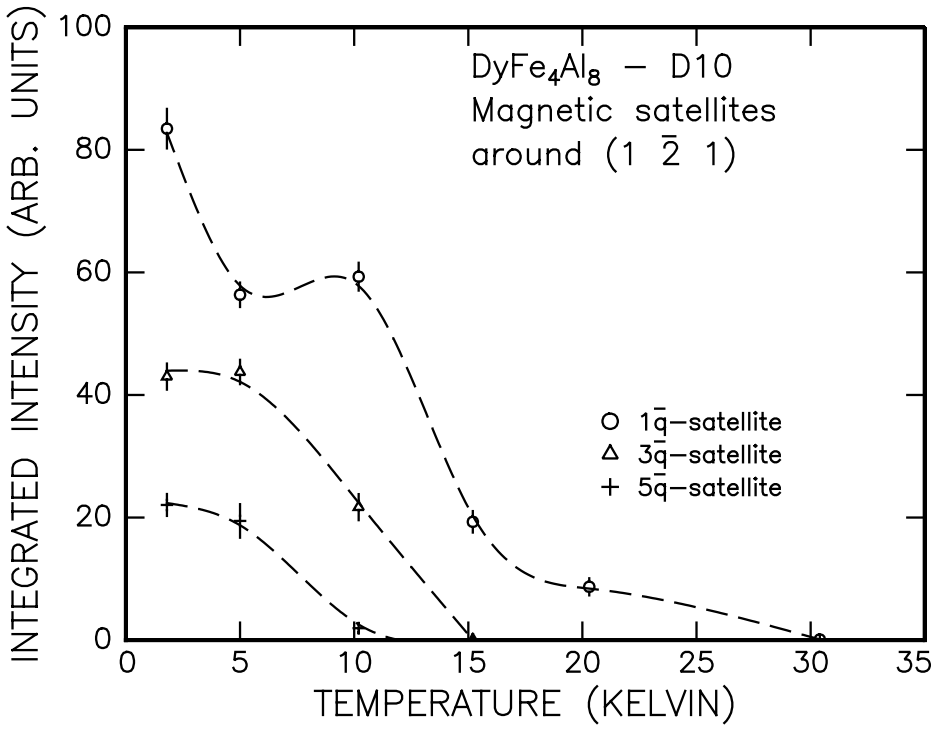

Figure 11. Integrated intensity of 1'st, 3'rd and 5'th order magnetic satellites around the $(1\ \overline{2}\ 1)$*-peak. The dashed curves are guides to the eye. Note, that since* 5ξ *is larger than* $\frac{1}{2}$*, the* $5\vec{q}$ *satellites appearing closest to* $(1\ \overline{2}\ 1)$ *are associated with the* $(0\ \overline{3}\ 1)$*- and* $(2\ \overline{1}\ 1)$*-reflections.*

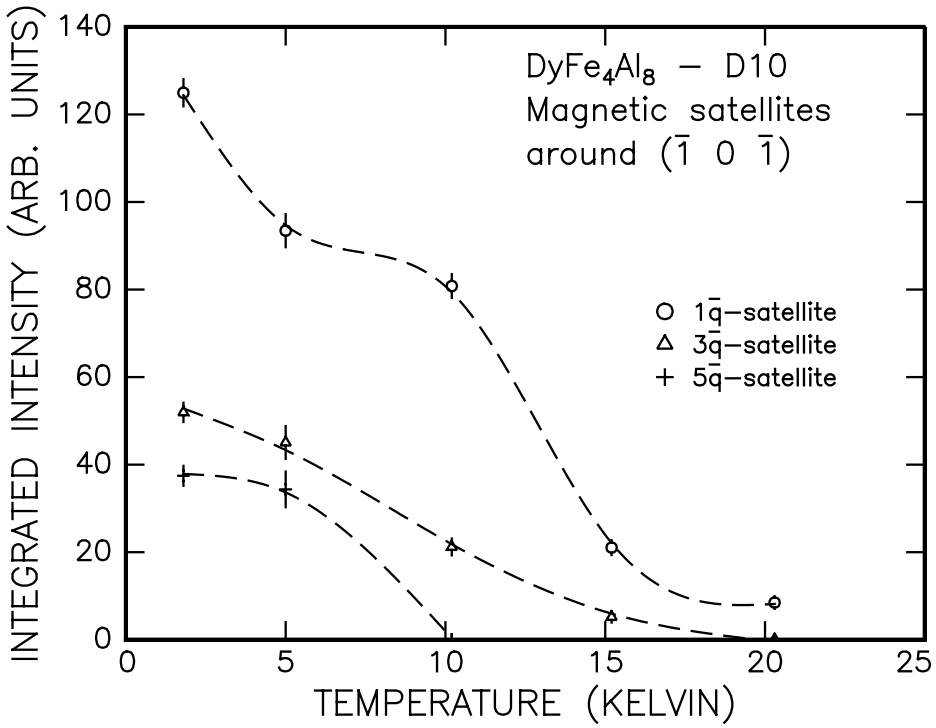

Figure 12. Integrated intensity of 1'st, 3'rd and 5'th order magnetic satellites around the $(\overline{1}\ 0\ \overline{1})$*-peak.The dashed curves are guides to the eye. Note, that the* $5\vec{q}$ *satellites appearing closest to* $(\overline{1}\ 0\ \overline{1})$ *are associated with the* $(\overline{2}\ 1\ \overline{1})$*- and* $(0\ \overline{1}\ \overline{1})$*-reflections.*

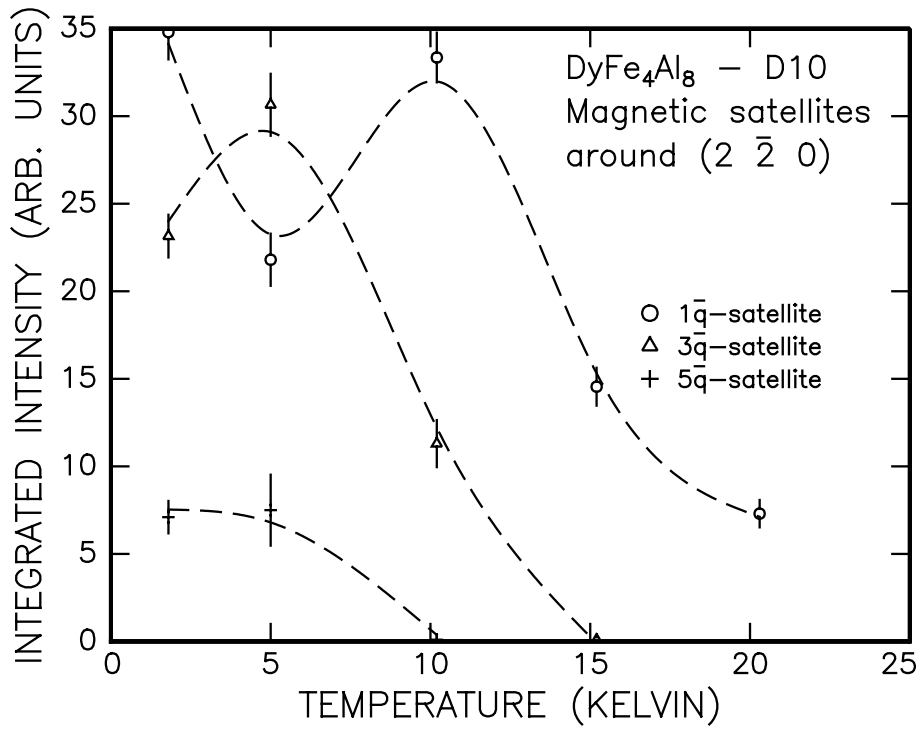

Figure 13. Integrated intensity of 1'st, 3'rd and 5'th order magnetic satellites around the $(2\ \overline{2}\ 0)$*-peak.The dashed curves are guides to the eye. Note, that the* $5\vec{q}$ *satellites appearing closest to* $(2\ \overline{2}\ 0)$ *are associated with the* $(1\ \overline{3}\ 0)$*- and* $(3\ \overline{1}\ 0)$*-reflections.*

Reflection	$+\xi$	$-\xi$	$+3\xi$	-3ξ	$+5\xi$	-5ξ
$(1\ \overline{1}\ 0)$	0.9268	0.9268	0.9171	0.9171	0.8980	0.8980
$(2\ \overline{2}\ 0)$	0.7461	0.7461	0.7386	0.7386	0.7240	0.7240
$(1\ \overline{2}\ 1)$	1.0450	1.0071	1.0639	0.9552	1.0612	0.8945
$(\overline{1}\ 0\ \overline{1})$	1.5614	1.4479	16245	1.3140	1.6150	1.1805

Table 4. The product of $(1 + {e_3}^2)$ *and the square of the* Dy^{3+} *form factor at the positions of magnetic satellites.*

To compare the measured intensities around different nuclear reflections, we divide the integrated intensity by the corresponding coefficient in Table 4. The resulting integrated intensities are listed in Table 5. We see, that the intensities observed around $(1\ \overline{2}\ 1)$ and $(\overline{1}\ 0\ \overline{1})$ are fairly consistent with the assumption of a basal plane cycloid. The consistency is not within the estimated errors in all cases, but considering the problems with correcting for the background and the low satellite intensities, we do not consider these discrepancies as sufficient reason to discard the cycloidal model. However, the intensities, especially in the 1'st order satellite, measured around the $(2\ \overline{2}\ 0)$ seems clearly off. In the plot of the $(2\ \overline{2}\ 0)$ satellite intensities *vs.* temperature it is also clear, that these reflections are somewhat odd. No explanations have been found to these problems with the $(2\ \overline{2}\ 0)$ satellites. The development of higher harmonics in the cycloidal structure is likely caused by the bunching of the spins along easy directions of the crystal field. Although the results for the configuration of the Dy spins are far from conclusive, it is interesting to evaluate the size of the ordered moment at the Dy-sites assuming the cycloidal model. Taking the intensities measured around the $(\overline{1}\ 0\ \overline{1})$ we get 6 μ_B. The same treatment of the satellites around the $(1\ \overline{2}\ 1)$ reflection gives an identical value. These results should be compared to the free-ion moment

of 10.6 μ_B. Later in this chapter of the thesis, we discuss observations of extinction release indicating, that the quoted ordered moment may be overestimated by around 5 percent. The ratios between the intensity of Dy-only satellites and the intensity of satellites around $(1\overline{1}0)$ are qualitatively consistent with a ferromagnetic coupling between the Fe- and Dy-sublattices. This is not in agreement with the general trend claimed by Buschow and van der Kraan [8].

Satellites around $(1\ \overline{1}\ 0)$

T(K)	-5ξ	-3ξ	$+3\xi$	$+5\xi$
1.8	17(1)	64(1)	70(1)	21(1)
5.2	12(2)	71(2)	70(2)	17(2)
10.2	7(1)	26(1)	31(1)	8(1)

Satellites around $(2\ \overline{2}\ 0)$

T(K)	-5ξ	-3ξ	$-\xi$	$+\xi$	$+3\xi$	$+5\xi$
1.8	9(1)	28(1)	47(2)	47(2)	35(1)	11(1)
5.2	14(2)	40(2)	31(2)	27(1)	44(2)	7(2)
10.2	6(2)	15(1)	44(2)	46(1)	16(1)	-
15.2	-	-	20(1)	19(1)	-	-
20.2	-	-	11(1)	9(1)	-	-

Satellites around $(1\ \overline{2}\ 1)$

T(K)	-5ξ	-3ξ	$-\xi$	$+\xi$	$+3\xi$	$+5\xi$
1.8	24(1)	41(2)	84(2)	79(3)	44(1)	22(2)
5.2	24(2)	38(1)	58(2)	52(1)	48(2)	16(2)
10.2	4(1)	20(2)	59(2)	57(2)	23(2)	-
15.2	-	-	19(1)	19(1)	-	-
20.2	-	-	8(1)	9(1)	-	-

Satellites around $(\overline{1}\ 0\ \overline{1})$

T(K)	-5ξ	-3ξ	$-\xi$	$+\xi$	$+3\xi$	$+5\xi$
1.8	29(1)	35(1)	83(2)	83(1)	36(1)	25(1)
5.2	30(3)	29(2)	65(2)	60(1)	32(2)	20(1)
10.2	-	17(1)	57(2)	53(1)	13(1)	-
15.2	-	4(1)	14(1)	15(1)	3(1)	-
20.2	-	-	6(1)	5(1)	-	-

Table 5. Integrated intensities of magnetic satellites divided by the respective geometrical factors and form factors listed in Table 4.

The integrated intensities of the higher order magnetic satellites appearing around the $(1\ \overline{1}\ 0)$ are shown in Fig. 14. By dividing these intensities by the appropriate factors of Table 4 and comparing with the intensities of the Dy-only satellites, we may determine whether the Fe sublattice takes part in the formation of higher order satellites. In Table 5 we also list the corrected intensities of the $(1\ \overline{1}\ 0)$ higher order satellites. It is clear, that the intensities of the $3\vec{q}$ satellites are approximately a factor of two higher than the corresponding Dy-only intensities at the $(\overline{1}\ 0\ \overline{1})$ listed in Table 5, and we conclude, that the magnetic

structure of the Fe sublattice is distorted. Since the $5\vec{q}$ satellites around (1 $\overline{1}$ 0) are associated with (0 $\overline{2}$ 0) and (2 0 0), these satellites are not sensitive to the Fe ordering. A set of $5\vec{q}$ satellites probing the Fe sites appears around (2 $\overline{2}$ 0), but as described above, we retain from drawing conclusions from this part of the data set.

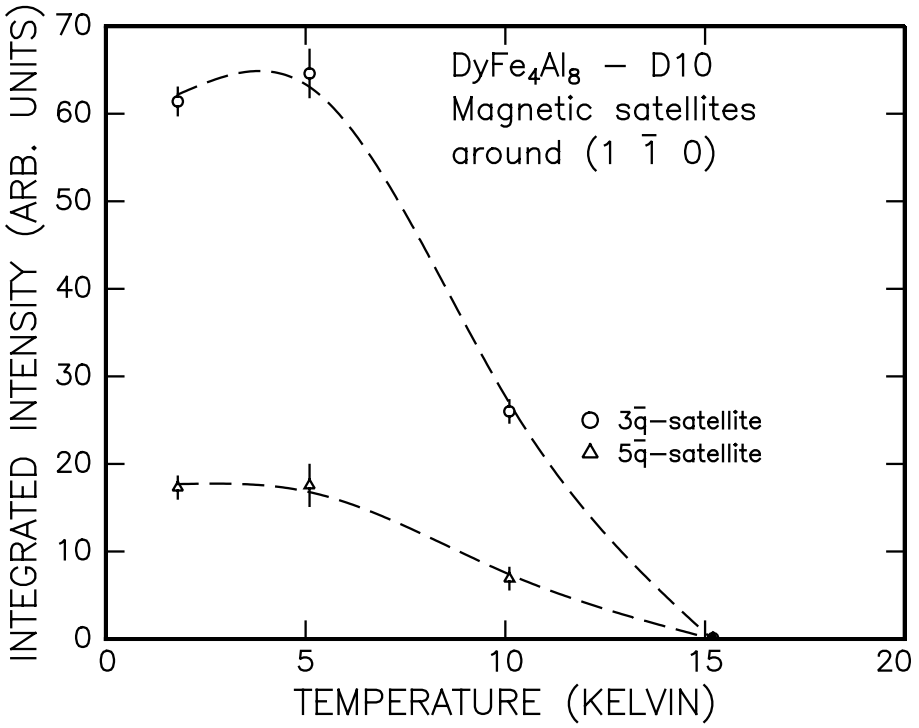

Figure 14. Integrated intensity of the 3'rd and 5'th order magnetic satellites around the (1 $\overline{1}$ 0)*-peak. The dashed curves are guides to the eye. Note, that the* $5\vec{q}$ *satellites appearing closest to* (1 $\overline{1}$ 0) *are associated with the* (0 $\overline{2}$ 0)*- and* (2 0 0)*-reflections.*

Several times we have mentioned the problem of estimating the background due to diffuse scattering building up at low temperature. The diffuse components are seemingly centered around the nuclear peaks corresponding to a short range ferromagnetic correlation.

6.3 Summary of the D10 experiment

We briefly summarize the D10 experiment in the following points:

- The ordering of Fe in a basal plane cycloidal structure is observed from approximately 180 K.
- The ordering of Dy is observed below approximately 25 K. The observed intensities are fairly consistent with a basal plane cycloidal structure.
- The magnetic structure is modulated along the <1 1 0> directions, and the modulation vector locks in at low temperature to the value of ($\frac{2}{15}$ $\frac{2}{15}$ 0).
- From the selection rules of the crystal structure, it is concluded, that on the Fe sublattice the moments rotate 180° + 24° when going from one Fe plane normal to <1 1 0> to the next.
- At temperatures below 15 K, 3'rd and 5'th order satellites are observed. These may be due to the bunching of moments around easy axes of the crystal field.
- For the ordered moment at the Fe sublattice we find the value of 1.5 μ_B at 60 K when assuming a basal plane cycloidal structure.

- Assuming the basal plane cycloid for the Dy as well, we get the value 6 μ_B for the ordered Dy moment at 1.8 K. We note, that due to release of extinction at low temperature, this value may be overestimated by some 5%.
- The observed satellite intensities are qualitatively consistent with a ferromagnetic coupling between the Fe- and Dy-sublattices.
- At low temperatures, a significant component of diffuse scattering is observed around the nuclear reflections.

7 An X-ray resonant magnetic scattering experiment

The possibility of scattering of X-rays from magnetic moments was realized already in 1929 in a work by Klein and Nishina (see [38] and references herein). However, the cross-section for this scattering was found to be reduced relative to the cross-section of Thompson charge scattering by a factor of the order $\frac{\hbar\omega}{m_e c_0^2}$, $\hbar\omega$ being the X-ray energy and $m_e c_0^2$ the electron rest mass. At X-ray energies typically used for diffraction in solids, the reduction of scattered intensity is of the order 10^4. In spite of it's weakness, magnetic scattering from antiferromagnetic NiO was observed by de Bergevin and Brunel [11] using a standard Cu sealed tube X-ray source. At the magnetic peak, the intensity was approximately 2 counts per minute on top of an eight times higher background, and the counting times were several days. With the advent of tunable, high intensity X-ray sources at synchrotron facilities, X-ray magnetic scattering has developed from a subject of fundamental theories and delicate demonstration experiments into a powerful tool of solid state physics. The effect discovered by Klein and Nishina and demonstrated by de Bergevin and Brunel is today known as non-resonant X-ray magnetic scattering. In 1985 Namikawa discovered a resonant enhancement of the magnetic scattering in Ni when the incident energy was close to the K-shell absorption edge. A similar, but much stronger enhancement has been observed at the L-edges of the rare earth elements and at the M-edges of the actinides. Since this X-ray *resonant* magnetic scattering (XRMS) involves the tuning of the incident energy to an absorption edge, the technique is element specific. Thus XRMS is an obvious choice of technique for the investigation of systems like $DyFe_4Al_8$ containing several magnetic species.

After a short introduction to the technique of XRMS, this section shall report on an XRMS experiment on $DyFe_4Al_8$ performed at the magnetic scattering beamline ID20 of the ESRF in collaboration with J. A. Paixão, University of Coimbra, Portugal, S. Langridge, ISIS, UK, G. H. Lander, EITU, Karlsruhe Germany and C. Vettier, N. R. Bernhoeft, A. Stunault and D. Wermeille from the ID20 group of the ESRF, Grenoble, France.

7.1 Principles of XRMS

Quite analogous to the formulation of neutron scattering, we may introduce a scattering length to characterize the scattering of X-rays from an atom. This scattering length takes the generic form:

$$f = f_0 + f'(\omega) + \imath f''(\omega) \tag{45}$$

In this expression, f_0 represents the energy independent high energy limit, where the electrons of the atom are considered unbound, since the photon energy, $\hbar\omega$ is much larger than the electron binding energies. When the X-ray energy approaches the transition energy from a core state to an empty state above the Fermi level of the atom, a strongly energy dependent term shows up in the scattering length. Electrons are driven by the X-ray field back and forth between the core state and the empty state. Since the upper state may decay spontaneously, energy is dissipating from the X-ray field leading to both a real part $f'(\omega)$ and an imaginary part $f''(\omega)$ in the scattering length. As a simple but highly useful classical picture, one may think of the atom in the X-ray field as a driven, dampened harmonic oscillator. As a first approximation, we may calculate the scattering length needed to describe the diffraction of X-rays from a solid in the model of an isolated atom, and apply well established formalism from atomic physics and quantum optics. Hence, the scattering length is extracted from time-dependent perturbation theory, and we must consider the matrix elements of the interaction of electrons with the X-ray field. The operator describing the interaction between the field and the electrons will depend on the position of the electrons. In the calculation of the matrix elements, we overcome this problem by expanding the spatial dependence of the interaction in powers of the position. The individual terms of this multipole expansion are named dipole, quadrupole, octopole and so forth. If we take the electric part of the dipole term, usually designated $E1$, the resonant part of the scattering takes the form:

$$\begin{aligned} f_r^{E1} &= -\frac{3}{4\pi q}\left\{(\vec{\epsilon}\,'\cdot\vec{\epsilon})\left[F_{+1}^1+F_{-1}^1\right]\right. \\ &\quad +\imath(\vec{\epsilon}\,'\times\vec{\epsilon})\cdot\hat{m}\left[F_{-1}^1-F_{+1}^1\right] \\ &\quad \left.+\,(\vec{\epsilon}\,'\cdot\hat{m})(\vec{\epsilon}\cdot\hat{m})\left[2F_0^1-F_{+1}^1-F_{-1}^1\right]\right\} \end{aligned} \tag{46}$$

The definitions of the symbols appearing in this equation are shown in Fig. 15; $\vec{\epsilon}$ and $\vec{\epsilon}\,'$ are the polarization vectors of the incident and the scattered electric field, $q=\omega/c$ is the X-ray wave number and $\hat{m}$ is a unit vector parallel to the magnetic moment of the atom. Finally, F_ν^1 are energy dependent resonant strengths for the $E1$ transition (the superscript 1 refers to the change of one in the angular momentum quantum number, l) corresponding to a change of ν in the magnetic quantum number.

The first term of the scattering length in equation (46) represents the "usual" anomalous dispersion, i.e. the resonant part of the scattering length, which does not depend on the magnetization. Note, that the polarization dependence of this term, $\vec{\epsilon}\,'\cdot\vec{\epsilon}$ is identical to the polarization dependence of the non-resonant Thompson charge scattering. The X-rays from conventional synchrotron sources (bending magnets, symmetric wigglers and undulators) are to a very high degree (typical from 95% to close to 100%) linearly polarized in the plane of the synchrotron ring. This polarization, we shall denote σ-polarization, whereas the photon state with polarization vector perpendicular to the ring plane is denoted π-polarization. From the polarization dependence of both the Thompson scattering and the first term of equation (46), it is clear that neither of these types of scattering may produce π-polarized light from incident σ-polarization. The second term of the scattering length depends linearly on the direction of the local magnetic moment. In a modulated structure with the modulation vector $\vec{q}$, this term gives rise to satellites displaced by $\vec{q}$ from the charge Bragg peaks. Furthermore, the term is proportional to the cross product of the polarization vectors of the incident and scattered beams. Hence, this second term rotates the incident σ-polarization into the π-channel. The intensity of the resonant scattering is determined by the matrix elements F_ν^1. The group of D. Gibbs at Brookhaven National Laboratory, U.

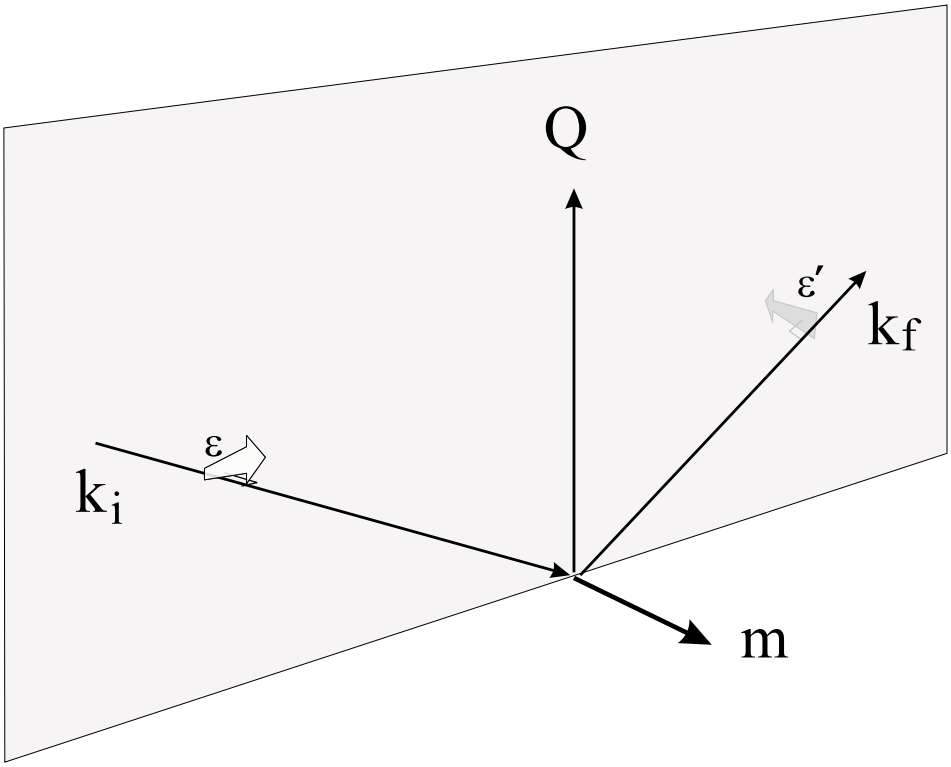

Figure 15. Scattering geometry assumed in the scattering length stated in equation (46). $\vec{k}$ and $\vec{k}'$ are the incident and scattered wave vectors, $\vec{\epsilon}$ and $\vec{\epsilon}'$ the polarization vectors of the incident and scattered beams and $\hat{m}$ is a unit vector parallel to the magnetization.

S. undertook in the last part of the 1980's a detailed investigation of the magnetic properties of Ho by X-rays [16]. In this experiment, a 50 fold resonance enhancement of the scattered intensity at the $1\vec{q}$-position was found. In the third term of the scattering length, the local magnetization appears to 2'nd order. Thus, in a modulated structure this term gives rise to magnetic satellites displaced by twice the modulation vector even in the case of a plain sinusoidal structure. Again, referring to the experiment on Ho by Gibbs and coworkers [16], they found the intensity of these satellites reduced by a factor of 20 compared to the $1\vec{q}$ satellites from the second term. It is also worth noting, that in Ho weak $3\vec{q}$- and $4\vec{q}$ satellites were observed. To account for those satellites one has to include the $E2$ quadrupole transition in the scattering cross section. When comparing to atomic transitions driven by visible light, the $E2$ term becomes important in our case because it contains the gradient of the field, and the wavelength of the radiation is comparable to the extent of the wave functions. As briefly mentioned above, the useful resonance enhancement in rare earth systems is found at the L-edges. Since the dipole interaction imposes the selection rule $\Delta l = \pm 1$ on the angular momentum quantum number, it is clear that the dipole resonances at the L_{II} and L_{III} edges involve the transitions $2p_{1/2} \rightarrow 5d_{3/2}$ and $2p_{3/2} \rightarrow 5d_{5/2}$ respectively. Hence, the $E1$ resonant scattering does not involve the $4f$-electrons of the rare earth ions directly. In the $E1$ part of the scattering, the magnetism of the $4f$-system is probed through it's polarization of the $5d$-electrons. However, since the $E2$-interaction has the selection rule $\Delta l = \pm 2$, this weak part of the scattering is probing the $4f$-moment directly.

With the high intensity of radiation from synchrotron sources, even the weak non-resonant magnetic scattering may become a useful probe. A very attractive

feature of the non-resonant scattering cross-section is different polarization factors for the orbital and spin parts of the total angular momentum. In principle, one could separate the two contributions by a direct measurement using non-resonant magnetic scattering.

To summarize, we list a number of appealing features of the magnetic X-ray techniques:

- With the modern synchrotron sources, the typical momentum transfer resolution in an X-ray magnetic scattering experiment is of the order 10^{-4} Å^{-1}.
- The resonant technique is element specific. That is highly useful in the study of alloys and compounds with several magnetic elements.
- The scattering cross-section has polarization dependencies that are useful in the practical experiment. In the dipole part of the resonant cross section, the dominant $1\vec{q}$-term rotates the plane of polarization by 90°. Polarization analysis effectively reduces the charge scattering background and plays a crucial role when deciding whether a peak is charge or magnetic scattering.
- With the non-resonant technique, we have, in principle, direct access to the orbital and spin parts of the total angular momentum.
- Since the geometrical prefactors of the X-ray and neutron scattering cross-sections are different, the combination of the two techniques may be useful in solving magnetic structures.

One often hears discussion of whether X-rays or neutrons should be regarded *the* universal microscopic probe of magnetism. The X-ray techniques are undergoing a very rapid development, but at least at the present time, the question of a single universal probe seems to have little meaning. Compared to neutron measurements, the X-ray experiments are generally more technically complicated. The use of resonant techniques rely on the existence of absorption edges at wavelengths applicable for diffraction. In the case of X-ray resonant magnetic scattering, the intensity of the diffraction peaks involves atomic matrix elements, which may be difficult to determine. Presently, the problem of relating the intensity of resonant magnetic diffraction peaks to the size of the ordered magnetic moment remains unsolved. The so-called branching ratio problem, a variation of the ratio between the resonant enhancement at the L_{II} and the L_{III} edges through the rare earth series, indicates the complexity of the theoretical treatment of diffraction peak intensities. Furthermore, it is important to note, that though the spin and orbital parts of the angular momentum are not directly accessible to neutron techniques, the two components can be separated in an indirect way by the fitting of neutron data to a form factor based on a model involving $\vec{L}$ and $\vec{S}$.

7.2 Experimental details

The ID20 beamline of the ESRF [13] is an instrument dedicated to X-ray studies of magnetism. In order to provide both linear and circular polarization of the incident beam in a broad energy range (3 keV - 40 keV), the experimentalist has the choice between an undulator and an asymmetric wiggler as the source of radiation. In combination with diamond crystal phase plates, the undulator provides X-rays with linear or circular polarization in the photon energy range up to 20 keV. At higher energies, the phase plates are no longer efficient in changing the polarization state, and the asymmetric wiggler source is used. To suppress higher order contamination of the beam and to focus the beam, mirrors are installed at either side of the double crystal Si monochromator. The curvatures of the mirrors are

automatically controlled to obtain a parallel beam in front of the monochromator and focusing of the beam at the sample position. The brilliance, i.e. the number of photons per second per square radian per square millimeter, in a bandpass of 0.1% at 8 keV photon energy is 10^{19} $s^{-1}mrad^{-2}mm^{-2}$. At 8 keV, the energy resolution of the beamline is 1.6eV. Down stream to the front end optics, a flexible diffractometer is installed. This instrument gives the choice between horizontal and vertical scattering geometry. In the vertical geometry and incident σ-polarization, the charge scattering polarization factor $\vec{\epsilon}' \cdot \vec{\epsilon}$ is independent of the scattering angle. However, the possibility to mount heavy sample environments and cryostats using liquid coolants is limited in this geometry. Therefore, the access to horizontal geometry is crucial when using such equipment. At the exit side, the diffractometer has a housing for an analyzer crystal. This option is used to provide high momentum transfer resolution or to analyze the linear polarization state of the scattered beam. The latter function is obtained by selecting an analyzer crystal with a d-spacing corresponding to 90° Bragg scattering of the incident photon energy. If the scattered photons are σ-polarized, the product $\vec{\epsilon}' \cdot \vec{\epsilon}$ will be zero if the polarizer is set to scatter the beam by 90° out of the vertical plane. Conversely, if the scattered photons are π-polarized, the scattering at the polarizer cancels in the vertical plane. This principle of linear polarization analysis is illustrated in Fig. 16.

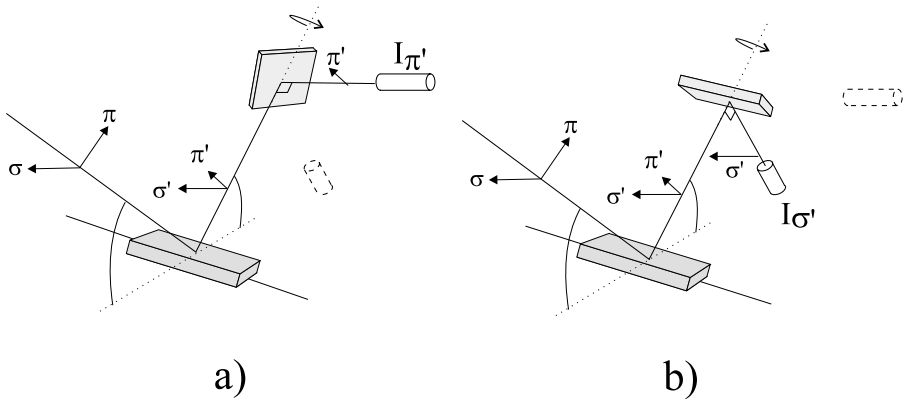

Figure 16. The principle of the linear polarization analysis used in the XRMS experiment. After the incident beam has been scattered from the lower sample crystal, it is diffracted on the upper analyzer crystal. When the analyzer scatters by 90° *in the plane containing the σ-polarization vector (a), only the π-polarized part of the beam is detected. In (b), the* 90° *scattering on the analyzer is in the plane containing the π-polarization, and only the σ-polarized part of the beam is detected.*

In the present experiment, only σ-polarized incident radiation with photon energy around 8 keV was used, and the undulator source was applied. The diffractometer was operated in the vertical scattering geometry with the sample mounted in a two stage closed cycle helium refrigerator going down to 12 K. The cryostat was equipped with a Be vacuum shroud, and inside this, the sample was mounted in a small Be can filled with He exchange gas. Throughout the experiment, polarization analysis was applied using the (0 0 6)-reflection of a graphite analyzer crystal. To obtain good reflectivity, the sample was prepared by polishing a 1 mm^2 surface normal to the [1 1 0]-direction.

7.3 Results

The resonant enhancement at the Dy L_{III}-edge of the magnetic scattering is seen in Fig. 17, where the peak intensity of the $(4-\xi\ 4-\xi\ 0)$ magnetic satellites is measured as a function of energy. The measurement is performed by scanning the incident energy while keeping the momentum transfer fixed at the peak position. Note, that the peak shape is asymmetric This is due to the interference between the dominant $E1$ contribution and the much weaker resonant $E2$ and non-resonant contribution. The asymmetry comes about since the energy of the $E1$ and the $E2$ resonances are slightly different and because the relative phases of the resonant and non-resonant parts of the scattering length changes when passing the resonance.

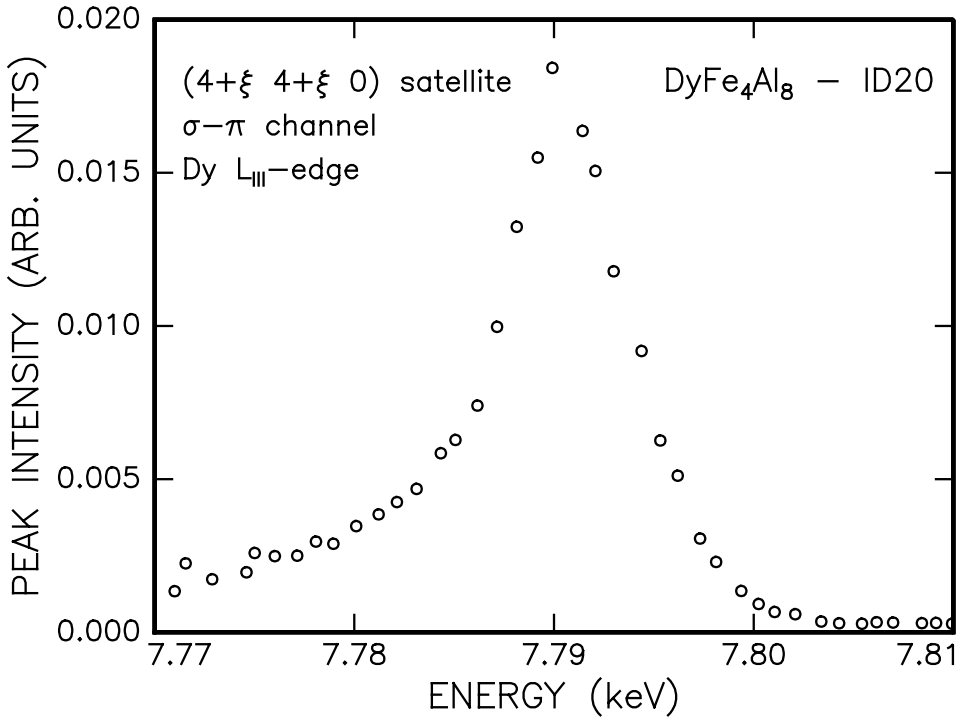

Figure 17. The intensity of the $(4+\xi\ 4+\xi\ 0)$ *magnetic satellite as a function of energy when scanning through the* Dy L_{III}*-edge.*

To obtain new information on the magnetic structure of $DyFe_4Al_8$, the intensity of the 1'st order magnetic satellites along the [1 1 0] direction was measured at the base temperature of the cryostat (12 K) in two different orientations of the crystal. As shown in Fig. 18, when in the orientation a, the sample has it's *bct* basal plane parallel to the vertical scattering plane. When going to orientation b, the sample is rotated by 90° around the scattering vector bringing the basal plane of the crystal structure perpendicular to the scattering plane. In Fig. 19, we show the Lorentz corrected integrated satellite intensity measured in the two sample orientations as a function of scattering angle.

The Lorentz corrected satellite intensity with the sample in orientation a is clearly independent of the scattering angle. From the expression (46) and the Figs. 15 and 18 we see, that the satellite intensity is proportional to $(\vec{k}\cdot\hat{m})^2$ averaged over a period of the magnetic structure. Assuming that the magnetic moments are in the basal plane, we may explain the rotational symmetry of the satellite intensity by either the cycloidal structure or two symmetry related domains of an amplitude modulated structure with moments along the <1 0 0>-directions. The latter possibility seems unlikely with a cycloidal structure on the Fe sub-

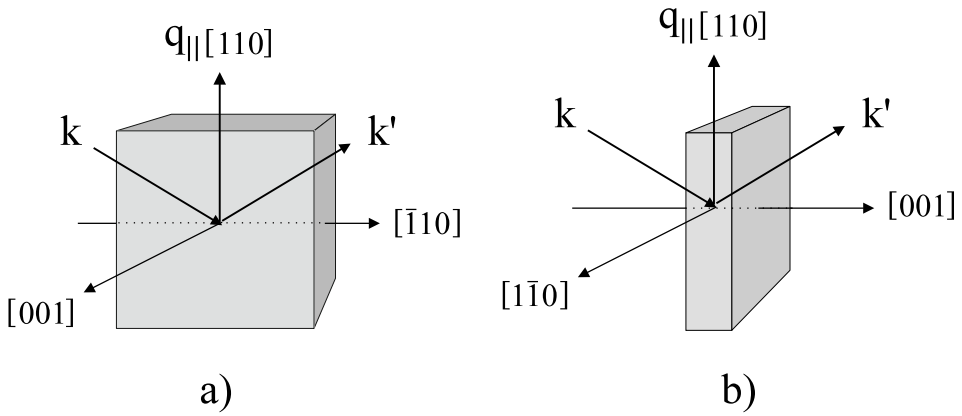

Figure 18. The two sample orientations used in the XRMS experiment. In orientation a, the basal plane of the sample is parallel to the scattering plane. In orientation b, the sample has been rotated around [1 1 0] *to bring the basal plane perpendicular to the scattering plane.*

lattice. We now turn to the satellite intensities measured in orientation b. If the moment is distributed with rotational symmetry in the basal plane, the average of the product $(\vec{k} \cdot \hat{m})^2$ becomes proportional to $\sin^2(\theta)$. The full curve through the points of orientation b is a $\sin^2(\theta)$. The average intensity observed in orientation a has been normalized to unity, and the prefactor of the full curve in orientation b has been calculated from the expression of the scattering length assuming the cycloidal structure. Thus, the XRMS experiments brings strong support to the picture of the magnetic structure based on the D10 experiment. However, since the available cryostat had the base temperature of 12 K no further understanding of the formation of higher order satellites was obtained.

In the XRMS experiment, the position and intensity of the $(3-\xi\ 3-\xi\ 0)$ and $(4-\xi\ 4-\xi\ 0)$ satellites were monitored as a function of temperature. The temperature dependence of the two satellites is completely identical. Since the satellite associated with (3 3 0) is sensitive to both Fe and Dy, but the one associated with (4 4 0) is a Dy-only peak, this identical behavior clearly shows the element specific character of XRMS: In both cases we observe Dy, since this is the element, that we tuned to. In spite of the specific sensitivity to the Dy, some residual intensity stays in the two satellites above the ordering temperature of Dy and all the way up to the disordering of Fe. Since the dipole L_{III}-resonance involves transitions $2p_{3/2} \rightarrow 5d_{5/2}$, the residual signal is the polarization of the $5d$-electrons of Dy caused by the Fe. Thus, the XRMS directly probes the overlap between Dy-$5d$ and Fe-$3d$ wave functions. The observed behavior of $\vec{q}$ *vs.* temperature is clearly different from the one observed with neutrons in the D10 experiment. In the X-ray case, the modulation vector shows a lock-in already around 100 K whereas a lock-in did not appear until the ordering of Dy in the D10 experiment. There is an obvious difference between the two experiments, since the neutrons interact with the Fe directly whereas the resonant X-ray signal only probes the Fe indirectly through the polarization of Dy. Moreover, in the neutron experiments, the bulk of the sample is probed but the X-rays are sensitive to the surface only. From the structure refinement it follows that the $1/e$ penetration depth of 14 meV neutrons in $DyFe_4Al_8$ is 0.8 cm. At photon energies in the vicinity of the Dy L-edges, the X-rays penetrate a few microns into the surface of the sample. However, it is not clear how these differences could result in the observations of different periods in

the structure.

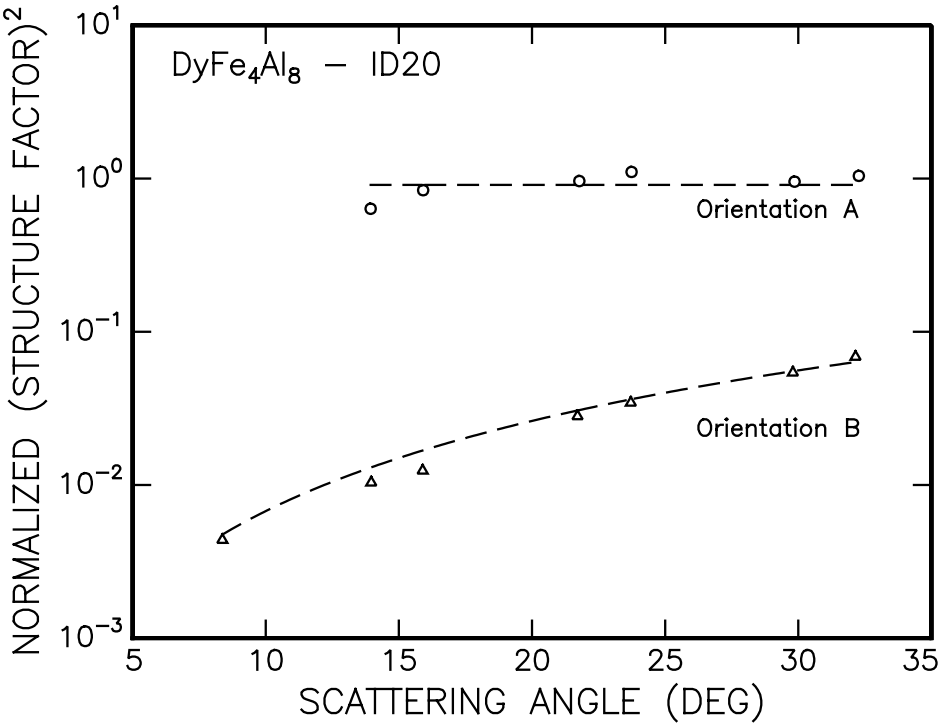

Figure 19. The Lorentz corrected intensity of the 1'st order magnetic satellites around (h h 0)-reflections as a function of the scattering angle. The two orientations are defined i Fig. 18.

In addition to the results presented here, the XRMS work on $DyFe_4Al_8$ has included spectroscopic aspects. A full report on the experiment will be found in [33].

8 Neutron scattering from $DyFe_4Al_8$ in applied magnetic field

In two experiments conducted at spectrometers at the DR3 reactor of Risø National Laboratory, the magnetic structure of $DyFe_4Al_8$ was studied in applied magnetic field. The main picture is a very high susceptibility of the Dy-moments to the applied field, whereas the moments of the Fe sites stay in a modulated structure even in a field of 5 T. In the experiments at Risø, we also observed effects of release of extinction due to the interaction between the magnetic and the crystalline structure.

8.1 Experimental details

Due to the scheduling of beam time, the field measurements were undertaken in two parts at different instruments, TAS1 and TAS3, using different sample environments.

The first experiment was conducted at the multi purpose diffractometer TAS3. This instrument is installed at the thermal source of the DR3 reactor. It has a range

of detector units making the instrument applicable to both single crystal diffraction, powder diffraction and highly specialized characterization measurements on textured samples. For the present experiment, the instrument was equipped with a tilting detector and used in the standard double axis configuration, i.e. the detector was in the horizontal plane throughout the experiment, and the sample orientation was only changed by rotation around a vertical axis. The neutrons from the thermal water source are monochromatized by a graphite monochromator. The sample is mounted on a turn-table with two motorized goniometer arcs for the alignment. Both the in-pile collimation and the collimation in front and behind the sample may be changed by the user. In the in-pile case by translating a motorized bank of Soller collimators, and in the two other beam paths by inserting units with fixed collimation Soller systems. In the present experiment no collimator was used in-pile or in the monochromator to sample path giving a beam divergence of approximately 1 degree. A 60' Soller unit was placed in front of the detector to limit the background. For the experiment we used 2.36 Å incident neutrons. Since at this wavelength, the beam from the thermal neutron source will be heavily contaminated by $\lambda/2$-neutrons, a graphite filter was used. With the choice of instrumental parameters stated above, a longitudinal momentum transfer resolution of the order 5×10^{-2} Å^{-1} at the (2 2 0) position was achieved. The sample was mounted with the [1 $\overline{1}$ 0]-direction along the vertical field of a 9 T cryomagnet. In this sample environment, the cooling of the sample and the cooling of the super-conducting magnet coils has been separated by mounting the sample in a chamber inside a so-called "variable temperature insert". This insert is thermally insulated from the He-bath by a vacuum, but by pumping He into the insert through a needle-valve connection to the bath, the insert and the sample may be cooled down to 1.5 K. When closing the needle valve, the insulation between the bath and the insert makes it possible to heat the sample to room temperature while keeping the magnet coils super-conducting. The background scattering from the cryomagnet is moderate, but only about 50% of the incident 2.36 Å neutrons are transmitted through the device.

The triple axis spectrometer TAS1 was used in the second part of the experiment. This machine is installed at the cold hydrogen source of DR3. As in the TAS3 experiment, a monochromator of pyrolythic graphite (PG) is used for the monochromatization of the incident beam. The in-pile collimation is fixed at 60', the collimation between monochromator and sample is defined by Soller plug-in units. The sample rotation around the vertical axis is motorized, but the goniometer arcs of the turntable must be adjusted by hand when the sample is aligned. Behind the sample, the energy of the scattered neutrons is analyzed by another PG crystal. At either side of the analyzer, the collimation is defined by movable cadmium plates. Unlike the "true" triple axis setup, the incident neutron energy is semi fixed, since the user has the choice between four fixed take-off angles at the monochromator. Changing the incident energy means moving (by tools) the whole instrument from one hole in the monochromator shielding to another. However, the detected energy is continuously variable. The analyzer is shielded by a set of pneumatically operated wedges. After the wedges have been lifted by compressed air, the detector can be moved by a motor to change the analyzer take-off angle. The orientation of the sample with the [1 $\overline{1}$ 0]-direction along the vertical field was kept from the TAS3 experiment, but this time a less sophisticated 5 T cryomagnet was used. The sample is mounted in an insert in direct thermal contact with the He-bath. With this construction, keeping the sample at a temperature different from 4.2 K was complicated and highly He consuming. In the TAS1 experiment, the incident neutron wavelength was 4 Å. To remove the substantial 2'nd order contamination of the beam, a filter of nitrogen cooled Be powder was

inserted in the incident beam path. The monochromator to sample and the sample to analyzer collimations were each 60', while the collimation between analyzer and detector was 120'. With this choice of wavelength and collimations, the longitudinal momentum transfer resolution at the (2 2 0) position was of the order 2×10^{-2} Å^{-1}. When compared to the 9 T magnet, the background scattering from the 5 T magnet is low, and the neutron transmission is high.

8.2 Results in applied field

In the first part of the experiment at the TAS3 instrument, the focus was on the low field region up to 1 T. At fixed magnetic field, the diffraction pattern was recorded in scans along the [1 1 0]-direction at temperatures between 2 K and 24 K. In Fig. 20, we show the results obtained at 2 K in fields of 0 T, 0.125 T and 0.75 T. In the plots, a reference scan measured at 180 K and 0 T has been subtracted from the raw data.

In the scans of Fig. 20, a number of interesting features are observed. Firstly, the intensity of the (1 1 0)-peak increases dramatically when the field is applied. As discussed earlier in this chapter, the (1 1 0)-peak is sensitive to a ferromagnetic alignment at the Dy-sites, while such an alignment at the Fe sites will not affect the (1 1 0)-reflection. Conversely, the (2 2 0)-reflection is sensitive to both Fe and Dy sites. However, the intensity of this peak seems to decrease when the field is applied. Such a behavior could only be ascribed to magnetism in case of an opposite direction of ferromagnetic alignment at the two sites. However, this situation is clearly odd, and later in this section an explanation of the decreasing intensity at (2 2 0) in terms of extinction is discussed. The additional scattering at the nuclear positions observed in zero field is also ascribed to extinction effects. Secondly, the intensity of the 1'st order magnetic satellites increases when the field of 0.125 T is applied. This is quite reasonable, since the field is applied perpendicular to the direction of momentum transfer. The cycloidal structure is perturbed by the field, probably to a fan-like structure, and a larger portion of the ordered moment contributes to the magnetic scattering length. At the field of 0.75 T, the Dy-only satellites around the (2 2 0)-reflection are gone while some intensity from the Fe remains around the (1 1 0). Thirdly, the diffuse scattering observed in the D10 experiment is quite clearly seen at 0 T and 0.125 T. However, the diffuse component is suppressed by the 0.75 T field. Furthermore, in the field of 0.125 T, 2'nd order magnetic satellites are seen. The appearance of such satellites is consistent with the formation of a modulated structure with a net moment. Finally, when comparing to the D10 experiment, the 3'rd order magnetic satellites are barely detectable at zero field. Compared to the D10, the background is significantly higher and the transmission through the sample environment significantly lower in the present TAS3 setup. At the positions of the 5'th order satellites rather strong peaks are observed. These positions are one third of allowed nuclear reflections, and a significant fraction of the intensity is ascribed to nuclear scattering of 3'rd order neutrons in the TAS3 incident beam leaking through the graphite filter.

The field range 1.4 T to 5 T was covered in the second part of the experiment. Due to the limitations of the cryomagnet, all measurements in this part were carried out at a fixed temperature of 4.2 K. In Fig. 21, we show the intensity of the two reflections (1 1 0) and (2 2 0) and their 1'st order magnetic satellites at 4.2 K as a function of applied field. At low fields, we note the steep increase of the 1'st order magnetic satellites and the following decrease to an approximately constant intensity level from 0.75 T. From this field value, the Dy-only satellites of the (2 2 0) are no longer observed, and the satellites of the (1 1 0) level off at an intensity comparable to that measured at zero field above the ordering of

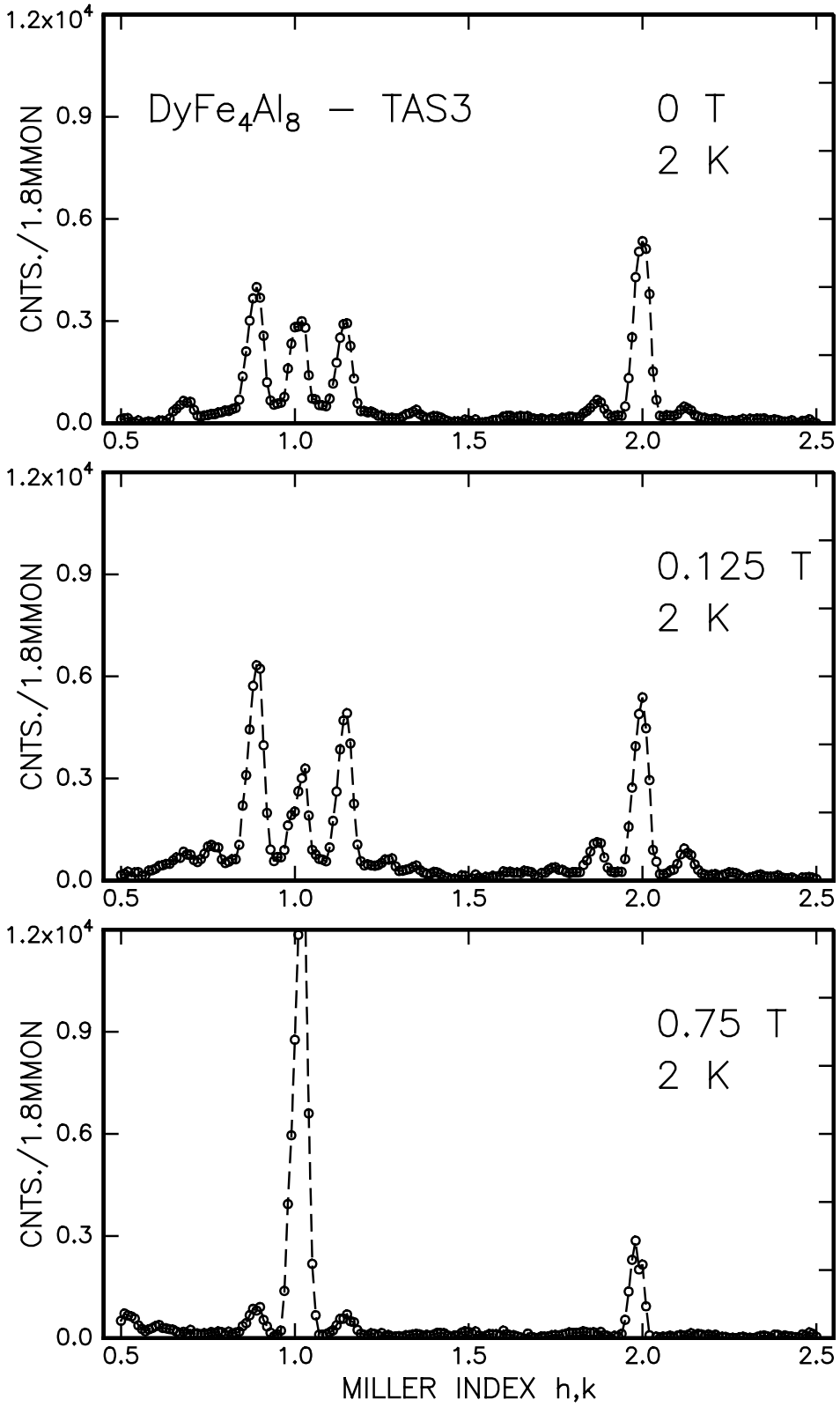

Figure 20. Background subtracted scans along the [1 1 0]*-direction measured in a field of 0 T (upper panel), 0.125 T (the middle panel) and 0.75 T (lower panel). The three scans were performed at 2 K and the subtracted background was recorded at 0 T and 180 K. The dashed curves are guides to the eye.*

Dy. We thus reach the general picture, that in the field region 0.75 T to 5 T, the modulation of the Dy is quenched, but the structure of Fe is fairly unperturbed by the field. The alignment of the Dy-moments along the field direction is indicated by the increase of the intensity of the (1 1 0)-reflection. The 2'nd order magnetic

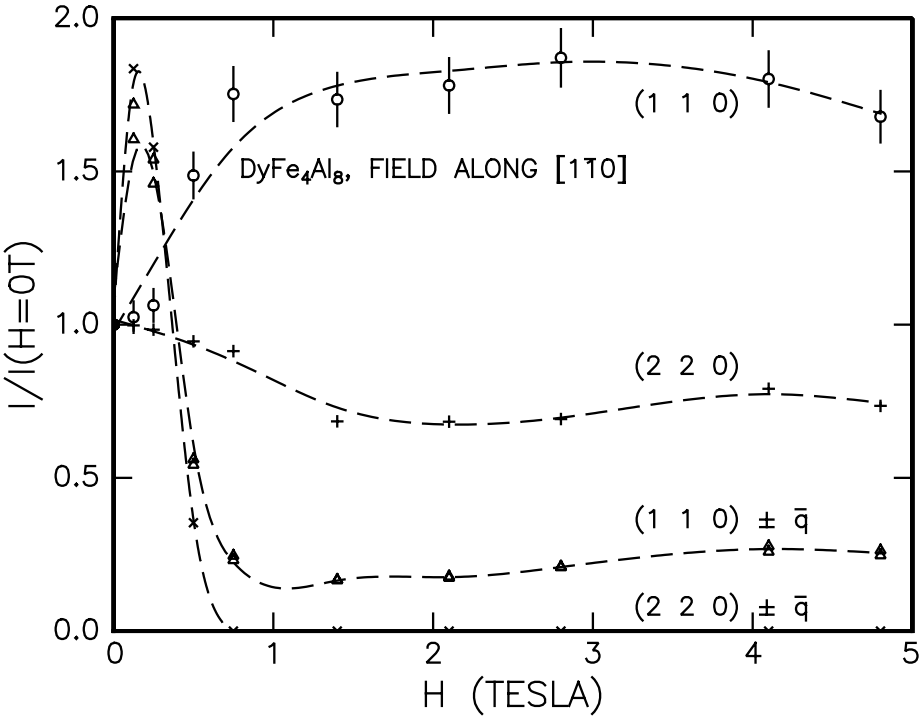

Figure 21. The relative peak amplitude of the (1 1 0)- *and* (2 2 0)*-reflections and their associated 1'st order magnetic satellites as a function of applied magnetic field. The data in the low field regime are from the TAS3 experiment, whereas the data at higher fields are from TAS1. The dashed curves are guides to the eye.*

satellites were not included in the graph shown in Fig. 21. These satellites appear around both the (1 1 0)- and (2 2 0)-reflections, and in the field range 0.125 T to 0.5 T we observe a smooth decay of these satellites with increasing temperature. However, at the field of 0.75 T, the 2'nd order satellites are absent at the lowest temperatures, but they appear accompanied by a steep increase of the intensity of the 1'st order satellites at approximately 10 K. In Fig. 22, the intensity of the (1 1 0) reflection and it's satellites are shown as function of temperature at the constant field of 0.75 T. It is clear, that at this field two separate phases are observed. At the lowest fields, the Dy-moments are aligned with the applied field, but above 10 K, these moments form a modulated structure with a 2'nd order component and a net moment.

A couple of times the question of the variation of nuclear intensities with temperature has been touched upon. In the TAS3 experiment, the intensity of the (1 1 0)-reflection increases in zero field by approximately 5% when cooling from 17 K to 2 K. Under the same conditions, the intensity of the (2 2 0) increases by 10%. Naively, one would interpret these observations as signs of a net moment developing at both Dy and Fe site at low temperature. However, no increase of the (1 1 0) intensity was observed in the D10 experiment using 1.26 Å incident neutrons. When checking the same intensity variations in the TAS1 experiment using 4 Å neutrons, the results were 14% increase of the (1 1 0) intensity and 33% increase of the (2 2 0) intensity. From measurements on large samples of rare earth metals, it is well known that due to magneto-elastic couplings, the extinc-

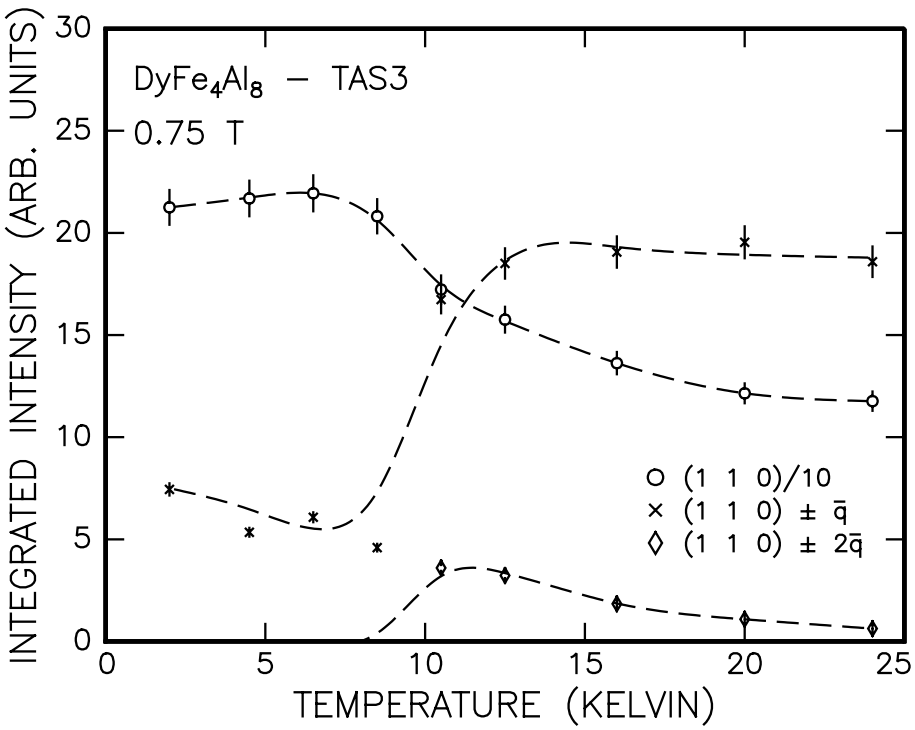

Figure 22. The integrated intensity of the (1 1 0)*-reflection and it's 1'st and 2'nd order satellites at 0.75 T. Note intensity of the main reflection has been divided by 10.*

tion effect may change dramatically in the process of magnetic ordering. Through the magneto-elastic couplings, the ordering of the magnetic moments may induce strain and hence increase the mosaicity of the sample. An increase in mosaicity will, in turn, decrease the effect of extinction in general, and since extinction is related to the crystal reflectivity, the effect of such an extinction release is expected to increase with wavelength and structure factor. This idea of extinction release was confirmed during the XRMS measurements, when the width of the rocking curve of a charge reflection was seen to increase as the sample was cooled down from 16 K to 12 K. We may estimate the effect of strain on the extinction corrections simply by scaling the mosaicity parameter of Zachariasen's extinction law [49] according to the extinction corrections measured at room temperature in the TAS2 experiment and the observed increases of intensity in nuclear reflections. In the TAS3 data taken at 2.36 Å incident wavelength, the observed increases of intensity are accounted for by a 30% increase of the mosaicity. To explain the intensity variation in the 4 Å data from TAS1, a somewhat higher mosaicity is needed. However, since change of mosaicity may not be reproducible and our calculations are only estimates in a regime of high extinction, this discrepancy need not indicate a real problem. The missing increase of intensity in the (2 2 0)-reflection when the external field is applied is also thought to be an effect of extinction. Whereas the modulated structure increases the mosaicity in zero field, the application of the field may decrease the mosaicity, thus increasing the extinction with the effect of quenching out the intensity from the ferromagnetic alignment of the moments.

If we reduce the extinction corrections at 2.36 Å by the estimate discussed above, the ordered moment at the Dy sites calculated from the D10 experiment is reduced from about 6 μ_B to 5.5 μ_B. The latter result is in agreement with the value calculated from the zero field part of the TAS1 experiment. We may calculate the size of the ferromagnetic moment at the Dy-sites from the difference between the

(1 1 0) intensity in zero field and the same intensity in applied field. However, in this case the question of extinction plays a crucial role for the correct separation of nuclear and magnetic scattering. In the framework of the Zachariasen formalism of extinction, the ferromagnetic alignment results in an increase of the structure factor. Since we have no knowledge on the change of mosaicity as a function of temperature and applied field, only a simple treatment of the extinction based on the Zachariasen formalism is attempted. From the extinction coefficient, y of the (1 1 0)-reflection transformed from the TAS2 result, we may estimate y as function of structure factor with all other parameters, i.e. scattering angle, wavelength, beam path and mosaicity kept fixed. Using this algorithm, we get a ferromagnetic moment at the Dy-sites of 8 μ_B. Again, using the simple approach to the extinction problem, we turn to the (2 2 0)-reflection and perform the reverse calculation: considering a simple estimate of the increase of extinction, we ask for the additional intensity in the (2 2 0)-reflection from a ferromagnetic moment of 8 μ_B at the Dy sites. The resulting estimate is a less than 10% increase of intensity, which could easily be compensated by the magneto-elastic effects as well as by the limitations of our treatment of the extinction. While keeping these complications in mind, we are led to the preliminary conclusion, that the full Dy moment is ferromagnetically aligned in a field of less than 1 T. We may overcome the problem of extinction in two ways: by reducing the size of the sample or by increasing it's mosaicity. Since we only have one single crystal of $DyFe_4Al_8$, we have retained from performing both kinds of modifications of the sample. We note, however, that the increase of mosaicity is often achieved by rapid cooling in liquid N_2 or by squeezing in a hydraulic press.

9 Diffuse scattering

In both the neutron experiments performed at the ILL and at Risø, strong diffuse scattering was observed around nuclear peaks when the sample was cooled well below the ordering temperature of the Dy sublattice. To further characterize this scattering, the zero field scans from TAS3 were manually filtered by simply deleting all data points belonging to resolution limited peaks from the background subtracted data. In Fig. 23, we show the result of this manual filtering of the scans along [1 1 0] at zero field and 2 K.

The centering of the diffuse scattering in the zone centers is clearly seen, and the scattering extends over the full Brillouin zone. The dashed curve in the figure shows the fit of the filtered data set to the sum of two Gaussian peaks. The same filtering and fitting have been applied to similar scans performed at 4 K, 6 K, 8 K, 10 K and 13 K. In Fig. 24, the peak height parameters of the Gaussian fits are shown as a function of temperature.

Based on the width and the positions of the diffuse components, they are ascribed to short-range ferromagnetic correlations in the sample. When applying the Lorentz correction and the Dy^{3+} form factor, the peak heights at the (1 1 0) and the (2 2 0) position are consistent, thus pointing to Dy as the only source of the diffuse component. In connection with the TAS1 experiment, the sample was mounted in a ^{4}He cryostat of the ILL Orange-type for a short run dedicated to the diffuse scattering. Firstly, at the position (1.21 1.21 0) a scan was performed in the transverse direction [0 0 1]. The position was chosen to be far away from the resolution limited peaks, and yet sufficiently close to the zone center to provide a reasonable diffuse intensity. In contrast to the longitudinal case, the width of the transverse scan was close to the resolution limit. See Fig. 25. Secondly, the quasi-elastic linewidth was measured by scanning the energy transfer at fixed mo-

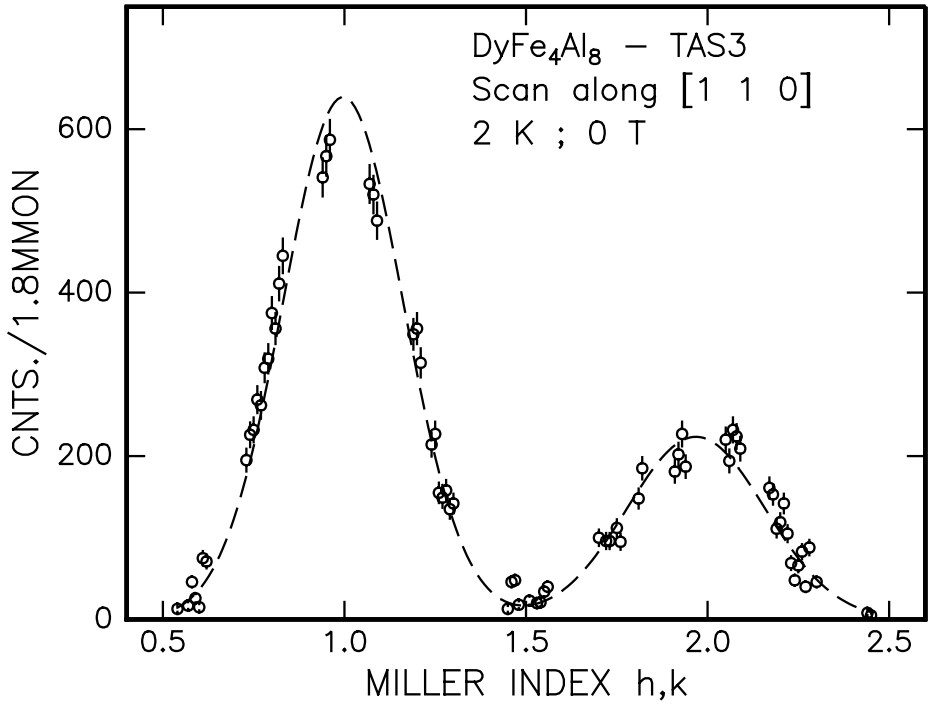

Figure 23. The diffuse component of the scattering measured in a scan along [1 1 0] *at 2 K and zero field. The dashed curve is a fit of a double Gaussian profile.*

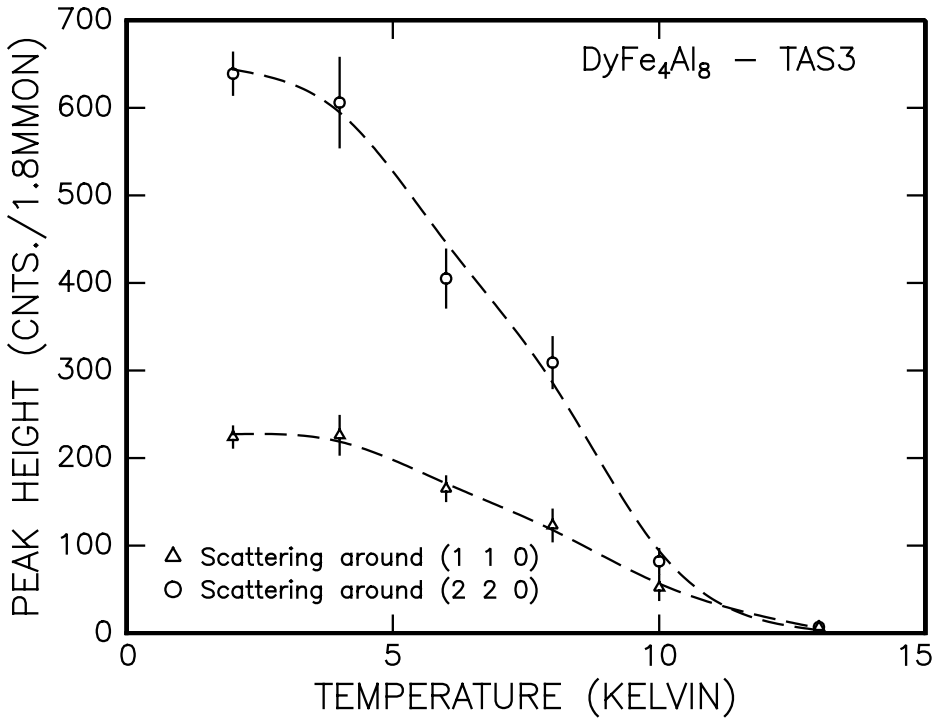

Figure 24. The peak height of the diffuse scattering as a function of temperature. The heights are extracted from Gaussian fits.

mentum transfer at the positions (1.21 1.21 0), (1.5 1.5 1.5) and (1.77 1.77 0). In all the cases, the lineshape was clearly not Gaussian. By fitting the data to a Voigt profile (a convolution of a Lorentzian response with a Gaussian resolution function) using resolution widths for each position calculated by RESCAL, the quasi-elastic linewidth was extracted. The results are listed in Table 6.

No significant change of the width is seen in the temperature interval 1.8 K

Temp.	(1.21 1.21 0)	(1.5 1.5 0)	(1.77 1.77 0)
1.7 K	40(1) μeV	71(4) μeV	40(1) μeV
2.8 K	39(1) μeV	85(5) μeV	40(1) μeV
3.8 K	38(1) μeV	74(4) μeV	41(1) μeV
5.8 K	41(1) μeV	74(4) μeV	42(1) μeV

Table 6. Quasi elastic width of diffuse scattering. The width is measured by scanning the energy transfer with fixed momentum transfer and incident energy. The momentum transfer is indicated in the top row of the table.

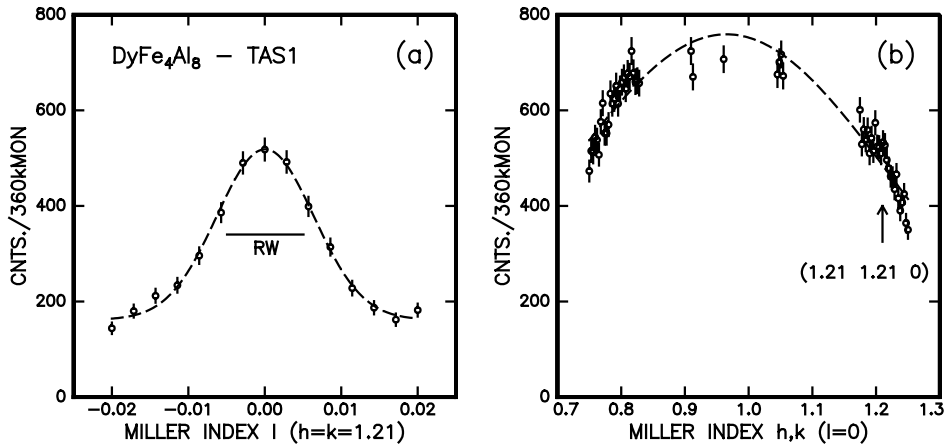

Figure 25. Scans of the momentum transfer perpendicular (a) and parallel (b) to the [1 1 0]*-direction. The center of the* (1.21 1.21 0) *of the l-scan in (a) is indicated by the arrow in (b). The solid line in (a) indicates the transverse resolution width as calculated by RESCAL.*

to 5.8 K. It is seen, that the width is significantly higher at the zone edge than at the points closer to the zone center. It should be noted, that the choice of (1.5 1.5 0) is somewhat misfortunate, since this point is sensitive to 2'nd order contamination of the incident beam. However no signs of a 2'nd order (3 3 0)-peak has been observed when scanning the momentum transfer. From the non-Gaussian (Lorentzian) lineshape and the finite width of the quasi-elastic scattering we conclude, that the short-range correlations giving rise to the diffuse scattering are fluctuating in time. To check the analysis of the quasi-elastic scattering, the energy transfer was scanned at the $(1-\xi\ 1-\xi\ 0)$ magnetic satellite. In this case, the line was Gaussian with a width corresponding to the calculated resolution. In order to further test the alignment and the resolution of the spectrometer, the energy transfer was scanned with a powder of vanadium at the sample table. The offset was less than 10 μeV and the width agreed with the RESCAL value within 10%.

The investigations and conclusions on the diffuse scattering leave many central questions unanswered. From the very limited studies of this scattering, we do not know the physical mechanism of the fluctuations. To answer the important question of the size of the magnetic moment involved in the fluctuations, we need a physical model with a scattering cross-section to include the resolution effects in a 4-dimensional $(\vec{q},\omega)$ fitting scheme.

10 A model of $DyFe_4Al_8$

In an attempt to obtain a more detailed understanding of the magnetic structures in $DyFe_4Al_8$, we shall formulate a simple phenomenological model of the system. The model is based on a few observations and assumptions: In accordance with the experiments, the crystal field anisotropy is assumed to keep the magnetic moments of both Fe and Dy within the basal plane, both under zero field conditions and with a field applied in the basal plane. In accordance with the conclusion in [8], we neglect the Dy-Dy interaction. The Fe sublattice is assumed to order in a sinusoidal cycloidal structure. That is, we neglect the influence of the Dy-ordering on the Fe sublattice, and we neglect any development of higher order harmonics at the Fe sublattice at low temperature. The latter assumptions are clearly an over simplification of the problem. However, the high ordering temperature of Fe compared to Dy and the apparently little effect of an applied field on the Fe modulation leave some hope, that our simple model may provide useful knowledge. In the Dy-Fe interaction, three different terms are considered: A Heisenberg-type exchange interaction. A crystal field term with the four-fold symmetry of the Dy-sites. The magnetic dipole coupling between Fe and Dy. Only the interaction of each Dy moment with the eight nearest neighboring Fe atoms is considered.

In a first consideration, we restrict the interaction to a single Heisenberg coupling. We may describe this interaction by a molecular field induced at the Dy sites by the assumed fixed Fe structure. The eight Fe sites nearest to the Dy-site $\vec{R}$ are:

$$\vec{R} \pm \begin{pmatrix} \frac{1}{4} \\ \frac{1}{4} \\ \frac{1}{4} \end{pmatrix} \quad \vec{R} \pm \begin{pmatrix} \frac{1}{4} \\ -\frac{1}{4} \\ \frac{1}{4} \end{pmatrix} \quad \vec{R} \pm \begin{pmatrix} -\frac{1}{4} \\ \frac{1}{4} \\ \frac{1}{4} \end{pmatrix} \quad \vec{R} \pm \begin{pmatrix} -\frac{1}{4} \\ -\frac{1}{4} \\ \frac{1}{4} \end{pmatrix} \tag{47}$$

To calculate the molecular field at the position $\vec{R}$, we sum the contributions from the eight Fe neighbors:

$$\vec{H}_{MF} \propto \sum_i \begin{pmatrix} \cos(\vec{q}' \cdot (\vec{R} + \vec{r}_i)) \\ \sin(\vec{q}' \cdot (\vec{R} + \vec{r}_i)) \\ 0 \end{pmatrix} = \begin{pmatrix} \cos(\vec{q} \cdot \vec{R}) \\ \sin(\vec{q} \cdot \vec{R}) \\ 0 \end{pmatrix} \sum_i \cos(\vec{q}' \cdot \vec{r}_i) \tag{48}$$

where $\vec{q}'$ denotes the modulation vector of the Fe-structure. In the last transformation, we have used the inversion symmetry among the set of Fe positions. Setting $\vec{q}' = (1+\xi, 1+\xi, 0)$, we further get:

$$\sum_i \cos(\vec{q} \cdot \vec{r}_i) = 4(1 - \cos(\frac{2\pi\xi}{2})) \tag{49}$$

Note, that the minus sign of the cos-term is due to the π phase shift of the Fe-structure. This ensures that the the molecular field at the Dy sites cancels in the case of the simple antiferromagnetic structure with π phase shift and $\vec{q} = 0$. Conversely, when $\vec{q} \neq 0$, the Fe moments give rise to a rotating molecular field at the Dy-sites resulting in a plain cycloidal modulation of the Dy-moments with no additional phase shift. This structure is illustrated in Fig. 26. The view is along the *c*-axis of the *bct* unit cell. The long arrows are the Dy moments whereas the shorter ones indicate the Fe magnetic moments.

Inserting value of $\xi = \frac{2}{15}$ gives the prefactor $4(1 - \cos(\frac{2\pi\xi}{2})) = 0.3458$. With a ferromagnetic alignment of the Fe-spins, this factor had been 8. Thus, the modulation of the Fe reduces the effective Dy-Fe-coupling by a factor of approximately 23 when comparing to a ferromagnetic alignment of the Fe. When we further take the four times larger moment of Dy into account, the ordering temperature of Dy

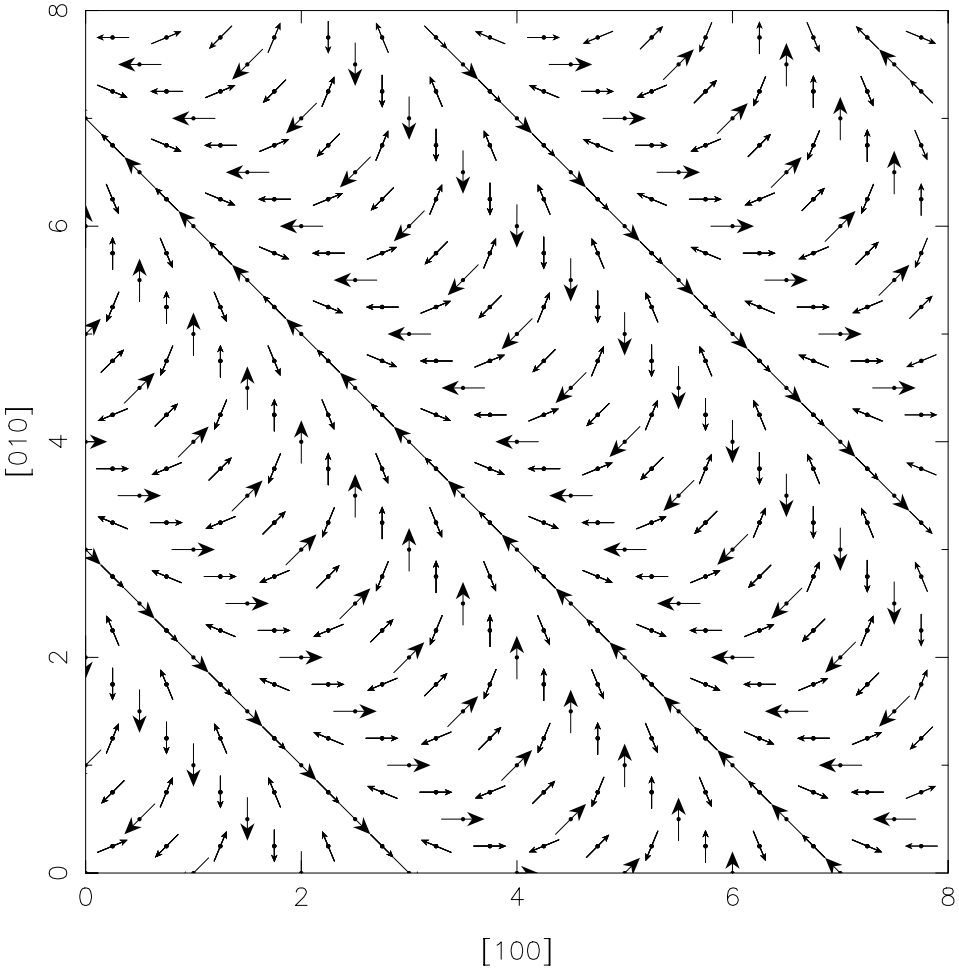

Figure 26. The plain cycloidal magnetic structure with the Heisenberg coupling as the only interaction in the simple model of $DyFe_4Al_8$*. The long arrows indicate Dy-moments, whereas the shorter ones are Fe moments.*

results in a Dy-Fe mean-field parameter of the same order of magnitude as the corresponding Fe-Fe parameter. This is in accordance with the results of [8], and, as mentioned above, a clear sign of a short coming of the model considered. We may estimate the size of the dipole interaction energy in a similar way. The energy of this coupling between two magnetic moments $\vec{\mu}_1$ and $\vec{\mu}_2$ is given by:

$$E_D = \frac{\vec{\mu}_1 \cdot \vec{\mu}_2 - 3(\vec{\mu}_1 \cdot \hat{r}_{12})(\vec{\mu}_2 \cdot \hat{r}_{12})}{|\vec{r}_{12}|^3} \tag{50}$$

where $\vec{r}_{12}$ is the vector from $\vec{\mu}_2$ to $\vec{\mu}_1$ and $\hat{r}_{12}$ is a unit vector parallel to $\vec{r}_{12}$. When inserting the numbers, we reach an energy of the dipole interaction between a Dy moment and it's Fe neighbors of less than 1 K. Thus, we shall not consider this term further. The third interaction, the crystal field anisotropy has it's origin in the electric field set up by the ions surrounding the Dy site. We know that the Dy site is on the 4-fold axis parallel to the c-axis, and at the intersection of the three mirror planes of the space group. Hence, the point group of the Dy site is D_{4h}. The crystal field term must be left invariant under the actions of this group. When expanding the field in terms of spherical harmonics, Y_l^m it is clear, that for all l only those m-values that are integer multiples of four can be accepted. The terms with $m = 0$ are independent of the moment orientation in the basal plane. The effect of these terms is to keep the moments in the basal plane. Furthermore, since f-electrons have the individual orbital quantum number $l = 3$, matrix elements of Y_l^m between these states must cancel for $l > 6$. We are now left with $Y_4^{\pm 4}$ as the

only possible source of in-plane anisotropy. Hence, we may represent the crystal field interaction by the term $B_4\mu^4\cos(4\phi)$ with ϕ being an orientation angle in the basal plane. Finally, to model the length of the ordered Dy-moment, we include terms in second and fourth order of this quantity in a phenomenological free energy function for the Dy-sublattice:

$$F = \sum_{\vec{R},Dy} \left(A_2\mu^2_{Dy,\vec{R}} + A_4\mu^4_{Dy,\vec{R}} + J_1 \sum_{i,Fe} \vec{\mu}_{Dy,\vec{R}} \cdot \vec{\mu}_{Fe,i} + B_4\mu^4_{Dy,\vec{R}}\cos(4\phi_{\vec{R}}) \right) \quad (51)$$

with the second summation over index i including the eight nearest neighboring Fe atoms. The magnetic structure of the Dy-sublattice is written as the Fourier expansion:

$$\vec{\mu}_{Dy,\vec{R}} = \sum_{n=-\infty}^{\infty} \vec{\mu}_{Dy,n} e^{\imath n\vec{q}\cdot\vec{R}} \quad (52)$$

As in the data analysis, the simple cycloidal structure is assumed. This means that Fourier coefficients $\vec{\mu}_{Dy,n}$ have the form:

$$\vec{\mu}_{Dy,n} = \mu_{Dy,n} \begin{pmatrix} 1 \\ \pm\imath \\ 0 \end{pmatrix} \quad (53)$$

With up to fifth order Fourier components included in the magnetic structure, the energy (51) has been minimized with respect to the amplitudes and phases of the components. For the minimization, the Levenberg-Marquart algorithm implemented in the CERN library package "MINUIT" [17] was used. Attempts to obtain amplitudes of the 1'st, 3'rd and 5'th order coefficients matching the satellite intensities measured in the D10-experiment did not succeed. However, since the "MINUIT" code is not reentrant, it was not possible to perform a true least square fit of the model parameters by means of this package and the fitting of these quantities was limited to a grid search. It is obvious that a detailed understanding of the magnetism of $DyFe_4Al_8$ requires a lot more work in the area of modeling. As a first step, the problems regarding parameter fitting in the proposed model should be solved. Further more, an experimental determination of the crystal field parameters would be useful. The effect upon the Fe-structure of Dy ordering should be included in a self-consistent scheme. The time frame of the present work did not allow a more thorough treatment of the modeling aspects. It is the hope that results and ideas presented in this chapter would encourage others to further pursue the many open questions.

Part III
MnSi

The period of a modulated magnetic structure is often of the order of a few chemical unit cells. However, in a family of compounds with the crystal structure $P2_13$, magnetic modulation periods of several hundred chemical unit cells have been observed. MnSi is one such example. It orders in a helical structure with a period of 180 Å at 29.5 K. It has been demonstrated [2] that the support of long period magnetic structures in the $P2_13$-compounds is closely connected with the lack of inversion symmetry in the space group. In several experiments, the application of an applied hydrostatic pressure has shown remarkable effects on macroscopic magnetic and electrical properties [5], [44]. In the present work, the effect of applied pressure on the magnetic structure of MnSi has been studied by small angle neutron scattering (SANS). From previous neutron scattering experiments, critical scattering of a spherical shape has been reported [26], [7]. In this part of the thesis, we report on new studies of the critical scattering by the SANS technique. Polarized neutron beams have previously been applied by Ishida and coworkers in neutron scattering experiments on MnSi using the time of flight technique. It was demonstrated in these experiments that the chiralities of the chemical and the magnetic structures of MnSi are locked together. In the final section of this chapter, a new polarization device based on multi-layer coated Si-wafers is described. The device was developed in collaboration with the Institut Laue Langevin, Grenoble, France, and it was designed specifically for SANS instruments. The observation of a single chirality domain in a MnSi sample was used as a test experiment for our polarization device.

11 Previous work

The literature on experimental as well as theoretical studies of the magnetism of MnSi is overwhelming. In this section, we briefly summarize those contributions that appear most relevant as background for the present work.

The crystal structure of MnSi has been solved by Borén using X-ray diffraction [6]. It has the cubic space group $P2_13$ containing pure 3-fold axes along the $< 111 >$ space diagonals and 2-fold screw axes parallel to the cube axes. The group does not contain the inversion. As has been demonstrated by anomalous X-ray scattering, crystals may grow with either of the two possible chiralities.

The first single crystal neutron scattering experiment on MnSi was performed by Ishikawa *et al.* [29]. At the Néel point of 29.5 K, magnetic satellites appear along equivalent $< 111 >$-directions at a distance of 0.035 $Å^{-1}$ from the nuclear peak. In total, four pairs of magnetic satellites appear around the forward direction and the nuclear reflections. One may interpret the magnetic diffraction pattern as the result of either a multi domain structure with a single magnetic modulation vector or a single domain of a multi-$\vec{q}$ structure. In addition to zero-field measurements, a magnetic field was applied along $< 110 >$- and $< 111 >$-directions. In the former case, additional satellites appeared at low fields at positions corresponding to the vector sum of the main positions. Upon application of higher fields along [110], the main satellites gradually rotate towards the field direction, and the modulation vector becomes completely aligned with the field at 0.39 T. When applying the external field along a $< 111 >$-direction, the intensity of the satellites along

the field direction increases at the expense of the other satellites. When lowering the field, the intensity shows a strong hysteresis. In the paper [29], this effect is interpreted as a sign of a multi domain, single-$\vec{q}$ structure. Since a discontinuous change of the magnetization is absent only when the field is applied in a $< 111 >$-direction, the paper assumes that the spin configuration is helical with the spins rotating in the plane perpendicular to the modulation vector. Based on the intensity of the magnetic satellites, the ordered moment in zero field is estimated as 0.4 μ_B. From measurements of magnetization at high temperatures and from studies of the temperature dependence of nuclear magnetic relaxation in the paramagnetic regime, the authors conclude that MnSi is an itinerant magnetic system.

By a Landau-type expansion of the free energy combined with symmetry analysis, Bak and Jensen [2] showed that the stabilization of the long period magnetic structures in $P2_13$-compounds is closely connected to the lack of inversion symmetry in the crystal structure. The formation of the modulated magnetic structure is described as a destabilization of a ferromagnetic configuration due to small antisymmetric terms in the free energy expansion. A few years later, these spin-orbit and spin-spin terms were derived from a microscopic Hamiltonian [31]. The reorientation of spins and modulation vector in applied field was treated by Plummer and Walker [46] by revising and extending the theory of Bak and Jensen.

In another $P2_13$-compound, FeGe [35], a magnetic ordered phase with $\vec{q}$ along $< 100 >$ is observed from 280 K. From approximately 210 K, the direction of the modulation vector changes to $< 111 >$. This reorientation was treated by Plummer [45] along the lines of the previous theoretical work.

The phase diagram of MnSi in magnetic field applied along the [001]-direction has been studied in great detail by Lebech *et al.* [36] and Harris [22] using small angle neutron scattering. The results are summarized in Fig. 27. Six distinct phases are seen in the middle panel of the figure. At the lowest fields in phase (d), the two pairs of satellites along [111] and [11$\overline{1}$] are observed as shown in the lowest diffraction pattern of the figure's left panel. In the phase (c), the modulation vector starts rotating towards the direction of the field until it is completely lined up along the field (a). This behavior is in agreement with the reorientation theory of Plummer and Walker [46]. However, an unexpected phase pocket appears close to the paramagnetic/ferromagnetic region in the rightmost part of the diagram. The pocket was first discovered by Ishikawa and Arai [25] and since no satellites were observed in the [110]-[001]-plane, the pocket was interpreted as a paramagnetic region. By rotating the crystal by $\pm 45°$ around the [001] field direction, Lebech [34] demonstrated that in the phase pocket, the system is still in a modulated magnetic phase but the direction of $\vec{q}$ has changed to the two $< 100 >$-directions perpendicular to the field. Such a reorientation is not expected from the theory of Plummer and Walker. The diffraction patterns from the crystal in this phase (e) are shown in the two upper panels of the right hand part of Fig. 27.

The relationship between the chirality of the chemical unit cell and that of the magnetic structure was addressed by Ishida and coworkers [24] in a time of flight type neutron scattering experiment using a polarized incident beam. As expected from the model of Bak and Jensen, the chiralities of the crystal and the magnetic structures are locked together.

The magnetic fluctuations in the vicinity of the magnetic ordering and in the paramagnetic regime have been the subject of detailed studies by Ishikawa and various coworkers [28], [26] and [27]. At temperatures well above the Néel point,

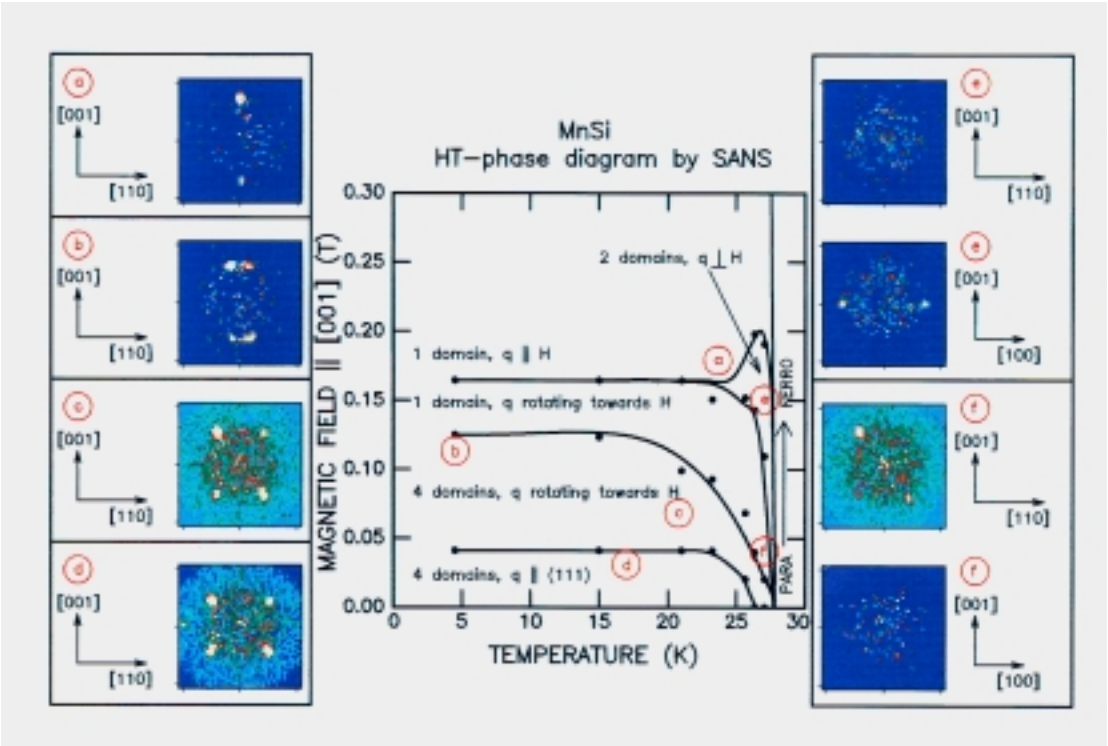

Figure 27. Summary of the HT-phase diagram of MnSi with field along the [001]*-direction. Representative diffraction patterns are shown to the right and left. The figure appears by courtesy of B. Lebech.*

the magnetic properties of MnSi resemble those of an itinerant ferromagnetic system. According to a theory put forward by Moriya and coworkers (the self consistent renormalization (SCR) theory, see references in [26]), the q-dependence of the inelastic linewidths observed in the itinerant system should be distinctly different from that found in the localized Heisenberg system. According to the authors of [26], their inelastic neutron scattering studies are the first experimental demonstration of this linewidth effect. In the critical region, both Ishikawa *et al.* [26] and Brown [7] observe a transverse elongation of the magnetic satellites which develops into a ring-shaped contour of intensity in the scattering plane.

Macroscopic magnetic and electric properties of MnSi have been studied under the application of hydrostatic pressure. In the pressure range up to 5.2 kbar, Bloch *et al.* [5] observed a decrease of ordering temperature upon increasing pressure at the rate $d \log T_N/dP = -3.9 \times 10^{-2}$/kbar. In later experiments of similar type, Pfleiderer *et al.* [44] succeeded to suppress the magnetically ordered phase by the application of 14.5 kbar hydrostatic pressure. Furthermore, they report a cross-over of the transition at the Néel point from second order to first order as the pressure is increased beyond 12 kbar.

12 High pressure SANS experiment

Based on the observed effect of pressure upon macroscopic properties, it was decided to study the microscopic magnetic structure of MnSi under applied hydrostatic pressure. As the separation of the magnetic satellites from the nuclear

peaks (or direct beam) is only 0.035 $Å^{-1}$, it was decided to conduct the experiment at a diffractometer specially designed for small angle neutron scattering (SANS). At Risø, a SANS instrument is installed at the cold neutron source of the DR3 reactor. Logically, the Risø SANS machine divides into four sections: The monochromator, the collimation section, the sample table and the detector. For the monochromatization of the incident neutron beam, a rotating velocity selector gives access to neutron wavelengths in the range 3 - 24 Å with adjustable resolution between 10 and 20%. Between the velocity selector and the sample table there is an evacuated flight-path with 1 fixed and 5 movable sections of 1 m long Ni-coated neutron guides. In combination with a set of pinholes, this flight-path collimates the incident beam. By adjusting the sizes of the pinholes and changing the effective path length by moving the guide sections in or out, one may optimize the collimation to match the requirements of the experiment. At the sample position, a motorized turn-table with a single goniometer arc and manual translations in the xy- and z-directions accepts a wide range of sample environments including variable temperature cryostats, cryomagnets and furnaces. Finally, the detector is a 60 by 60 cm^2 multi wire type ^{3}He filled area detector with 128 by 128 channels. The position of a detected neutron is determined from the difference between the arrival time of the signal at the two ends of a detector wire. Depending on the configuration of the detector electronics, the position resolution of the detector system is of the order 1 cm. Inside a vacuum tank, the detector is moving on a set of rails allowing the sample to detector distance to be varied between 1 and 6 m. The intensity of the incident neutron beam is monitored by a low efficiency ^{3}He-counter. All the major parameters including the sample orientation and the data acquisition are controlled by a micro-VAX system. This allows for a large degree of automation in the collection of data.

12.1 Experimental details

For the pressurization of the sample, a commercially available pressure cell [41] of the McWhan type was used. The sample space of the cell is cylindric with height 10 mm and diameter 6 mm. A main advantage of the McWhan design is the full 360° neutron window. The principle of the cell is sketched in Fig. 28. A key component of the cell is the barrel-shaped hollow device ("Cylinder") supporting the sample can. Prior to the pressurization of the sample space, the supporting device is pre-stressed in a hydraulic press by means of the two wedge-shaped rings ("Support ring"). While maintaining the load of the press, the upper wedge ring is clamped with a ring bolt ("Clamping ring"). The sample is kept in a can made from a neutron transparent Al alloy. To obtain a hydrostatic pressure inside the can, the sample is surrounded by some pressure transmitting medium. The can fits into the cavity of the supporting device, and a pair of pistons locks up the cell from top and bottom. The pressurization of the sample is again done in a hydraulic press. In this case an additional outer piston transfers the load of the press to the upper internal piston of the cell. The outer shape of the cell is cylindric. It has a diameter of 100 mm and a height of 140 mm. The total weight of the cell is approximately 5 kg. The maximum achievable pressure in the cell depends on the choice of supporting device. In standard configuration, a supporting device made of hot pressed Al_2O_3 powder allows for 25 kbar pressure. However, the small angle neutron scattering from the Al_2O_3 grains is substantial and it results in an unacceptable high background signal in the measurements. To overcome this problem, a supporting device made from a single Al_2O_3 crystal was applied. In this case, the maximum pressure is only 7 kbar, far below the 15 kbar pressure observed to suppress the magnetic ordering. As the pressure transmitting medium, the prod-

uct Fluorinert FC-75 from 3M Company was used. This medium is a CFC-type liquid where all hydrogen has been substituted by fluorine.

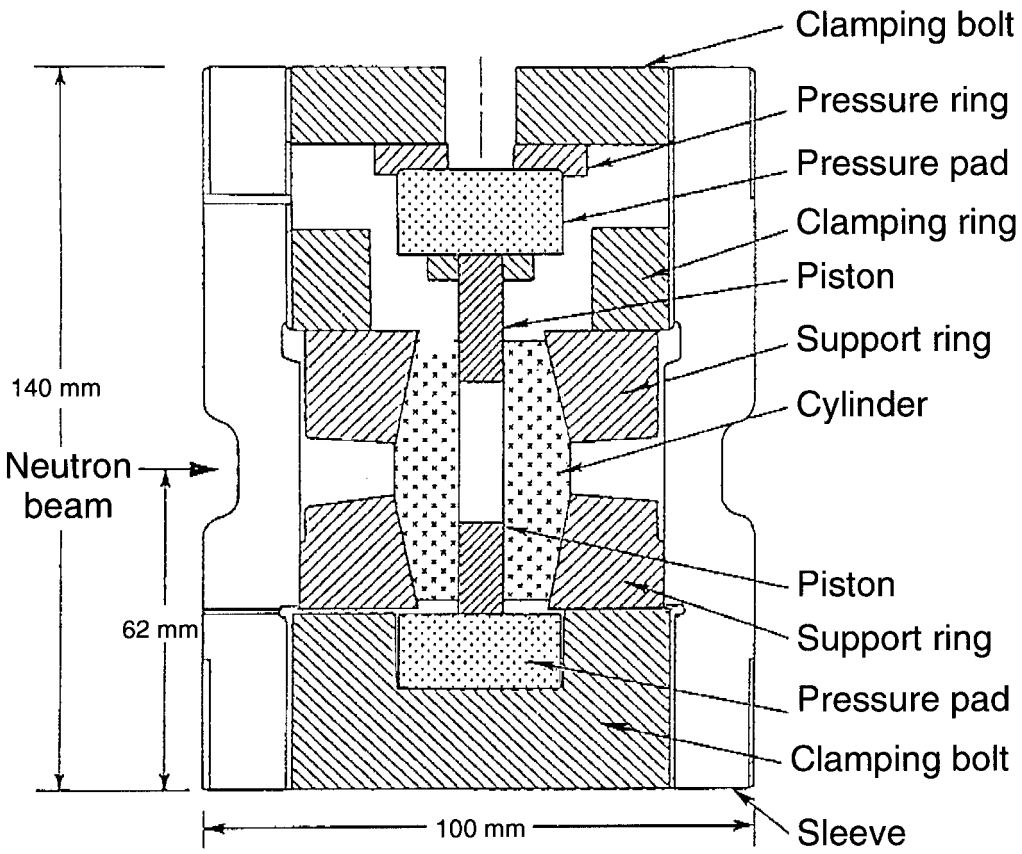

Figure 28. The McWhan-type high pressure cell used for SANS experiment on MnSi.

Low temperature conditions were obtained in combination with high pressure by attaching the cell to the cold tip of a closed-cycle refrigerator (a "Displex"). To mount the cell with good thermal contact, a Cu disk was clamped to the top of the cell. By a long thread, this disk was screwed onto a Cu block holding thermometers and heater cartridges. In turn, this block was fitted on the cryostat tip. An extra set of thermometers was mounted in the bottom of the pressure cell sleeve. When controlling the heater cartridge current by a standard Risø temperature controller, the temperature of the cell could be controlled in the region 8 - 120 K. Temperature differences of no more than 0.5 K were observed between the upper temperature control block and the bottom of the pressure cell.

The MnSi sample used for the experiment was an approximately 3 mm high cylinder of diameter 1 mm. With the [001]-direction vertical, the sample was fitted into a small Al disk fitting into the sample can. In the can, the Al disk with the MnSi sample was placed on top of a 4 mm high NaCl single crystal oriented with it's [001]-direction vertical. As an introductory part of the experiment, the sample can with sample, NaCl and the pressure transmitting fluid was mounted in the cell without any pressurization. With the cell mounted in the cryostat and the SANS instrument operated in a mode using 7 Å (18%) incident neutrons, it was checked that previously obtained results in ambient pressure [22] were reproduced. Both the general features and T_N were in agreement with the earlier observations. The confirmation of T_N was taken as an indication that the temperature of the

sample was in agreement with our measurements at the top and at the bottom of the pressure cell. After loading the cell in a hydraulic press, the pressure was established by measuring the lattice parameters of the NaCl crystal included with the sample. The relationship between applied pressure and NaCl lattice parameters has been established [12] from a theoretical equation of state. The estimated pressure value was 4.5 kbar $\pm$ 0.5 kbar. After the pressure had been measured at room temperature, the sample was cooled down to 8 K in the cryostat. In the cold state the pressure was checked once more by measuring the NaCl lattice parameters. Experience has shown that when the McWhan-type cell is used in the low pressure range below 10 kbar, the pressure is often lost upon thermal cycling. Therefore, the pressure cell was kept at a temperature below 100 K during the remaining part of the experiment.

The cryostat was now remounted on the sample table of the SANS instrument. Again, the SANS instrument was operated using 7 Å incident neutrons with a relative wavelength resolution of 18%. For the collimation, a 16 millimeter pinhole was used at the source. To reduce the background scattering from the steel parts of the pressure cell, the beam was narrowed down to 4 mm at the sample end of the collimating flight-path.The effective source to sample and sample to detector distances were both 3 meters. The diffraction pattern was recorded during rotation of the sample in a 180° angular interval at temperatures ranging from the 8 K cryostat base up to 1 K above the Néel point. For background correction, a full rotation series of diffraction patterns was recorded at 40 K.

12.2 Data analysis

All the low temperature diffraction patterns were corrected for various background signals and detector imperfections using the following procedure:

- The intensities of every pattern were normalized with respect to the beam monitor counts obtained during the recording.
- From every low temperature pattern, the 40 K pattern recorded with the same sample orientation was subtracted.
- These background subtracted patterns were corrected for inhomogeneous detector efficiency by division by a reference water spectrum.

Since water is an almost perfect isotropic scatterer, the distribution of intensity recorded in the water spectrum represents the distribution of detector efficiency. The reference spectrum had been corrected for the background scattering from the cuvette keeping the water sample. Typical color maps of the corrected intensity distribution ("SANS frames") recorded in the [100]-[001]-plane are shown in Fig. 29. The series of frames shown are recorded at temperatures ranging from 8 K - 24.5 K.

The distribution of intensity in every diffraction pattern has been analyzed using a circular and a radial averaging. In the circular averaging, the scattering recorded in the momentum transfer range 0.025 - 0.050 $Å^{-1}$ is summed in 63 radial sections. In the radial averaging, the intensity is summed in 47 concentric circular sections.

From the radial averaging, the length of the modulation vector *vs.* temperature has been extracted (see Fig. 31). The length of $\vec{q}$ has increased by approximately 15% relative to the value obtained at ambient pressure. From the circular averaging, we have extracted the angular position of the magnetic satellites in the diffraction plane. Plots of the radial and the angular distribution of intensity in

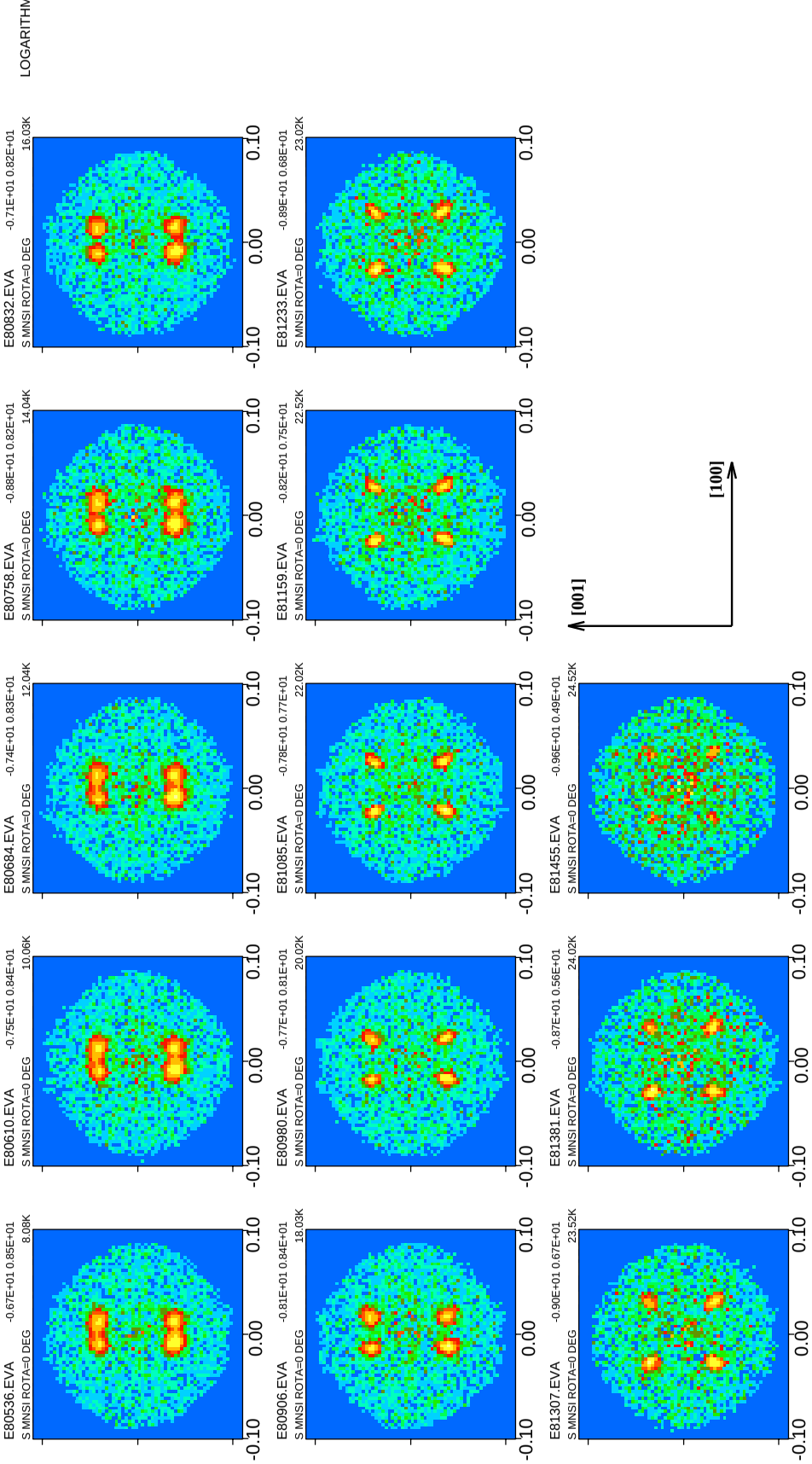

Figure 29. Typical corrected SANS frames recorded in the [100]-[001]*-plane at temperatures ranging from 8 K to 24.5 K. When rotating the page by 90 degrees clockwise, the* [100] *direction is along the horizontal axis of the frames and the* [001] *is along the vertical. Note, that each frame is shown on an individual logarithmic scale.*

the [100] − [001]-plane at the temperatures 8 K and 22 K are shown in Fig. 30. The extracted values for the angle between the modulation vector and the vertical [001]-direction measured in the [100]-[001]-plane are shown as a function of temperature in Fig. 32.

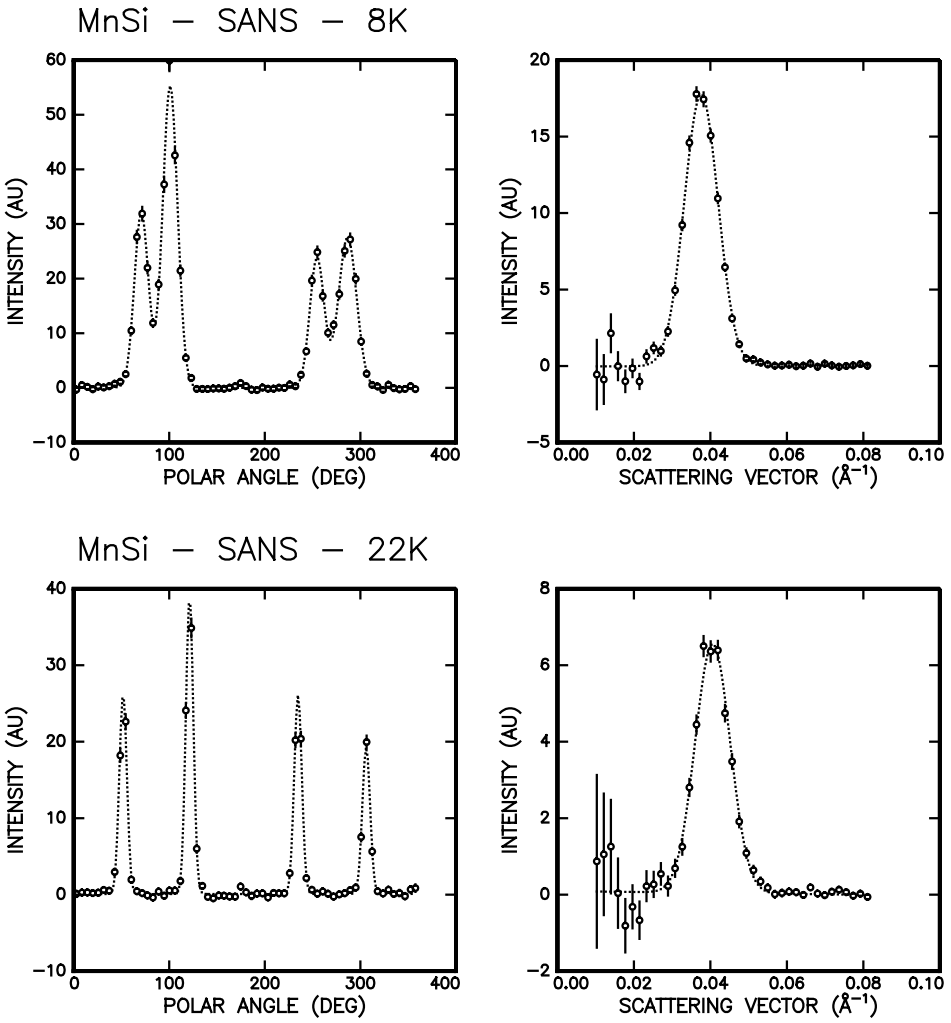

Figure 30. MnSi under 4.5 kbar pressure. The angular (left panel) and radial (right panel) intensity distribution in diffraction patterns recorded in the [100]-[001]*-plane. The upper panel of the figure is extracted from data taken at 8 K whereas the data of the lower part were taken at 22 K. The dotted curves are the results of Gaussian fits.*

To get an overview of the rotation of the modulation vector, the angular distributions of intensity in all the 73 SANS frames recorded at each temperature have been visualized in color maps as shown in Figs. 33 and 34. Along the horizontal axis of the map, we have the sample rotation around the [001]-direction. Zero orientation angle corresponds approximately to having [100] parallel to the diffraction plane. Along the vertical axis, we have the angle in the diffraction plane. This angle is measured from a direction in the diffraction plane perpendicular to the [001] and positive towards this direction. Hence, for $\vec{q}$ along [111] as in MnSi under ambient pressure, we should see a peak in the color map at sample rotation angles ±45° and polar angles 35.26°, 144.74°, 215.26° and 324.74°. The maps of Fig. 33 are composed from data taken at 8 K (upper map) and data taken at 20 K.

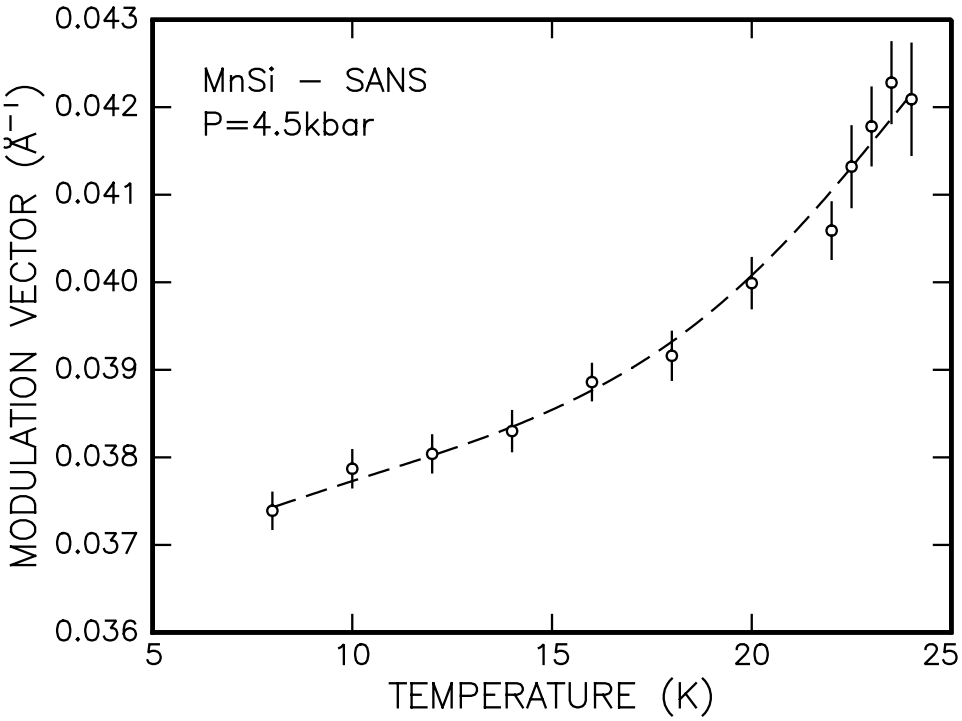

Figure 31. MnSi under 4.5 kbar pressure. The length of the modulation vector $\vec{q}$ versus temperature. The dashed curve is a guide to the eye.

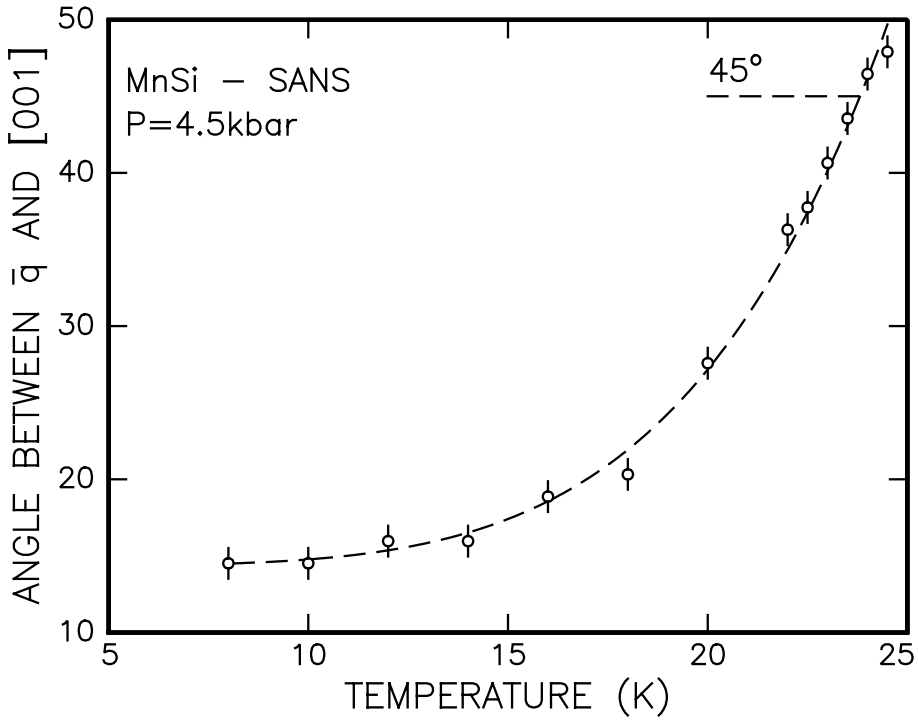

Figure 32. MnSi under 4.5 kbar pressure. The angle between the modulation vector $\vec{q}$ and the [001] *vertical direction is measured in the* [100]-[001]*-plane. Note that $\vec{q}$ gets close to the* [101]*-direction at the Néel point. The dashed curve is a guide to the eye.*

Maps of data taken at 22 K and 24 K are shown in Fig. 34. It is clearly seen that in the whole temperature range, the modulation vector is in the [100]-[001]-plane. Just before the disappearance of magnetic scattering, $\vec{q}$ is close to the [101]- and [10$\overline{1}$]-directions. With the present angular resolution in the diffraction plane, we

cannot determine whether the modulation vector locks into $< 110 >$-directions at the Néel point. In contrast with observations at ambient pressure, the magnetic satellites are rather broad along the sample rotation axis. At 20 K, intensity is still observable at sample rotations of $\pm 45°$.

As the satellites move towards the [001] direction (90° and 270° polar angle) upon decreasing the temperature, the "halo" of intensity is getting curved. There is a systematic difference in intensity between the two pairs of satellites presumably caused be a domain selection mechanism. The skewness of the line through the four intensity maxima is caused by a misalignment of the crystal. In a SANS experiment, the alignment of the crystal is complicated by the inaccessibility of nuclear Bragg reflections. At the Risø SANS instrument, the absence of a second arc on the sample goniometer is a further complication.

To estimate the Néel temperature, the intensity in the momentum transfer region 0.02-0.06 $Å^{-1}$ has been summed and plotted as a function of temperature. The result of $T_N \approx 25$ K agrees well with the observations of Pfleiderer *et al.* [44].

12.3 Discussion of the results

The selection of the vertical [001] as a preferred direction for $\vec{q}$ at low temperatures and 4.5 kbar pressure, the selection of the [001]-[100]-plane at the cost of the [010]-[001]-plane and the difference in intensity of the two domains with $\vec{q}$ in the [100]-[001]-plane is unexpected as a result of the application of a hydrostatic pressure since the three $< 100 >$-directions should remain equivalent. Furthermore, the observation of $\vec{q}$ close to $< 110 >$-directions at high temperature is in contradiction with the theory of Bak and Jensen [2] and with the work of Plummer [46], [45]. All theses observations suggest an inhomogeneity in the deformation of the sample crystal. In an attempt to interpret the results, we outline the approach of Plummer and Walker [45] in some detail.

The key point in the theoretical work of both Bak and Jensen [2] and Plummer and Walker [46] is an expansion of the free energy in spin density and the modulation vector. However, the starting point of the two groups are quite different. Bak and Jensen assume that the total free energy of the magnetic system may be written as an integral of a local free energy density expandable in powers of the order parameter (the spin density) and it's derivatives. According to Plummer and Walker, this assumption is not valid in general. Hence, the latter authors chose as their starting point an expression for the spin density of the form:

$$\vec{s}(\vec{r}) = \vec{m} + \vec{S}e^{\imath\vec{q}\cdot\vec{r}} + \vec{S}^* e^{-\imath\vec{q}\cdot r}$$

where $\vec{m}$ is a constant (ferromagnetic) contribution to the spin density. The free energy, in turn, is assumed to be a function of $\vec{S}$, $\vec{m}$ and $\vec{q}$. All terms of the orders S^2, m^2, qS^2, q^2S^2, m^2S^2, S^4 and m^4, which are invariant under the operations of the crystal symmetry group and the operation $\vec{S} \to \vec{S}^*$, $\vec{q} \to -\vec{q}$ are considered. As all the three vectors are defined as invariant under translation, the symmetry group considered is in fact not $P2_13$ itself but it's point group T. Group theory offers a systematic and elegant way of identifying the allowed terms. Details of the method with references are given in [30]. At this place, we merely note, that the characters of those (reducible) representations formed when taking second and fourth order symmetric or anti-symmetric product combinations of vector elements as basis are calculated according to formulae found in [32] and [30]. From these characters, the reducible components of the product representations are identified and those products forming the basis of the identical irreducible representation

(often designated by A [32]) are selected. Since these product combinations of vector components are invariant under T, they are exactly the higher order vector terms acceptable in the free energy expansion. When forming second order symmetric combinations, we find that the scalar product of two vectors

$$\vec{A} \cdot \vec{B} = A_x B_x + A_y B_y + A_z B_z$$

is invariant under T whereas the symmetric product combination:

$$\begin{pmatrix} A_y B_z + A_z B_y \\ A_z B_x + A_x B_z \\ A_x B_y + A_y B_x \end{pmatrix}$$

and the anti-symmetric product combination:

$$\vec{A} \times \vec{B} = \begin{pmatrix} A_y B_z - A_z B_y \\ A_z B_x - A_x B_z \\ A_x B_y - A_y B_x \end{pmatrix}$$

both transform as vectors under T. Hence, we have identified the second order scalar product term and possible third and fourth order terms formed with the 3-dimensional vector-like combinations appearing in scalar products. In a similar way, the characters of those representation formed from fourth order symmetric and anti-symmetric combinations of vector elements are calculated and the invariant combinations are identified. The invariant combinations take the forms:

$$A_x B_x C_x D_x + A_y B_y C_y D_y + A_z B_z C_z D_z$$

and

$$(\vec{A} \cdot \vec{B})(\vec{C} \cdot \vec{D})$$

We may now collect the combinations up to fourth order in the spin density and up to second order in the gradient following the above given scheme to get the desired expansion of the free energy [46]:

$$\begin{aligned} F &= \frac{1}{2} A_0 m^2 + A_0' \vec{S} \cdot \vec{S}^* + A_2 q^2 \vec{S} \cdot \vec{S}^* + B_1 m^2 \vec{S} \cdot \vec{S}^* + B_2 (\vec{S} \cdot \vec{S}^*)^2 + \\ & 2B' |\vec{m} \cdot \vec{S}|^2 + \frac{1}{2} B'' |\vec{S} \cdot \vec{S}|^2 + \frac{1}{4} B_3 m^4 - \vec{m} \cdot \vec{H} + \imath C \vec{q} \cdot (\vec{S} \times \vec{S}^*) + \\ & D_1 \left[q_x^2 |S_y|^2 + q_y^2 |S_z|^2 + q_z^2 |S_x|^2 \right] + \\ & D_2 \left[q_x^2 |S_z|^2 + q_y^2 |S_x|^2 + q_z^2 |S_y|^2 \right] + \\ & D_3 |\vec{q} \cdot \vec{S}|^2 + \\ & J_1 \left[m_x^2 |S_y|^2 + m_y^2 |S_z|^2 + m_z^2 |S_x|^2 \right] + \\ & J_2 \left[m_x^2 |S_z|^2 + m_y^2 |S_x|^2 + m_z^2 |S_y|^2 \right] + \\ & E(|S_x|^4 + |S_y|^4 + |S_z|^4) + I(m_x^4 + m_y^4 + m_z^4) \end{aligned} \tag{54}$$

The antisymmetric so-called Dzyaloschinskii-Moriya (DM) term, $\imath C \vec{q} \cdot (\vec{S} \times \vec{S}^*)$ was first identified by Bak and Jensen as responsible for the long period magnetic structure. The Zeeman coupling, $-\vec{H} \cdot \vec{m}$ is included to account for an external applied magnetic field, $\vec{H}$. In the treatment of Plummer and Walker, the free energy is simplified by assuming a helical structure with $\vec{S}$ perpendicular to $\vec{q}$, by averaging the anisotropy parameters $D = \frac{1}{2}(D_1 + D_2)$ and by neglecting the anisotropy terms in the magnetization, $\vec{m}$:

$$\begin{aligned} F &= \frac{1}{2} A_0 m^2 + (A_0' + A_2 q^2 + Cq) S^2 + B(m^2 S^2 + S^4 + \frac{1}{4} m^4) + B' m_\perp^2 S^2 + \\ & (\frac{1}{2} D q^2 S^2 + \frac{1}{4} E S^4) g - \\ & m_\parallel H \cos\theta - m_\perp H \sin\theta \end{aligned} \tag{55}$$

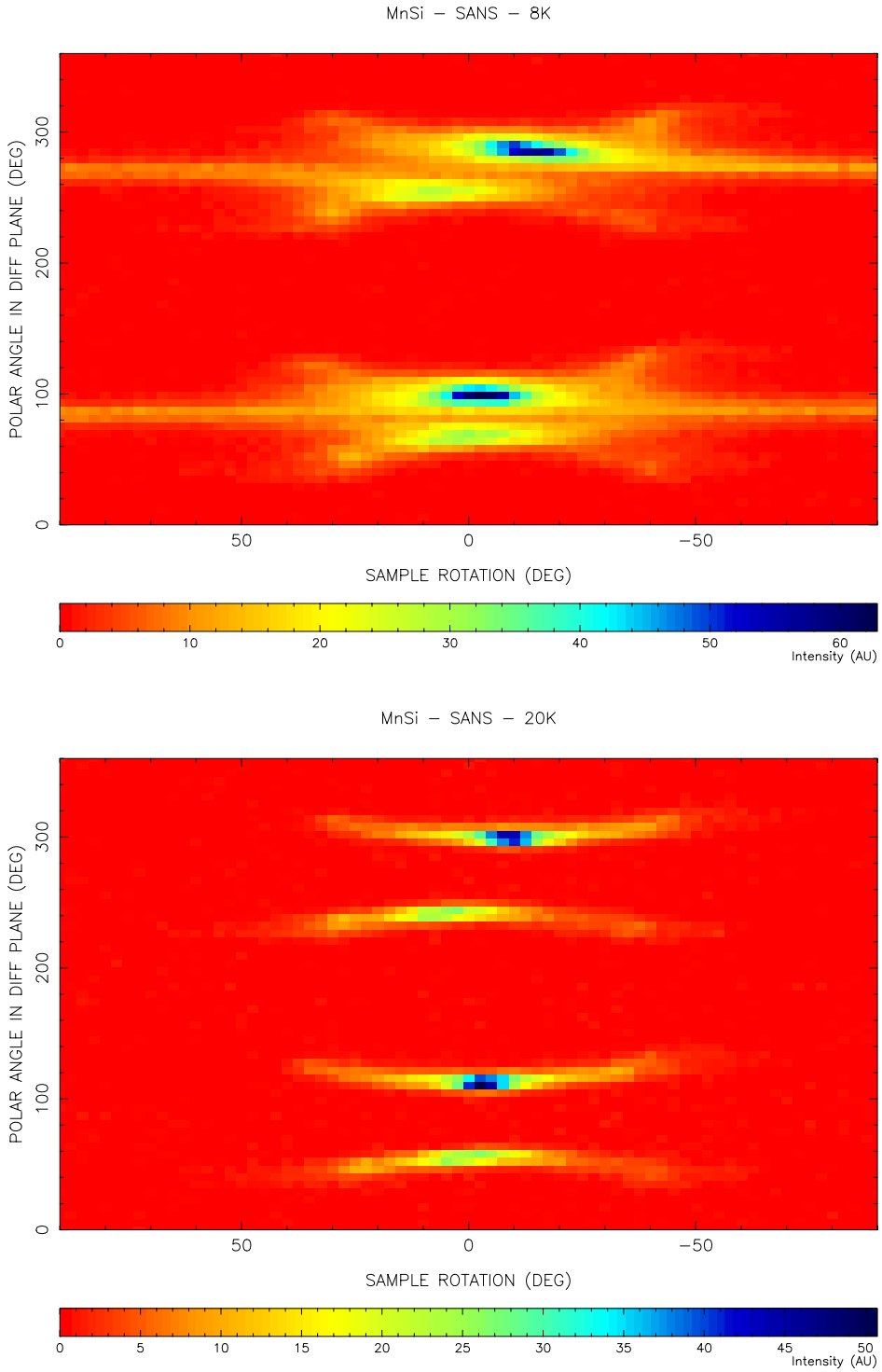

Figure 33. MnSi under 4.5 kbar pressure. The distribution of intensity as a function of sample rotation and of the direction in the diffraction plane measured from the direction in the plane perpendicular to the [001] *vertical rotation axis. The upper panel summarizes data taken at 8 K. The lower panel shows data taken at 20 K.*

where $g = 1 + \beta_x^4 + \beta_y^4 + \beta_z^4$ and β_i denotes the direction cosine of $\vec{q}$ with respect to the i-axis. The magnetization, $\vec{m}$ has been split into the components $m_{\|}$ and $m_{\perp}$ parallel and perpendicular to $\vec{q}$, respectively. θ denotes the angle between the

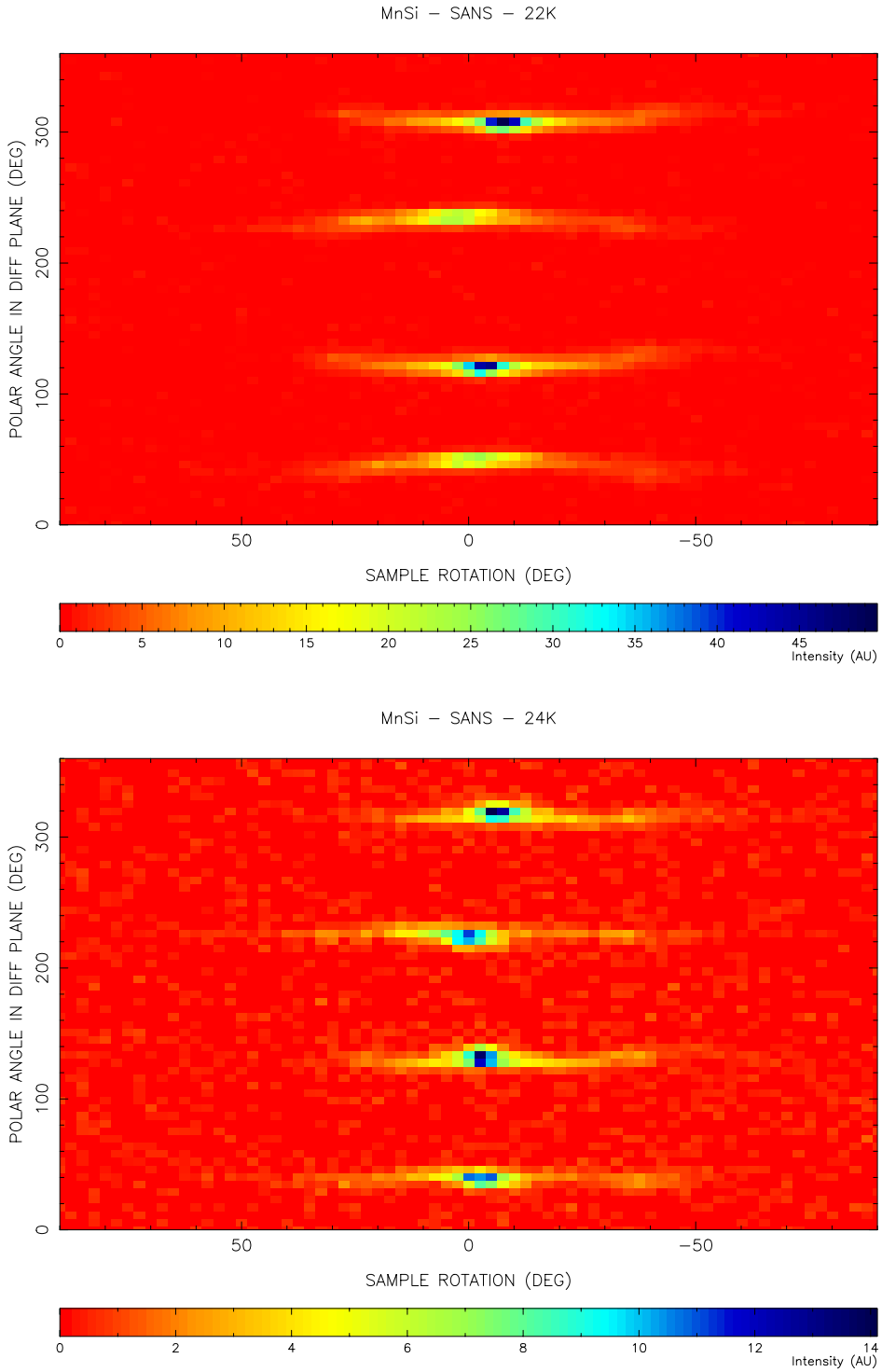

Figure 34. Mnsi under 4.5 kbar pressure. See text and caption of Fig. 33. The upper and the lower panels show data taken at 22 K and 24 K, respectively.

$\vec{q}$ and $\vec{H}$. The terms of 54 proportional to D_3 and B'' cancel due to the helical structure. Finally, by considering the case of $q \to 0$, Plummer and Walker conclude that the parameters B_1, B_2 and B_3 must be equal, and their common value is designated by B.

In the absence of an external magnetic field, the free energy is minimized with $\vec{q}$ parallel to $< 111 >$ if the coefficient of g is positive. In the case of a negative coefficient in front of g, the helix is stabilized with $\vec{q}$ along $< 100 >$. From this observation, it is concluded that both of the anisotropy parameters D and E are positive for MnSi at ambient conditions. The chirality of the magnetic helix is controlled by the sign of the coefficient C of the DM term. As shown in the phase diagram Fig. 27, a relatively small applied field (≈ 50 mT) changes the direction of $\vec{q}$ whereas it's length shows little field dependence. Hence the anisotropy terms play little role for the determination of the helix period. When neglecting D, we have:

$$|\vec{q}| \approx \frac{|C|}{2A_2} \tag{56}$$

When applying a magnetic field, a coupling between $\vec{q}$ and the field $\vec{H}$ exists through the combination of terms:

$$-\vec{m} \cdot \vec{H} + B' m_\perp^2 S^2$$

If $B' > 0$, the free energy is minimized by having $\vec{q}$ parallel to the magnetization, $\vec{m}$ and hence parallel to the field. The competition between these terms with the other anisotropy terms leads to the gradual rotation of $\vec{q}$ towards the field upon increasing the field.

As already mentioned, the observation of the rotation of $\vec{q}$ towards the [101]-direction when pressure is applied cannot be accounted for within the theoretical framework described above. When the cubic symmetry is maintained, there is no mechanism in favor of $\vec{q}$ parallel to a $< 110 >$-direction. Furthermore, we have observed a selection of a single domain which is not consistent with the cubic symmetry. This leads to the supposition that the sample crystal is subject to some uniaxial stress. As the pressure cell is cooled down, the pressure transmitting fluid, FC-75 eventually freezes[2]. In this process, one could imagine a breakdown of the hydrostatic pressure. Furthermore, it has been suggested [4] that imperfections in the crystal may lead to a inhomogeneous deformation even in a hydrostatic pressure.

The elastic perturbation of the crystal structure is characterized by the strain tensor elements ϵ_{ij}, $i, j = x, y, z$, where

$$\epsilon_{ij} = \frac{1}{2}\left(\frac{\partial u_i}{\partial r_j} + \frac{\partial u_j}{\partial r_i}\right) \tag{57}$$

with $\vec{u}(\vec{r})$ being the displacement field. Following the formulation of Callen and Callen [10], the Cartesian strain tensor is transformed to the irreducible strain tensor elements:

$$\begin{aligned}
\epsilon^\alpha &= \epsilon_{xx} + \epsilon_{yy} + \epsilon_{zz} \\
\epsilon_1^\gamma &= \sqrt{5}\left(\epsilon_{yy} - \frac{1}{2}(\epsilon_{xx} + \epsilon_{zz})\right) \\
\epsilon_2^\gamma &= \frac{1}{2}\sqrt{15}\,(\epsilon_{xx} - \epsilon_{zz}) \\
\epsilon_1^\epsilon &= \epsilon_{yz} \\
\epsilon_2^\epsilon &= \epsilon_{zx} \\
\epsilon_3^\epsilon &= \epsilon_{xy}
\end{aligned} \tag{58}$$

[2] A phase diagram for FC-75 at cryogenic temperatures was requested from the Danish branch of 3M. According to the company no such data has been published.

These tensor elements transform according to irreducible representations of the crystal point group, T. If only the α-strain is non-zero, the deformation conserves the cubic symmetry of the unit cell. Adding a single non-zero γ-strain changes the lattice parameter along a single cube axis but all cell angles remain 90°. Hence, a single γ-strain corresponds to a tetragonal distortion of the cell. When adding the second γ-strain, the cell is still rectangular, but the three axes become non-equivalent; the distortion is ortorhombic. The ϵ-strains (note, that here, the ϵ is the superscript ϵ of ϵ_i^ϵ referring to the three dimensional irreducible representation Γ_ϵ) represent deformations of the structure that change the cell angles. Based on the apparent symmetry of the magnetic diffraction patterns, we shall here neglect the ϵ-strains and concentrate on the effects of the γ-strains. We seek terms in first order of the strain elements and in second and fourth order of the spin density components. The appropriate combinations of spin density components are readily identified by simply noting that in a perturbation term, the spin density part must transform in the same way as the strain element under symmetry operations. Since the spherical harmonics Y_l^m for fixed l are homogeneous polynomials of the Cartesian coordinates of order l, and since they form a basis of a $2l+1$-dimensional irreducible representation of the full rotation group, getting the perturbation F' of the free energy is straight forward:

$$F' = B_2^\gamma \sum_{i=1}^{2} \epsilon_i^\gamma K_i^{\gamma,2}(\vec{S}) + B_4^\gamma \sum_{i=1}^{2} \epsilon_i^\gamma K_i^{\gamma,4}(\vec{S}) \tag{59}$$

where the Kubic harmonics [10] $K_i^{\gamma,j}$ are given by:

$$\begin{aligned}
K_1^{\gamma,2}(\vec{S}) &= \sqrt{5}\left(|S_y|^2 - \frac{1}{2}(|S_x|^2 + |S_z|^2)\right) \\
K_2^{\gamma,2}(\vec{S}) &= \frac{\sqrt{15}}{2}\left(|S_x|^2 - |S_z|^2\right) \\
K_1^{\gamma,4}(\vec{S}) &= 7\frac{\sqrt{15}}{2}\left(|S_y|^4 - \frac{1}{2}(|S_x|^4 - |S_z|^4) - \frac{6}{7}|S|^2 K_1^{\gamma,2}(\vec{S})\right) \\
K_2^{\gamma,4}(\vec{S}) &= 21\frac{\sqrt{5}}{4}\left((|S_x|^4 - |S_z|^4) - \frac{6}{7}|S|^2 K_2^{\gamma,2}(\vec{S})\right)
\end{aligned} \tag{60}$$

and the symbols B_i^γ designates magneto-elastic coupling parameters. In addition, a fourth order perturbation of the order q^2S^2 should be included. Keeping the simplification $D = D_1 = D_2$ of equation (54) makes the structure of the q^2S^2 perturbation equivalent to that of the S^4-term stated in equation (59). With the above used choice of coordinate axes, a γ_1-strain could favorize spin density along [010] and $\vec{q}$ in the [100]-[001]-plane. The appearance of the effect in both second and fourth order terms is consistent with the observation that $\vec{q}$ stays in the [100]-[001] plane throughout the whole temperature range covered in the experiment. In order to explain the rotation of $\vec{q}$ towards [001] at low temperatures, a γ_2-strain needs to be present. This strain introduces asymmetry in the [100]-[001] in both second and fourth order terms. If the sum of the two terms of the form $\epsilon_2^\gamma|S|^2$ nearly cancels, the modulation vector is found close to the [101]-direction at temperatures close to T_N where terms in S^4 are negligible. If further the term in $\epsilon_2^\gamma|S|^4$ is appreciable compared to DS^4, a rotation towards [001] may appear as T decreases and S increases. The flip of $\vec{q}$ from $< 100 >$ to $< 111 >$ observed in FeGe has been explained in a similar way by Plummer [45]. It should be noted, that part of the anisotropy could be introduced by the magnetic ordering itself. As a further possibility, a strain could change the magnetic structure to break the assumption of a simple helix. Diffraction patterns were recorded in rotation series at a few temperatures to look for higher order satellites signalizing a perturbation

of the helix, but no such satellites was observed. As we do not know the precise character of the strain and since we have no way of determining the coupling parameters in the perturbation terms, we retain from a further discussion of strain effects. However, it should be noted, that in numerical calculations of the free energy including a γ_1-strain in S^2 and S^4 and a γ_2-strain in S^4, a flattening of the minimum as a function of the direction of $\vec{q}$ is seen. With a certain (arbitrary) choice of parameters, the shape of the minimum resembles the arced shape of the intensity distributions seen in the experiment (Fig. 33 and 34).

Although we do not have a quantitative modeling of the rotation of $\vec{q}$, we have strong indications that the results of the high pressure study are dominated by the effects of an inhomogeneous deformation of the crystal. As the main conclusion on the experiment, we are left with the ascertainment that perturbations of the crystal lattice have a strong effect on the orientation of the modulation vector. As a final remark, we note that in measurements of longitudinal magnetostriction in MnSi published by Fawcett *et al.*, the phase pocket discussed by Ishikawa *et al.* [25], Lebech [34] and Harris [22] is clearly seen as an anomaly. This indicates the importance of interaction between the crystalline and the magnetic structure to the observed reorientation of $\vec{q}$ in the pocket. If the effect of the applied field leads to a γ-strain along the field direction sufficiently large to reverse the sign of the anisotropy parameters for the plane normal to the field and to make the strength of the anisotropy exceed the coupling to the field, this could result in the reorientation. As the field is increased, the modulation vector eventually realigns with the field.

To further investigate the coupling between crystalline and magnetic structure in MnSi, a number of experiments are suggested:

- A high pressure neutron scattering experiment using a He-pressure cell. Compared to the McWhan cell, the He-cell offers better certainty for a hydrostatic pressure. However, in the He-cell, the pressure is limited to 5 kbar. Thus, this cell-type would not allow a study of the microscopic magnetic structure in the vicinity of the suppression of the ordering.
- To clarify the effect of an inhomogeneous deformation of the crystal, a neutron scattering experiment under controlled application of uniaxial stress is proposed.
- To further investigate magneto-elastic couplings, a low temperature X-ray experiment is suggested.
- The coupling between lattice and magnetism in the phase pocket labeled (e) in Fig. 27 would be very interesting to study in an X-ray diffraction study. Combined with the uniaxial stress neutron scattering study, this experiment could test the suggested mechanism for the reorientation of $\vec{q}$ in the phase pocket.

13 Critical scattering studied by SANS

In the literature, several reports are found [25], [7] on a highly diffuse scattering of neutrons from MnSi at temperatures just above the Néel transition. To further

study the structure and evolution of this scattering, a small angle neutron scattering experiment was conducted at the Risø SANS instrument.

The configuration of the diffractometer was similar to the one used in the high pressure experiment except that a 10 mm pinhole was used at the sample end of the incident flight-path. The sample was a single crystal of nearly cylindric, slightly conical shape. It's diameter was approximately 5 mm and the length was about 5 cm. To obtain cryogenic conditions, a closed cycle cryostat with a base temperature of 12 K was used. This cryostat was chosen since the small angle scattering from it's vacuum shroud and radiation shield was known to be modest. An earlier attempt [22] to study the critical scattering in a cryomagnet failed due to a high intensity of background scattering at exactly the momentum transfer where the sample signal was expected. The sample was mounted in the cryostat with the [011]-direction along the vertical axis of rotation. In this orientation, the sample was inclined by approximately 35° from horizontal. To have the largest possible illuminated sample volume, the sample was translated along the horizontal [100] by about 10 mm. This means that the sample rotation axis did not intersect the beam and hence, the sample could not be rotated by more than ±25°. The sample temperature was measured by a calibrated Ge-resistor and controlled by a Risø temperature controller. By inserting thermal damping by means a 0.1 mm thick sheet of mylar between the cold tip of the cryostat and a thermometry block just above the sample, the measured temperature was stable within a few mK all the way down to the base temperature. Without the mylar foil, temperature fluctuations of up to 1 K were observed near the cryostat base.

Diffraction patterns were recorded either in rotation scans at fixed temperature (12 K, 29.2 K, 30.2 K, 30.4 K) and as temperature scans with the [100]-[011]-plane perpendicular to the incident beam. In the rotation scans, the counting time was 10 minutes per diffraction pattern except for the 12 K scan where the counting time was reduced to 1 minute per pattern. For the temperature scans, a counting time of 30 minutes per frame was chosen. In addition to the low temperature patterns, a rotation series was recorded at 40 K again using 10 minutes counting time per frame. All data have been background subtracted and corrected for detector efficiency following the same procedure as described for the pressure experiment.

Color maps of the corrected intensity distributions obtained from the data of the temperature scan with fixed orientation are shown in Fig. 35. At the 25 K map, four satellites of two domains with $\vec{q}$ along [111] and $[\overline{1}11]$, respectively are seen. The two extra peaks of intensity along the [100]-direction may originate partly from multiple scattering and partly from a coupling between the magnetic domains of the sample [29]. Since the two weaker peaks along [011] disappear upon rotation of the crystal around [011] by ±7.5°, they are ascribed to multiple scattering. In the frame recorded at 28.5 K we see an elongation of the main satellites perpendicular to the modulation vector. When warming up further, the ring shape develops and it stays visible in the maps to about 2.5 K above the Néel temperature.

To obtain the angular and radial distribution of intensity, each SANS frame has been analyzed as described in section 12 by circular and radial averaging. The radial distribution at each temperature has been fitted to a Gaussian peak shape. In Fig. 36, we summarize the results of these fits by showing the length of $\vec{q}$ and the radial width of the intensity distribution as functions of temperature. At the Néel point, the rate dq/dT is seen to increase dramatically and the width of the intensity distribution raises from the resolution limited value of 0.01 $Å^{-1}$. At 30 K,

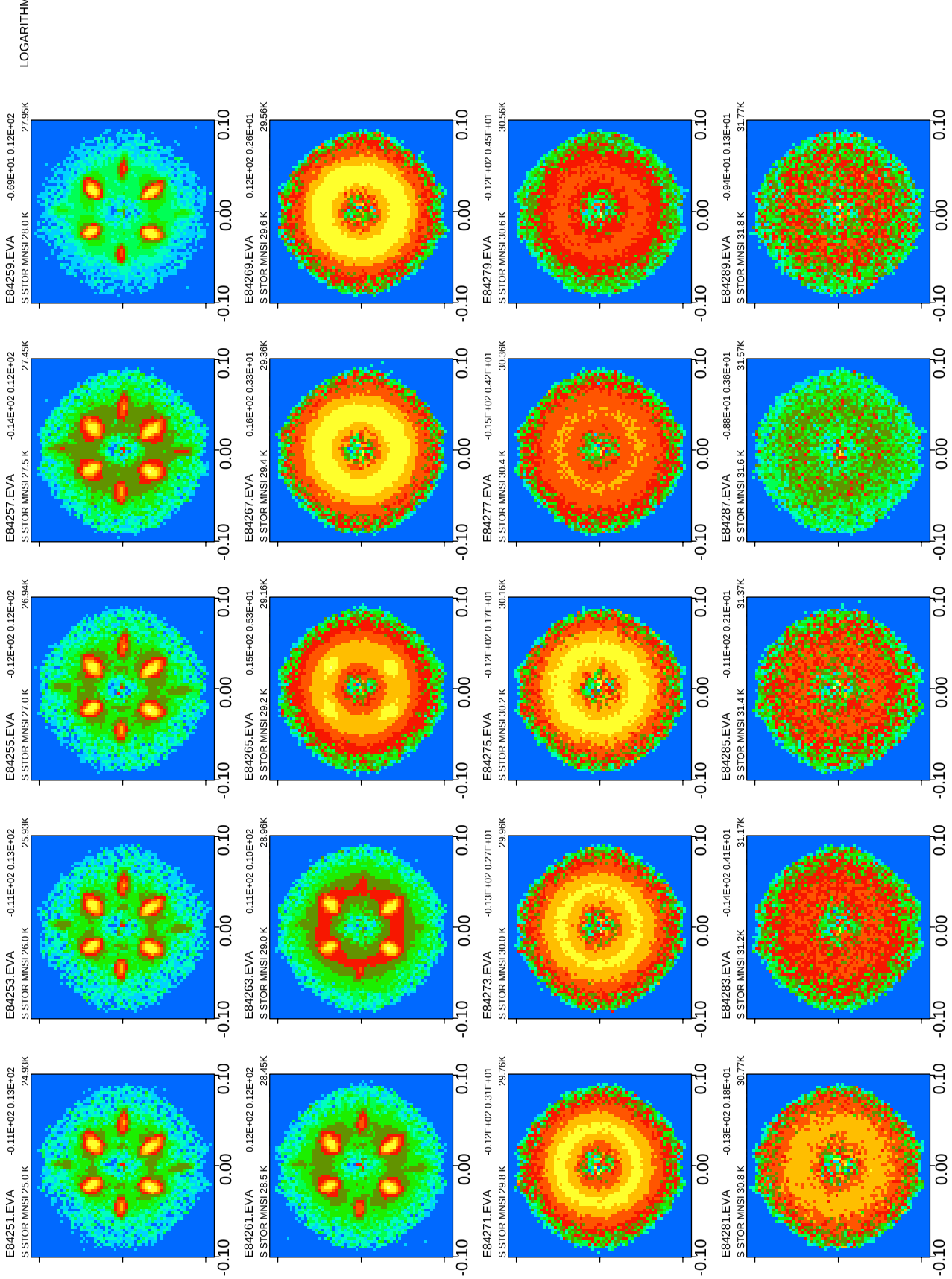

Figure 35. Corrected SANS frames recorded in the [100]-[011]*-plane at temperatures ranging from 25 K to 31.8 K. When rotating the page by 90 degrees clockwise, the* [100] *direction is along the horizontal axis of the frames and the* [011] *is along the vertical. Note, that each frame is shown on an individual logarithmic scale.*

the observed radial width is 0.025 Å^{-1}. Taking the resolution width as 0.01 Å^{-1}, a crude estimate for the correlation length along $\vec{q}$ is of the order 300 Å.

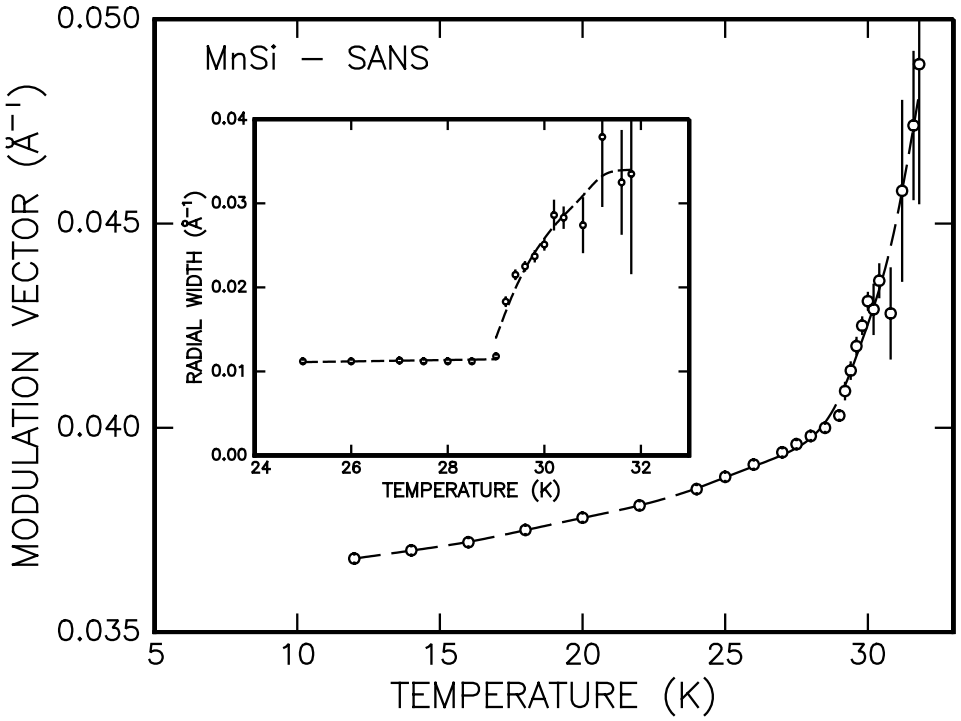

Figure 36. The length of the modulation vector $\vec{q}$ versus temperature. The inset shows the Gaussian full width of half maximum for the radial distribution of intensity. The dashed curves are guides to the eye.

The development of the angular distribution of intensity has been summarized in the color map of Fig. 37. The intensity is shown on a logarithmic scale with the temperature along the horizontal axis and the angle from the [100]-direction in the [100]-[011]-plane along the vertical. As in the color maps of the corrected SANS frames (Fig. 35), the disappearance of the main satellites and building up of the diffuse component is seen. It is noted, that at 29.2 K the diffuse scattering seems somewhat stronger in the direction of [011] than in the [100]-direction. For a full treatment of the critical scattering, one should model the sample scattering cross-section and by the resolution function formalism fit the observed diffraction patterns to the model. Recently, a program system was developed by Harris *et al.* [23] to treat single crystal diffraction data from a SANS instrument. However, to achieve reasonable computation times, the system is limited to a Gaussian model of the sample cross-section. Furthermore, this analysis system requires the recording of diffraction patterns under rotation and tilting of the sample. Since the assumption of a Gaussian cross-section is not valid in the critical regime and since full rotation and tilt scans could not be obtained within the available beam time, a more primitive analysis of the angular distribution of intensity is performed. The diffraction plane has been divided into eight angular sections corresponding to the $< 111 >$ directions containing the main satellites (four sections), the [100]-direction (two sections) and the [011]-direction (two sections). The intensity recorded in the momentum transfer range 0.020 - 0.065 Å^{-1} has been integrated for each of the three types of sections as shown in Fig. 38. In both the [100]- and the [011]-sections, a clear maximum in the (diffuse) intensity is seen at 29.2 K. At the highest temperature of 31.8 K, remnants of the diffuse scattering is still seen.

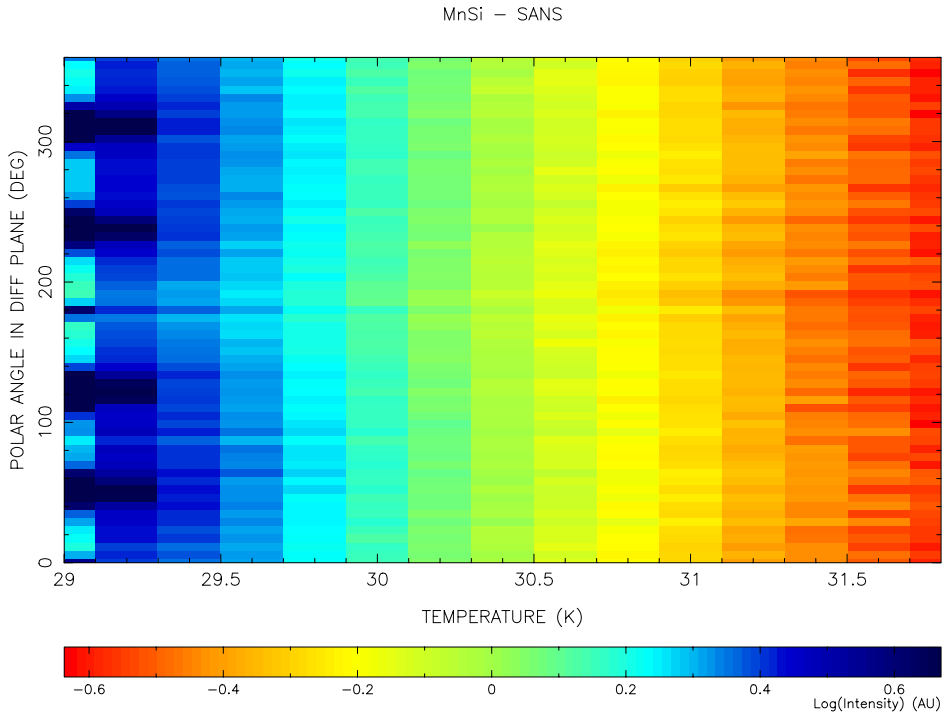

Figure 37. The angular distribution of intensity in the [100]-[011] *of MnSi as a function of temperature. The intensity is shown on a logarithmic scale.*

From the integrated intensities shown in Fig. 38, the intensity ratios $I_{[011]}/I_{[100]}$ and $I_{[011]}/I_{<111>}$ have been formed. The results are shown in Fig. 39. Below 29 K, the contamination of the [100]-sections from scattering from the two $\vec{q}$-domains outside the plane is seen. Just above 29 K, the intensity in the [011]-type sections exceeds that of the [100]-sections by approximately 15%. From about 30 K, both the intensity ratios shown are close to 1 indicating that the angular distribution of intensity within the ring is now uniform.

The ratio $I_{[011]}/I_{<111>}$ shown in Fig. 39 changes very steeply from close to 0 to close to 1 at the Néel transition. This indicates that $I_{[011]}$ is highly dominated by the critical scattering and may be used to isolate the part of $I_{<111>}$ originating from the long range order. Fig. 40 shows the difference $I_{<111>} - I_{[011]}$, i.e. the true long range component of the magnetic scattering as a function of temperature. The data in the temperature region 20.0 - 29.2 K have been fitted to a power-law model of the form $I = I_0(T_N - T)^{2\beta}$, where β is the critical exponent for the amplitude of the spin density wave. Since the performed integration of intensity and correction for the critical part of the scattering is somewhat sloppy, one could certainly question the reliability of the obtained value for β. However the found value of 0.2 is in complete agreement with the result of Hansen [21] quoted by Harris [22]. The power-law fit was performed with a fixed Néel temperature of 29.2 K.

The SANS frames recorded in rotation scans have been analyzed to extract the radial distribution of intensity. At 30.2 K, no significant change is seen in the distribution as the sample is rotated. Hence, it may be concluded that above 30 K, the scattered intensity is independent on the direction of the the momentum transfer. At these temperatures, the distribution of scattered intensity takes the form of a spherical shell. The spin correlations above T_N must be of such a character

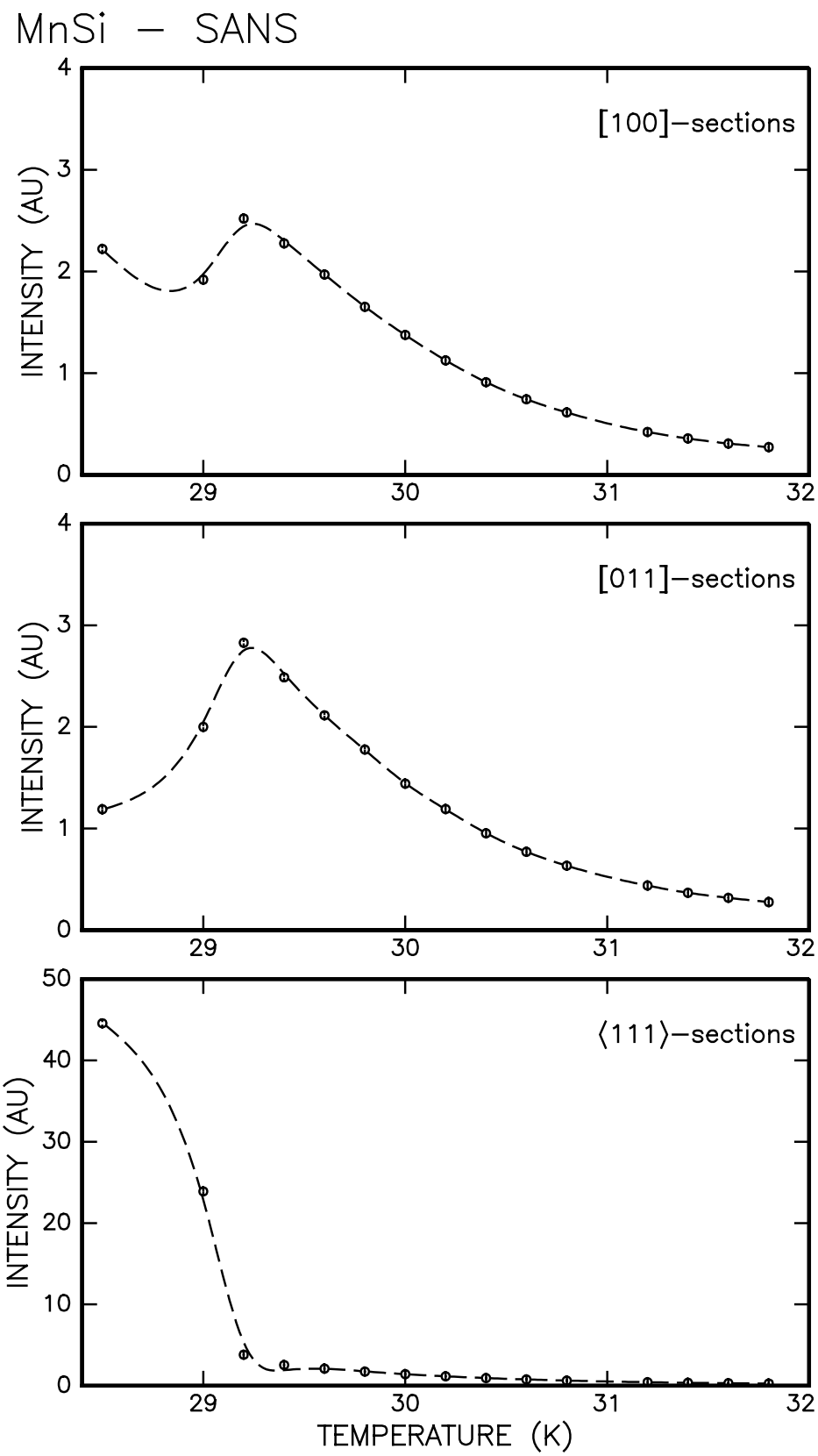

Figure 38. The intensity of neutron scattering from MnSi in the [100]-[011]*-plane integrated in angular sections around the* [100]*-direction (upper panel), the* [011]*-direction (middle panel) and the two* $< 111 >$*-directions in the plane (lower panel). The dashed curves are guides to the eye.*

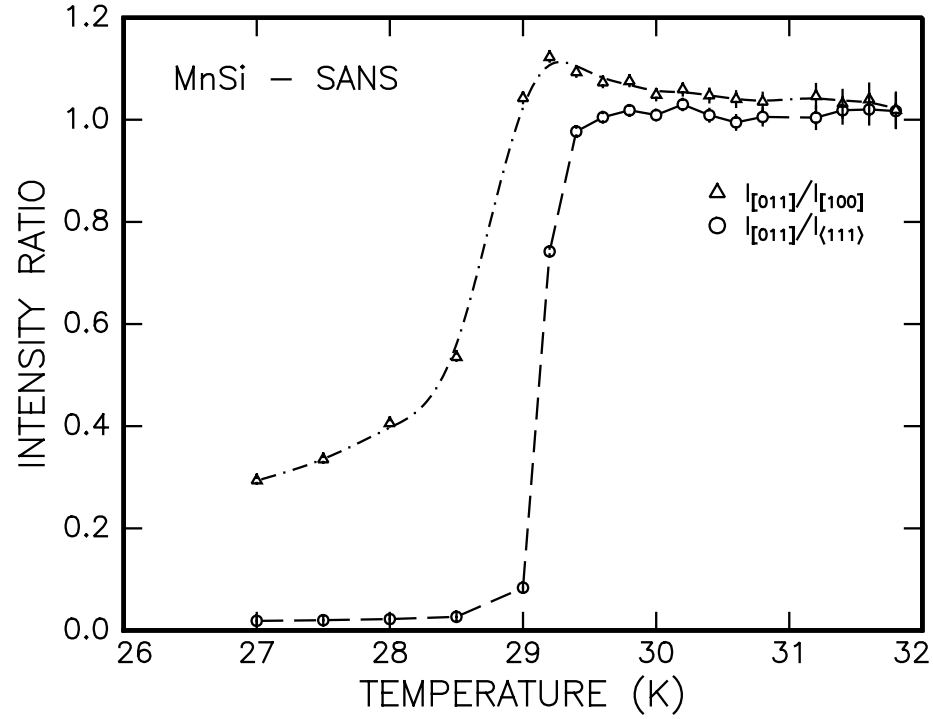

Figure 39. The ratio between intensity integrated in the three different types of angular sections as a function of temperature. The dashed curves are guides to the eye.

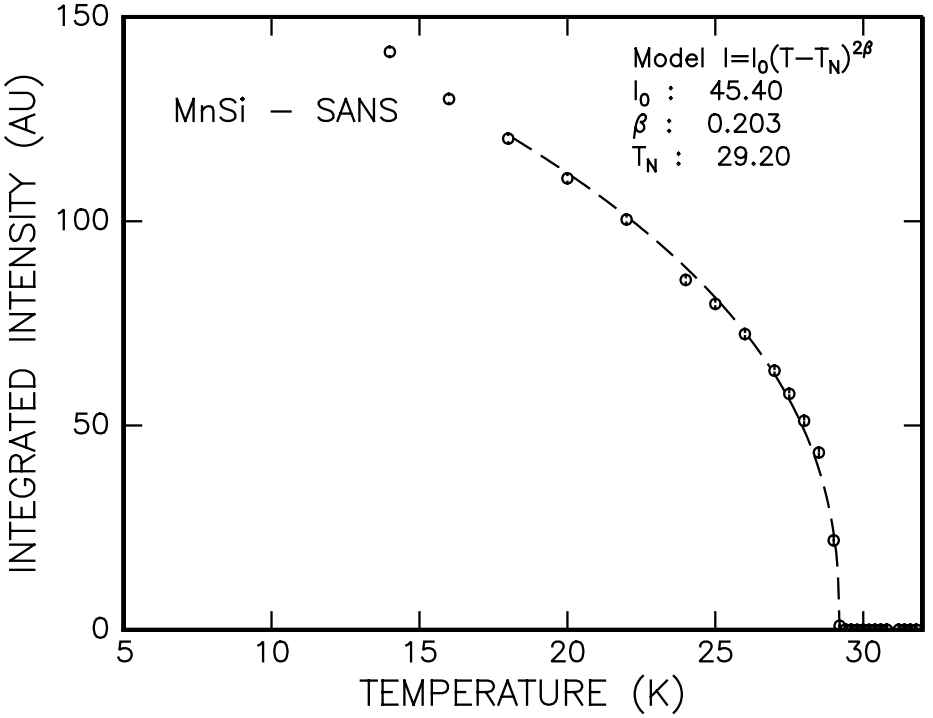

Figure 40. The scattered intensity in the $< 111 >$-type angular sections corrected for the critical contribution by subtraction of $I_{[011]}$. The dashed curve is the result of a power-law fit in the temperature region 20 - 29.2 K.

that a local modulation vector exists of a length comparable to what is found in the ordered state but with a random orientation. This appears consistent with the approximate mutual independence of those terms in the free energy expansion (54) determining $|\vec{q}|$ and those controlling the direction of the helix.

14 A polarization device for SANS

Since the lack of inversion symmetry in the crystal symmetry plays such an important role in the theoretical models of the magnetic structure in MnSi, a study of the relationship between the chirality of the chemical cell and that of the magnet helix is interesting for testing the theory. As discussed in the introduction of this report, the chirality of a helical magnetic structure may be determined in a measurement of the neutron scattering cross-section using a polarized incident beam.

The theoretical prediction of a one to one correspondence between the structural and magnetic chiralities was confirmed in an experiment by Ishida and coworkers [24] in 1985. For this study, a white beam of neutrons was reflected from a curved polarizing mirror, taken through a spin flipper device and scattered from the MnSi single crystal. The scattered beam was analyzed using a pair of time-of-flight detectors positioned to measure the intensity of a $+\vec{q}$ and a $-\vec{q}$ magnetic satellite, respectively. The experiment excellently solves the physical problem of determining the chirality. However, for general investigation of long period magnetic structures, SANS with an area detector is far more efficient than a single or double detector technique, and the development of a polarization device for SANS would be highly desirable. In this section, a new multi-layer based polarization device for SANS manufactured by P. Høghøj of the Institut Laue Langevin Instrumentation Branch and implemented at Risø by P. Høghøj, M. Gerstenberg and the author is described.

In addition to the requirements meat by polarization devices for traditional double and triple axis experiments, a polarizer for SANS must have a large wave-length acceptance. Since the source intensity of the long wavelength neutrons applied for SANS is often weak, one may use a bandwidth of 20%. To limit the total loss in the instrument, it was decided to design the polarizer with a defined band width to have a polarizing band-pass filter rather than separate devices for polarization and monochromatization.

As shown in Fig. 41, the polarization device is a stacking of 0.5 mm thick Si wafers with an Fe-Si multi-layer sputtered on each side. The Si-wafers work as miniature neutron guides since neutrons of the incident beam with the desired polarization state undergoes a Bragg reflection on each of the multi-layer covered sides of the wafer. Those neutrons not reflected from the multi-layers are absorbed in a Gd-layer on the outside of the wafer. Since the desired neutrons are reflected twice, the exit beam is parallel to the incident beam but shifted by approximately 1 mm. During the sputtering process, the d-spacing of the multi-layers were modulated to obtain a bandwidth of 20%. Instead of using one long wafer to cover a 10 mm wide beam, the covered fields of the individual wafers in the stack were made contiguous by matching the length of the wafers against their thickness and the scattering angle. Since the polarizing function of the multi-layers is due to the magnetic scattering from the Fe, the multi-layers were magnetized in a yoke mount with a field of 0.1 T. In addition to the band-pass filter effect and the parallel incident and exit beams, it is a major advantage of the device that the polarizing effect may be turned on and off simply by rotating the wafers between a orientation letting the beam straight through and the orientation for Bragg reflection.

The beam polarization obtained with the device was measured at the Risø SANS instrument using a second polarizer. The beam polarizer was mounted in a yoke

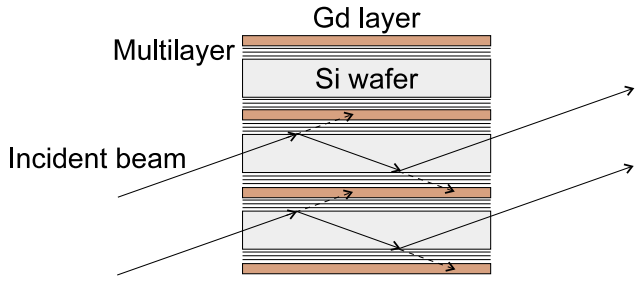

Figure 41. The principle of the SANS polarization device.

on a turn-table just after the exit pinhole of the incident flight path, The second polarizer was mounted on the sample table. To maintain the neutron polarization at the flight-path between the two polarizers, a weak guide field was established by fitting stacks of permanent magnets between iron plates. To allow rotation of the neutron polarization, a Mezei-flipper was also installed in the polarizer to polarizer flight path. After optimizing the guide fields and the currents in the two coils of the flipper, a flipping ratio of 20 was obtained. The transmission of neutrons with the desired spin state was about 50%.

In order to demonstrate the potential of using a polarized incident beam on a SANS instrument with an area detector, the shell of magnetic critical scattering from MnSi discussed in the previous section was measured with the multi-layer polarizer in the beam. The experimental conditions were similar to those described in section 13 except for the polarization. The multi-layer device in the yoke was placed behind the exit pinhole of the collimation section as in the reference experiment described above. The guide field sections and the Mezei-flipper were placed between the polarizer and the sample cryostat. A set of coils were fitted on the outside of the cryostat to obtain a weak guide field at the sample position. The diffraction pattern from the sample was measured at 30.0 K and at 50.0 K with the neutron spin parallel and anti-parallel to the vertical [110]-direction of the sample. The diffraction patterns recorded at 50.0 K were used for background subtraction of the 30.0 K data and the normalizations with respect to beam monitor and detector efficiency were applied as described in sections 12 and 13.

From equation (19), we readily get the dependence of the scattered intensity upon the angle between the scattering vector and the polarization. In the SANS geometry used, the scattering vector, $\vec{\kappa}$ is parallel or anti-parallel to the modulation vector $\vec{q}$. By further assuming that at 30.0 K, the local correlations in the spin density takes the simple helical form, we have the cross product term $\imath(\tilde{A}_{\vec{r}} \times \tilde{A}_{\vec{r}'})$ of equation (19) being proportional to $\vec{q}$. Hence, the intensity takes the form

$$I \propto 1 - \delta P_0 \hat{z} \cdot \hat{\kappa} \tag{61}$$

Keeping the notation of the introduction, P_0 denotes the incident polarization, $\hat{z}$ is a unit vector along the direction of polarization and $\hat{\kappa}$ is a unit vector along the momentum transfer. Finally, δ is the difference in relative occupancy in the sample of the two magnetic chirality domains. Thus, if the sample cross-section is independent of the direction of $\vec{\kappa}$, we expect the intensity to vary as cosine to the angle, ϕ between scattering vector and polarization. In Fig. 42, the intensity measured in the [100]-[011]-plane of MnSi at 30.0 K is shown as a function of the angle between $\vec{\kappa}$ and [100]. The open circles represent the data obtained without flipping the incident spin, whereas the triangles represents data taken with the Mezei-flipper on. The dashed curves are the results of fitting the data to the func-

tion $a+b\cos(90°-\phi)$ with a and b as fitted parameters. The ratio b/a between the to model parameters of the fit represents the product δP_0. Assuming the incident polarization of 90% (the flipping ratio of 20 for the polarizer) gives 95% occupation of the dominant chirality domain of the crystal. It should be noted, that since the counting time is only 10 minutes per diffraction pattern, the statistics of the data shown in Fig. 42 is poor. The uncertainty of the majority domain population stated above is indeed of the order 0.05.

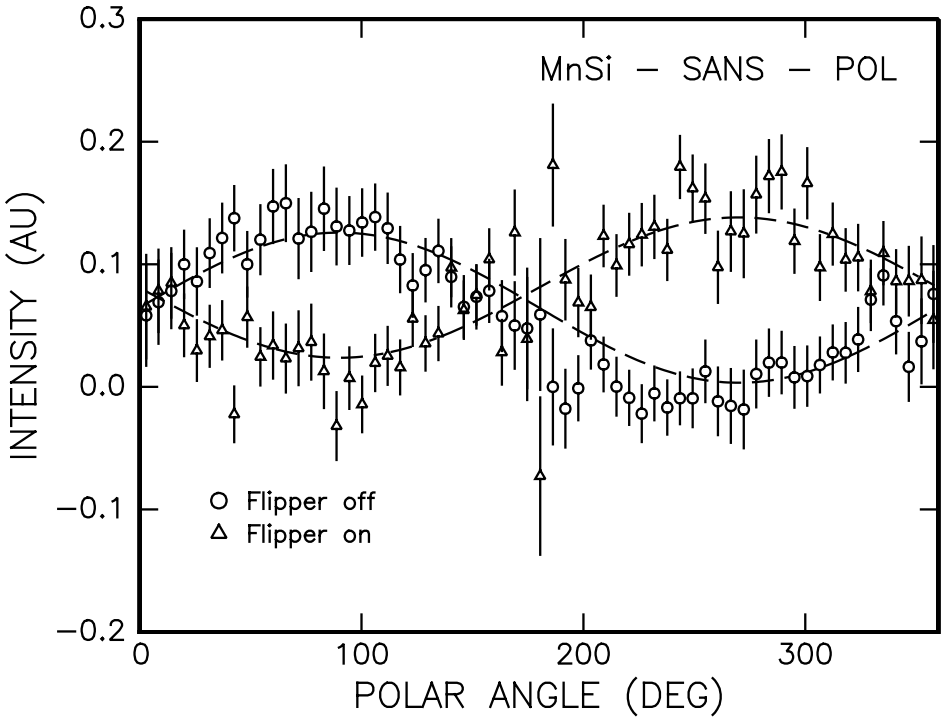

Figure 42. The intensity of the magnetic critical scattering from MnSi at 30.0 K with incident neutron polarization parallel to [011] *(90° polar angle) and anti parallel to* [011] *(270° polar angle). The dashed curves are the results of fitting the data to a sine-function. See text for more details.*

In the experiment by Ishida and coworker [24], occupancies of the majority domain of 98 - 99% were obtained. Apart from the poor statistics of the data presented here, the guide field established for the present SANS experiment was provisional, and it was necessary to move the guide field sections in order to mount the cryostat. Hence, the optimization of flipper and guide field sections obtained during the reference measurement with two polarizers could not be retained for the measurements with the MnSi sample. Thus, the incident polarization might well be significantly lower than obtained in our reference measurement. Solving the problems of guide fields and reducing the background are simple technical tasks, and the results presented here certainly proves the potential of the polarization device. Separation of spin-flip from non spin-flip scattering would by highly interesting not only to studies of magnetic systems but also to more traditional macro molecular applications of SANS. However, such separation is only possible if polarization analysis is applied to the scattered neutrons. For a SANS instrument, a polarization analyzer with an extreme angular acceptance (at least $\pm 5°$) is needed, and this requirement is currently only meat by pumped ^{3}He filter devices.

Part IV
Conclusion

The two magnetic systems $DyFe_4Al_8$ and MnSi have been studied by neutron scattering and in the former case also by X-ray resonant magnetic scattering. In the following, the main results are summarized.

In $DyFe_4Al_8$ ordering of the Fe sublattice has been found at temperatures below 180 K. By comparing the intensities of the magnetic satellites observed by neutron scattering with the momentum transfer parallel and perpendicular to the modulation vector, a cycloidal structure with the spins in the basal plane of the *bct* crystal structure is suggested. Assuming this structure, the value of 1.5 μ_B was obtained for the ordered magnetic moment at the Fe-sites. At temperatures below 25 K ordering of the Dy sublattice is signalized by a second set of magnetic satellites in the neutron diffraction pattern. Below 15 K satellites of 3'rd and 5'th order show up in the diffraction patterns. Integrated satellite intensities observed around four reciprocal lattice points was compared to test an assumption of a basal plane cycloidal model for the Dy structure. The result of this analysis could neither confirm nor rule out the cycloidal model for the Dy. When the cycloidal structure is assumed for the Dy, the ordered magnetic moment for this element is estimated as 5.5 μ_B.

The resonant magnetic X-ray scattering at the Dy L_{III}-edge was measured in two different crystal orientations (the basal plane of the crystal parallel and perpendicular to the scattering plane) at temperatures down to 12 K. The dependency of the scattered intensity upon the diffraction angle observed in the two orientations strongly supports the basal plane cycloidal structure of Dy. At temperatures above the ordering of Dy, a residual resonant X-ray signal shows the polarization of Dy 5*d*-electrons due to the Fe ordering. The temperature dependency of the length of the modulation vector was measured with both X-rays and neutrons. In the X-ray case, the modulation vector shows a lock-in to $(\frac{2}{15}\frac{2}{15}0)$ at around 100 K. When measured by neutron scattering, the length of the modulation vector varies down to temperatures of 15 - 20 K. An explanation to this discrepancy has not been found.

The effect of a magnetic field applied along a $< 110 >$-direction was investigated by neutron scattering. A field of less than 1 T is sufficient to quench the modulation of the Dy-moments while magnetic satellites originating from the Fe-sites are still observed at 5 T. Due to large extinction corrections, the magnetization induced by the field is difficult to estimate. Using a crude correction for extinction effects yields a Dy-moment of 8 μ_B at fields above 1 T. In zero field, an increase in the intensity of both the (110) and (220) peaks is observed upon cooling. Since the effects depends strongly on neutron wavelength, it was ascribed to release of extinction.

At temperatures below $\approx$ 12 K, diffuse scattering builds up around the nuclear peaks. In the longitudinal direction, this diffuse component is observed all over the Brillouin zone. In the transverse direction, the width of the scattering is resolution limited.

A simple model of $DyFe_4Al_8$ was constructed by assuming a fixed cycloidal magnetic structure of the Fe sublattice and simple nearest neighbor Heisenberg coupling between the Fe and Dy moments. The model was not able to explain

the observed intensities of higher order harmonics. However, a number of enhancements of both the model and the method of determination of the model parameters are suggested for future work.

The intermetallic compound MnSi belongs to a family of itinerant magnetic systems with very long period (up to 2000 Å) modulated magnetic structures and the cubic crystal structure $P2_13$. In MnSi, a helical spin density wave with modulation vector, $\vec{q}$ along $< 111 >$ and a period of 180 Å is known to exist at temperatures below 29 K. The effect of a 4.5 kbar applied hydrostatic pressure on the magnetic structure was investigated by small angle neutron scattering (SANS). The main effects of the pressure are a decrease of the Néel temperature to 25 K and a rotation of the modulation vector in the [100]-[001]-plane from a direction close to [110] at T_N to a direction close to [001] at 8 K. This behavior is not explained by the current theory of the magnetism of MnSi if the cubic symmetry is maintained. A further lack of equivalence in the diffraction patterns between symmetry related directions indicates an anisotropic deformation of the sample. Including an ortorhombic distortion in the theoretical model, may provide an explanation of the observed rotation of the modulation vector. However, the experiment does not provide data to quantitatively model the strain effects and a series of additional experiments is suggested.

An isotropic magnetic critical scattering from MnSi has previously been reported in the literature. In the present work, the development of the critical scattering has been studied by SANS in greater detail than hitherto published. The diffraction patterns recorded in the [100]-[011]-plane were analyzed by integrating the intensity in radial sections around the two $< 111 >$-directions, around [100] and around [011]. When warming up, the critical scattering develops from an elongation of the main satellites in the direction perpendicular to the $\vec{q}$ seen at 28.5 K. At 29 K, the scattering around [011] is 15% stronger than the scattering around [100]. Above 30 K, the observed scattering is independent on the direction of the momentum transfer, and the intensity distribution takes the form of a spherical shell. At 29.2 K, the width of the radial distribution of intensity shows a steep increase from a resolution limited level. At 30 K, the radial width is 0.025Å^{-1} corresponding to a correlation length along $\vec{q}$ of some 300Å. The sharp component of the scattering resulting from the long range order below T_N was analyzed resulting in a Néel temperature of 29.2 K and a value of 0.2 for the critical exponent β of the amplitude of the spin density wave.

Finally, the critical magnetic scattering from MnSi at 30.0 K was used to demonstrate the potential of a novel multi-layer polarization device for SANS implemented at Risø. The results clearly shows the function of the device although significant work to improve the performance remains.

Acknowledgments

Much of the work presented in this thesis is the result of collaboration. I am grateful to all those colleagues and friends who shared their knowledge and ideas with me and supported my work.

My Ph.D.-project was initiated under the supervision of Allan R. Mackintosh, University of Copenhagen and Bente Lebech, Risø. Allan took a very active part in the project, and I had great benefit from his outstanding abilities as a scientific

coach, from his enormous knowledge in the field of magnetism in metals and from his never failing enthusiasm. When Allan was killed in a tragic car accident in December 1995, all of us who had the privilege to work with him suffered a terrible loss. Throughout the project, Bente had the daily toil of teaching me the trade of neutron scattering in particular and experimental physics in general. I am truly grateful for all her efforts, her support and her personal involvement in all my ups and downs during the project. In particular, I would like to emphasize Bente's way of combining the role of the teacher and that of the colleague. Although she definitely taught me many lessons, I was never put in the position of the inferior student.

Many people showed interest in my work and kept pressing me to write up the last part of the thesis after leaving Risø for an industrial career. Of those, Morten Jagd Christensen was definitely the most mean and persistent. Apart from keeping my conscience bad, he also prepared a number of the figures found in the report.

Bente Lebech and Morten Jagd Christensen did me the great favor of reading the manuscript. I am grateful for their effort and all their comments and suggestions.

Finally, I would like to thank Jens Lebech, Morits Lund, Bjarne Breiting, Finn Saxild and Keld Theodor of the technical crew of the neutron house at Risø. All of them spent lots of time in the preparation of the high pressure and low temperature experiments.

References

[1] G. E. Bacon. *Neutron Diffraction*. Oxford University Press, Oxford, UK, 1975.

[2] P. Bak and M. Høgh Jensen. Theory of helical magnetic structures and phase transitions in MnSi and FeGe. *J. Phys. C : Solid State Phys*, 13:L881, 1980.

[3] J. Baruchel, J. L. Hodeau, M. S. Lehmann, J. R. Regnard, and C. Schlenker, editors. *Neutron and Synchrotron Radiation for Condensed Matter Studies*. Springer Verlag and Les Editions de Physic, Berlin, Germany / Les Ulis, France, 1993.

[4] N. R. Bernhoeft. Private communication.

[5] D. Bloch, J. Voiron, V. Jaccarino, and J. H. Wernick. The high field — high pressure magnetic properties of MnSi. *Phys. Lett.*, 51A:259, 1975.

[6] B. Borén. Röntgenuntersuchung der Legierungen von Silicium mit Chrom, Mangan, Kobalt und Nickel. *Arkiv för kemi, mineralogi och geologi*, 11A:1, 1933.

[7] S. A. Brown. PhD thesis, Cavendish Laboratory, Cambridge, UK, 1990.

[8] K. H. J. Buschow and A. M. van der Kraan. Magnetic ordering in ternary rare earth iron aluminium compounds RFe_4Al_8. *J. Phys. F : Metal Phys.*, 8:921, 1978.

[9] K. H. J. Buschow, J. H. N. van Vucht, and W. W. van den Hoogenhof. Note on the crystal structure of the ternary rare earth-3d transition metal compounds of the type RT_4Al_8. *J. Less Comm. Met.*, 50:145, 1976.

[10] E. Callen and H. Callen. Static magnetoelastic coupling in cubic crystals. *Phys. Rev.*, A139:455, 1963.

[11] F. de Bergevin and M. Brunel. *Phys. Lett.*, 39A:141, 1972.

[12] D. L. Decker, W. A. Bassett, L. Merril, H. T. Hall, and J. D. Barnett. High-pressure calibration, a critical review. *J. Phys. Chem. Data*, 1:773, 1972.

[13] The website of the european synchrotron radiation facility. URL : http://www.esrf.fr.

[14] I. Felner and I Norwik. Crystal structure, magnetic properties and hyperfine interactions in RFe_4Al_8 (R = rare earth) systems. *J. Phys. Chem. Solids*, 39:951, 1978.

[15] J. Gal, I. Yaar, E. Arbaboff, H Etedgi, F. J. Litterst, K. Aggarwal, J. A. Pereda, G. M. Kalvius, G. Will, and W. Schäfer. $HoFe_4Al_8$: An unusual spin glass. *Phys Rev. B*, 40:745, 1989.

[16] D. Gibbs, D. R. Harshmann, E. D. Isaacs, D. B. McWhan, D. Mills, and C. Vettier. Polarization and resonance properties of magnetic x-ray scattering in Holmium. *Phys. Rev. Lett.*, 61:5663, 1988.

[17] Michel Goossens and Fred James. Minuit function minimization and error analysis, reference manual. CERN Program Library Long Writeup D506, CERN, Geneva, Switzerland, 1992. Version 92.1.

[18] P. C. M. Gubbens, A. M. van der Kraan, and K.. H. J. Buschow. Investigations of $TmFe_4Al_8$ and $DyFe_4Al_8$ by means of ^{169}Tm and ^{161}Dy Mössbauer spectroscopy. *J. Magn. Magn. Mat.*, 61-64:61, 1982.

[19] Theo Hahn, editor. *International Tables for Crystallography*. Kluwer Academic Press, Dordrecht, 1992.

[20] O. Halpern and M. R. Johnson. *Phys. Rev.*, 55:898, 1939.

[21] P. A. Hansen. *Magnetic Anisotropy and Related Matters Studied by Neutron Scattering*. PhD thesis, Risø National Laboratory, Dk-4000 Roskilde, Denmark., 1977.

[22] P. Harris. *Neutron and X-ray diffraction from modulated structures*. PhD thesis, Risø National Laboratory, Dk-4000 Roskilde, Denmark., 1994.

[23] P. Harris, B. Lebech, and J. Skov Pedersen. The three-dimensional resolution function for small-angle scattering and laue geometries. *J. Appl. Cryst.*, 28:209, 1995.

[24] M. Ishida, Y. Endoh, S. Mitsuda, Y. Ishikawa, and M. Tanaka. Crystal chirality and helicity of the helical spin density wave in MnSi. II. Polarized neutron diffraction. *J. Phys. Soc. Jpn.*, 54:2975, 1985.

[25] Y. Ishikawa and M. Arai. Magnetic phase diagram of MnSi near critical temperature studied by neutron small angle scattering. *J. Phys. Soc. Jpn.*, 53:2726, 1984.

[26] Y. Ishikawa, Y. Noda, C. Fincher, and G. Shirane. Low-energy paramagnetic spin fluctuations in the weak itinerant ferromagnet MnSi. *Phys. Rev. B*, 25:254, 1982.

[27] Y. Ishikawa, Y. Noda, Y. J. Uemura, C. F. Majkrzak, and G. Shirane. Paramagnetic spin fluctuations in the weak itinerant-electron ferromagnet MnSi. *Phys. Rev. B*, 31:5884, 1985.

[28] Y. Ishikawa, G. Shirane, J. A. Tarwin, and M. Koghi. Magnetic excitations in the weak itinerant ferromagnet MnSi. *Phys. Rev. B*, 16:4956, 1977.

[29] Y. Ishikawa, K. Tajima, D. Bloch, and M. Roth. Helical spin structure in manganese silicide MnSi. *Solid State Comm.*, 19:525, 1976.

[30] M. Høgh Jensen. Faseovergange og magnetiske strukturer i MnSi og Neodymium. Master's thesis, University of Copenhagen, Copenhagen, DK, 1981.

[31] M. Kataoka, O. Kakanishi, A. Yanase, and J. Kanamori. Antisymmetric spin interactions in metals. *J. Phys. Soc. Jpn.*, 53:3624, 1984.

[32] L. D. Landau and E. M. Lifshitz. *Quantum Mechanics*, volume 3 of *Course on Theoretical Physics*. Pergamon Press, Oxford, UK, 3'rd edition, 1977.

[33] S. Langridge, J. A. Paixão, N. Bernhoeft, C. Vettier, G. H. Lander, D. Gibbs, S. Aa. Sørensen, A. Stunault, D. Wermeille, and E. Talik. Changes in 5*d*-band polarization in rare-earth compounds. Submitted to Phys. Rev. Lett.

[34] B. Lebech. Magnetic ordering in nearly ferromagnetic antiferromagnetic helices. In A. Katami and N. Suzuki, editors, *Recent Advances in Magnetism of Transition Metal Compounds*, page 167, Singapore, New Jersey, London, Hong Kong, 1993. World Scientific.

[35] B. Lebech, J. Bernhard, and T Freltoft. Magnetic structures of cubic FeGe studied by small angle neutron scattering. *J. Phys.: Cond. Matter*, 1:6105, 1989.

[36] B. Lebech, P. Harris, J. Skov Pedersen, K. Mortensen, S. Aa. Sørensen, H. S. Shim, M. Jermy, J. Wingfield, N. R. Bernhoeft, C. I. Gregory, and S. A. Brown. Magnetic phase diagram of MnSi. In P.-A. Lindgård, K. Bechgaard, K. N. Clausen, R. Feidenhans'l, and I Johannsen, editors, *Annual Progress Report of the Department of Solid State Physics 1 January - 31 December 1994*, page 21, January 1995. Risø Report 779(EN).

[37] S. W. Lowesey. *Theory of Neutron Scattering from Condensed Matter*. Oxford University Press, Oxford, UK, 1984.

[38] S. W. Lowesey and S. P. Collins. *X-ray Scattering and Absorption by Magnetic Materials*. Oxford University Press, Oxford, UK, 1996.

[39] G. J. McIntyre and R. F. D. Stansfield. *Acta Cryst.*, A44:257, 1988.

[40] R. M. Moon, T. Riste, and W. C. Koehler. Polarization analysis of thermal-neutron scattering. *Phys. Rev.*, 181:920, 1968.

[41] A. Onodera, Y. Nakai, N. Kunitomi, O. A. Pringle, H. G. Smith, R. M. Nicklow, R. M. Moon, F. Amita, N. Yamamoto, S. Kawano, N. Achiwa, and Y. Endoh. High-pressure cell for neutron scattering. *Japn. Jour. Appl. Phys.*, 26:152, 1987.

[42] J. A. Paixão and P. A. Conçalves. Structure refinement and investigations of magnetic structure of $HoFe_4Al_8$. Risø National Laboratory, EEC Large Installation Program Experimental Report #234, 1995.

[43] J. S. Pedersen and C. Larsen. *Neutronspredning fra terbium*. Risø National Laboratory, Dk-4000 Roskilde, Denmark.

[44] C. Pfleiderer, G. J. McMullan, and G. C. Lonzarich. Magnetic quantum phase transition in MnSi under hydrostaic pressure. *Physica B*, 199:634, 1995.

[45] M. L. Plummer. Wavevector and spin-flop transitions in cubic FeGe. *J. Phys. : Cond. Matter*, 2:7503, 1990.

[46] M. L. Plummer and B. Walker. Wavevector and spin reorientation in MnSi. *J. Phys. C : Solid State Phys.*, 14:4689, 1981.

[47] G. L. Squires. *Introduction to the Theory of Thermal Neutron Scattering*. Cambridge University Press, Cambridge, UK, 1978.

[48] E. Talik, J. Szade, and J. Heimann. Spin glass behaviour and magnetic anisotropy in $DyFe_4Al_8$ single crystals. *Physica B*, 190:361, 1993.

[49] W. H. Zachariasen. *Acta Cryst.*, 23:558, 1967.

Bibliographic Data Sheet **Risø–R–1125(EN)**

Title and author(s)

Neutron Scattering Studies of Modulated Magnetic Systems

Steen Aagaard Sørensen

ISBN	ISSN
87–550–2570–6	0106–2840

Dept. or group	Date
FYS	August 3, 1999

Groups own reg. number(s)	Project/contract No.

Pages	Tables	Illustrations	References
84	6	42	49

Abstract (Max. 2000 char.)

This report describes investigations of the magnetic systems $DyFe_4Al_8$ and MnSi by neutron scattering and in the former case also by X-ray magnetic resonant scattering.

The report is divided into three parts: An introduction to the technique of neutron scattering with special emphasis on the relation between the scattering cross section and the correlations between the scattering entities of the sample. The theoretical framework of neutron scattering experiments using polarized beam technique is outlined. The second part describes neutron and X-ray scattering investigation of the magnetic structures of $DyFe_4Al_8$. The Fe sublattice of the compound orders at 180 K in a cycloidal structure in the basal plane of the *bct* crystal structure. At 25 K the ordering of the Dy sublattice shows up. By the element specific technique of X-ray resonant magnetic scattering, the basal plane cycloidal structure was also found for the Dy sublattice. The work also includes neutron scattering studies of $DyFe_4Al_8$ in magnetic fields up to 5 T applied along a $< 110 >$ direction. The modulated structure at the Dy sublattice is quenched by a field lower than 1 T, whereas modulation is present at the Fe sublattice even when the 5 T field is applied. In the third part of the report, results from three small angle neutron experiments on MnSi are presented. At ambient pressure, a MnSi is known to form a helical spin density wave at temperature below 29 K. The application of 4.5 kbar pressure intended as hydrostatic decreased the Néel temperature to 25 K and changed the orientation of the modulation vector. To understand this reorientation within the current theoretical framework, anisotropic deformation of the sample crystal must be present. The development of magnetic critical scattering with an isotropic distribution of intensity has been studied at a level of detail higher than that of work found in the literature. Finally the potential of a novel polarization device for small angle neutron scattering is demonstrated by measurements of the magnetic critical scattering from MnSi.

Descriptors INIS/EDB

Available on request from:
Information Service Department, Risø National Laboratory
(Afdelingen for Informationsservice, Forskningscenter Risø)
P.O. Box 49, DK–4000 Roskilde, Denmark
Phone (+45) 46 77 46 77, ext. 4004/4005 · Fax (+45) 46 75 56 27 · Telex 43 116